

Exchange interaction of Fe films on NiO(001) single crystals

Guolei Liu

Max-Planck-Institut für Mikrostrukturphysik
Weinberg 2, 06120 Halle, Germany

March 25, 2003

urn:nbn:de:gbv:3-000006352

[<http://nbn-resolving.de/urn/resolver.pl?urn=nbn%3Ade%3Agbv%3A3-000006352>]

Exchange interaction of Fe films on NiO(001) single crystals

Dissertation

zur Erlangung des akademischen Grades

doctor rerum naturalium (Dr. rer. nat.)

vorgelegt der

Mathematisch-Naturwissenschaftlich-Technischen Fakultät
(mathematisch-naturwissenschaftlicher Bereich)
der Martin-Luther-Universität Halle-Wittenberg

von Herrn **Guolei Liu**

geb. am: 01. August 1972 in Zhejiang, V. R. China

Gutachterin/Gutachter:

1. Prof. Kirschner
2. Prof. Henning Nedermeyer
3. Prof. Schneider (Jülich)

Halle/Saale, 09.12.2003

Abstract

The thesis presented the investigation of the exchange interaction of Ferromagnetic materials (Fe films) epitaxially grown on antiferromagnetic substrates (NiO(001) single crystals). The magnetic domain structures of Fe films were characterized by Scanning Electron Microscopy with Polarization Analysis (SEMPA). The Fe spin polarization is in plane and the interface exchange interaction causes the Fe domains to be modified from “free” Fe films. For Fe film grown on type I NiO(001) single crystal the spin polarization in each domain is roughly oriented along its easy direction [110] (or [1-10]) corresponding to the orientation of NiO(001) crystal. For Fe film grown on type II NiO(001) single crystal the spin polarization in each domain is inclined $6^{\circ}\pm 12^{\circ}$ from [1-10] direction or $11^{\circ}\pm 12^{\circ}$ from [110] direction corresponding to the orientation of NiO(001) crystal. A micromagnetic model was proposed, where the inclined angle is caused by the relatively weak in plane anisotropy K_2 of NiO crystal. The magnetization reversal processes of Fe films were studied by Magneto-optical Kerr Effect (MOKE) and in-field SEMPA. The in-field SEMPA is an advanced extension of SEMPA, which allows SEMPA to work in the presence of an external magnetic field up to 400 Oe. The coercivity of Fe film was enhanced and domain wall creeping was observed at the applied field close to coercivity.

Contents

Introduction	1
1 The exchange interaction between FM and AFM materials	3
1.1 Associated phenomena and applications	3
1.2 Theoretical models	6
1.3 NiO(001) single crystal and Fe/NiO(001) systems	10
2 Experimental setup	13
2.1 SEMPA	13
2.1.1 Overview of the system	14
2.1.2 SEMPA setup	15
2.1.3 LEED spin detector and domain imaging	16
2.2 In-field SEMPA	19
2.2.1 Operation principle	19
2.2.2 Performance characterization by simulation	20
2.2.3 In-field magnetic microscopy	23
2.3 Optical technique for T domains observation	25
3 Experimental results	27
3.1 Preparations of FM/NiO(001) samples	27
3.2 Domain structures of as-grown Fe/NiO(001)	30
3.2.1 Fe domains	30
3.2.2 Thickness dependence	33
3.3 The correlation of Fe domains and T-domains	36
3.4 FM grown on type II NiO(001)	41
3.5 MOKE measurements	44
3.6 Reversal processes by in-field SEMPA	46
3.6.1 Reversal process with decreasing field	46
3.6.2 Reversal process with increasing field	52
4 Discussions and conclusions	55
4.1 a phenomenological model	55

4.2 Discussion on magnetization reversal process	60
4.3 Conclusions	64
Bibliography	67
Summary	73
Curriculum Vitae	i
Erklärung	ii
Acknowledgments	iii

Introduction

In thin film physics it is very common to bring different materials into direct contacts. These contacts can be simply accomplished by depositing ultrathin films on variety substrates or by growing multilayer systems. Usually any combination will give rise to many structural and chemical problems. Beyond that, a particularly interesting situation occurs, when the materials are not different from their chemical compositions, but as regards their magnetic ordering. For example there is a case that multilayer systems formed by thin films, which concern ferromagnetic (FM) materials contacting with antiferromagnetic (AFM) materials, show new magnetic properties which can not be obtained by bulk materials. A remarkable phenomenon is *the exchange anisotropy* among these FM/AFM systems. This phenomenon is a macroscopic effect, which can be clearly established from the hysteresis loops of FM materials in FM/AFM systems: 1). The origin of the hysteresis loops was found to be shifted away from zero in magnetic field axis, while the hysteresis origin of a single FM material was centered at zero field. The symmetry of magnetization reversal process was broken along magnetic field axis in positive and negative sides, hence the energy to reverse the magnetization is not equal to switch it back. 2). The coercivity of the FM materials was generally found to be enhanced and to be much larger than that of single FM materials. Recently the phenomenon of *exchange anisotropy* has found some interesting applications to fabricate a new class device. These FM/AFM systems have attracted much attention in the field of fundamental research as well as technological applications.

The exchange interaction between FM and AFM materials plays an important role in their magnetic properties. Many experimental and theoretical studies have revealed the interaction mechanism. Because of the experimental difficulties for AFM materials the mechanism for the exchange interaction of FM/AFM system is still unclear. In one side, the exchange interaction is realized to be an interface effect between FM and AFM materials, which is difficult for direct experimental measurements. The required experimental and analytical tools for investigating interfacial properties at the atomic level have considerably advanced in recent years. Although these developments lead to an extensive amount of publications, there are still many open questions, and, at present, there is still no comprehensive picture of all available models and theories. In another side, the magnetic properties of AFM materials are less known than FM materials. This is because

that the spins of AFM materials are fully compensated, while most of the magnetic techniques are used to characterize the spontaneous magnetization of samples. Furthermore the magnetic structures of both FM and AFM materials may be modified from their bulk materials by the mutual interaction at interface. To completely understand the problem, one should not ignore these modification of magnetic structures at interface. Up to now, the exchange interaction of FM/AFM systems have been an extensive subject both from the point view of application and fundamental research.

The present thesis is devoted to the subject of the exchange interaction of FM/AFM systems. In order to study the exchange interaction, the Fe/NiO(001) systems are used in present work. Here NiO(001) single crystals and the epitaxial Fe films are AFM and FM materials, respectively. The motivations to choice Fe/NiO(001) single crystals is described as following: 1). For the application the antiferromagnetic NiO is one of the candidates for insulating AFM materials; 2). The magnetic properties of bulk NiO crystals are well-studied, which greatly helps the study of exchange interaction of Fe/NiO(001) systems; 3). By comparing to those of polycrystalline Fe/NiO bilayers, the Fe films grown on NiO(001) single crystals have advantages of controlled interface conditions and no grains with different crystalline orientations.

All conclusions in the thesis rely on the observations of the magnetic domains of FM films epitaxially grown on NiO(001) single crystals. The magnetic domain structures of FM (Fe films) are characterized by using the magnetic imaging technique of Scanning Electron Microscopy with Polarization Analyser (SEMPA) and the AFM domains are detected by optical microscopy. The magnetic reversal processes of ultrathin Fe films are studied by using MOKE (Magneto-optical Kerr Effect) and SEMPA in presenting of external magnetic fields. In particular it is the first time to directly observe the domain behaviors during reversal process of ultrathin Fe films grown on NiO(001) single crystal by SEMPA.

The thesis is divided into four chapters. In chapter 1, the associated phenomena and models of the exchange interaction are briefly introduced, and it also introduced the magnetic structures of NiO(001) single crystals and Fe/NiO(001) systems. Chapter 2 is devoted to the experimental setups for the characterization of magnetic domains. The experimental results, which consists of the observation of magnetic domain structures of Fe films grown on NiO(001) single crystals and the magnetization reversal processes of Fe films, are described in chapter 3. In the last chapter 4, a phenomenological model is proposed to explain the exchange interaction in Fe/NiO(001) systems. The magnetization reversal processes are also discussed. The conclusions for the thesis are given at the end of the chapter.

Chapter 1

The exchange interaction between FM and AFM materials

When the ferromagnetic (FM) materials are contacted with antiferromagnetic (AFM) materials, the magnetic properties of FM materials are drastically modified after a special procedure of heat treatment in presence of strong magnetic field. A remarkable phenomenon is the *exchange anisotropy*. The exchange anisotropy was first discovered in Co/CoO particles by Meiklejohn and Bean [1–3] in 1956. The Co particles revealed a unidirectional anisotropy and a strictly different hysteresis loop comparing to single Co material was observed. In recent years the exchange anisotropy has found many interesting applications. In section 1.1 it briefly introduces the associated phenomena and their applications. Several models have proposed to explain the mechanism of exchange interaction. They are briefly described in section 1.2. In last section 1.3 it is devoted to describe the magnetic structures of NiO(001) single crystals and Fe/NiO(001) systems which were used in our experiments.

1.1 Associated phenomena and applications

The exchange anisotropy of FM/AFM systems was first discovered by Meiklejohn and Bean in 1956 [1, 2]. They used ferromagnetic Co-nanoparticles which were embedded in their native antiferromagnetic CoO layers. The Co/CoO systems were treated by field cooling procedure which the sample was heated and subsequently cooled down to below the Néel temperature T_N with a sufficiently strong magnetic field being presented. The origin of the hysteresis loop of Co in Co/CoO systems was no longer centered at zero field ($H = 0$) which has a shift along the field axis. Since the first discovery in Co/CoO nanoparticles, the exchange anisotropy was observed in other FM/AFM systems, such as small particles, inhomogeneous materials [4], FM films on AFM single crystals and FM on thin

films (seen in review [5] and references therein). Besides FM/AFM systems, exchange anisotropy has been also observed in other types of systems, e.g. involving ferrimagnetic (FIM) materials: FIM/AFM [6] and FM/FIM [7]. Among these systems the types of FM/AFM systems, especially the FM/AFM multilayers, are much more favorable because they are more amenable for the development of device applications [8, 9]. Only the types of FM/AFM systems formed by multilayers are treated in the following descriptions.

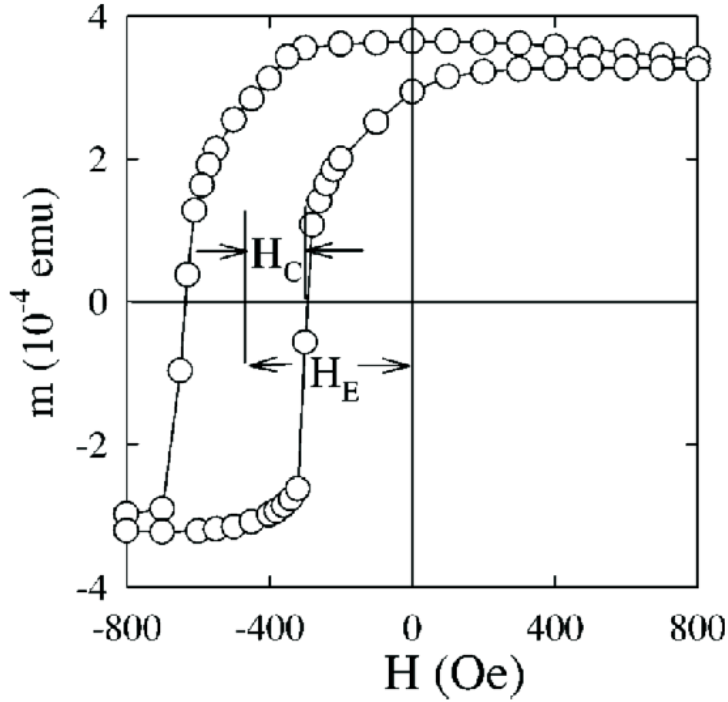


Figure 1.1: *Hysteresis loop for $FeF_2(\sim 90nm)/Fe(\sim 13nm)/Ag(\sim 9nm)$ on $MgO(100)$ grown at $200^\circ C$. The loop was carried out by using SQUID magnetometer at $T=10K$. The definitions for the exchange bias (H_E) and coercivity (H_C) are also shown. From ref. [11].*

The exchange bias [1, 5, 10] and enhanced coercivity [1, 5, 10] are two frequently studied phenomena of FM/AFM systems. Both of them are macroscopic effects of FM/AFM systems, which may be accomplished much simply in the hysteresis loop of FM materials. Fig.1.1 shows a hysteresis loop of $FeF_2/Fe/Ag$ multilayers grown on $MgO(001)$ at $200^\circ C$ [11]. The measurement was carried out by SQUID (Superconductor Quantum Interference Device) at 10K. Here the films of Fe and FeF_2 were FM and AFM materials, respectively. It found that the origin of the hysteresis loop was shifted to left side along magnetic field axis. This phenomenon is named as *the exchange bias* of FM/AFM systems. The exchange bias field H_E is defined as the field shift from the loop origin to zero field, indicated in Fig.1.1. Normally the origin of hysteresis loop is shifted towards left side

where H_E has negative value. The unusual phenomena of positive exchange bias were also found in some systems [12, 13]. The coercivity H_C of the exchange coupled Fe/FeF_2 systems, which indicated as H_C in Fig.1.1, was generally several times larger than those of “free” Fe films. The exchange bias and enhanced coercivity occur after field cooling (Néel temperature T_N of AFM material was lower than Curie temperature T_C of FM materials), or growing FM film in presence of a sufficiently strong magnetic field. Both of the phenomena disappear at and above T_N . The H_E and H_C of FM/AFM systems were influenced by many different parameters involved in, anisotropy, roughness, and spin structures or magnetic domains etc. [5]. They also can be influenced by the field-cooling procedure and the number of hysteresis loop cycles [14].

Except exchange bias and enhanced coercivity, the exchange coupled FM/AFM systems have many other associated phenomena, which consist of the asymmetry of magnetization reversal processes [15, 16], training effect [14], memory effect [17], perpendicular coupling [18, 19] and et al.. The asymmetry of magnetization reversal processes can be the asymmetry of the shape of hysteresis loop [15], or of the magnetic domain behaviors [16] in the demagnetization processes with branches in increasing and decreasing field. In some FM/AFM systems, with increasing numbers of loop cycles the H_E and H_C decrease and the initially asymmetric hysteresis loop becomes more symmetric, which performs training effect [14]. In other FM/AFM systems it was found that at a given temperature the coercivity H_C maintained a unique value while the exchange bias field H_E was manipulated by variety cooling fields, which performed memory effect [17].

The exchange bias of FM/AFM systems has found successful technological applications, such as magnetic domain stabilization in magnetoresistive sensors [20–22] and non-volatile magnetic random access memory (MRAM) [23]. In particular the exchange biased FM films were proved to be immensely useful in the rapidly evolving field of spin electronics or, simply, spintronics [24, 25]. Examples including of the “giant” magnetoresistance spin valves [21, 26–28] and tunnel junctions [29, 30] are currently being studied for myriad data storage and sensor applications [31, 32]. The exchange bias, which exploited in the read head based on the spin-valve structure, is already in the market. Fig.1.2 [33] shows a magnetic recording head. A read head and a write head are typically integrated in the magnetic recording head within the same lithographically defined structures. The write head, which is a magnetic pole tip, is used to write the magnetic bits into a thin magnetic films on a rotating magnetic recording disk. The read head, which is based on spin-valve structure, is used to retrieve the information written on the disk. It senses the magnetic flux emerging from the transition regions between the bits on the disk. The working principle of the read head is based on the giant magneto-resistance (GMR) effect [34–36]. A sense current passing through the spin valve structure performs a resistance, which depends on the magnetization alignment of two FM layers. The magnetization direction in “hard” FM layer FM2 is pinned by an AFM layer and does not be rotated. The flux from the disk is large enough to change the magnetization direction in “free” FM layer (FM1 in the read head shown in the bottom panel of Fig.1.2). The magnetization alignments of two ferromagnetic layers FM1 and FM2 have two states, which are parallel “1” and

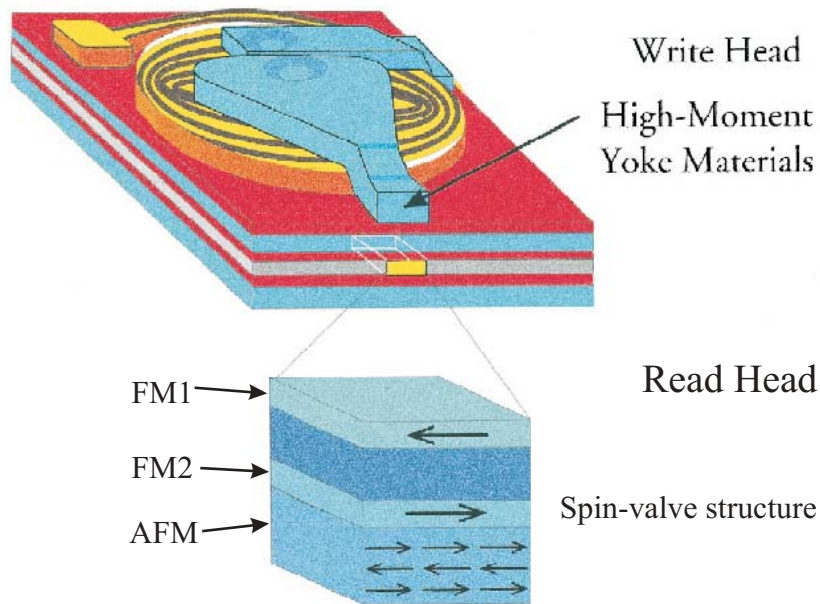


Figure 1.2: Magnetic recording heads typically consists of a write head and a read head within the same lithographically defined structure. The write head consists of a coil and a yoke that guides the magnetic flux created by the coil to a pole tip. The large magnetic field emerging from the pole tip is used to write the magnetic bits into a thin magnetic film on a rotating magnetic-recording disk. The read head is used to retrieve the information written on the disk. It senses the magnetic flux emerging from the transition regions between the bits on the disk. From Ref. [33].

antiparallel “0”. The resistance of alignment “0” is higher by about 10% than that of alignment “1”. In this example the exchange bias of FM2 and AFM layers plays a role.

1.2 Theoretical models

Recent years several models and theories were proposed to understand the mechanism of the exchange anisotropy such as the simplest model [1, 37], Mauri’s model [38], random field model [39–41] and perpendicular coupling [42, 43]. They are mainly focused on explaining the exchange bias, and a few on the enhanced coercivity and other associated phenomena.

The simplest model for the exchange anisotropy was proposed by Meiklejohn and Bean [1, 5, 10, 37]. It assumes that either FM or AFM film in FM/AFM bilayers is a single crystallite and the exchange bias occurs at an ideal smooth interface. It also assumes

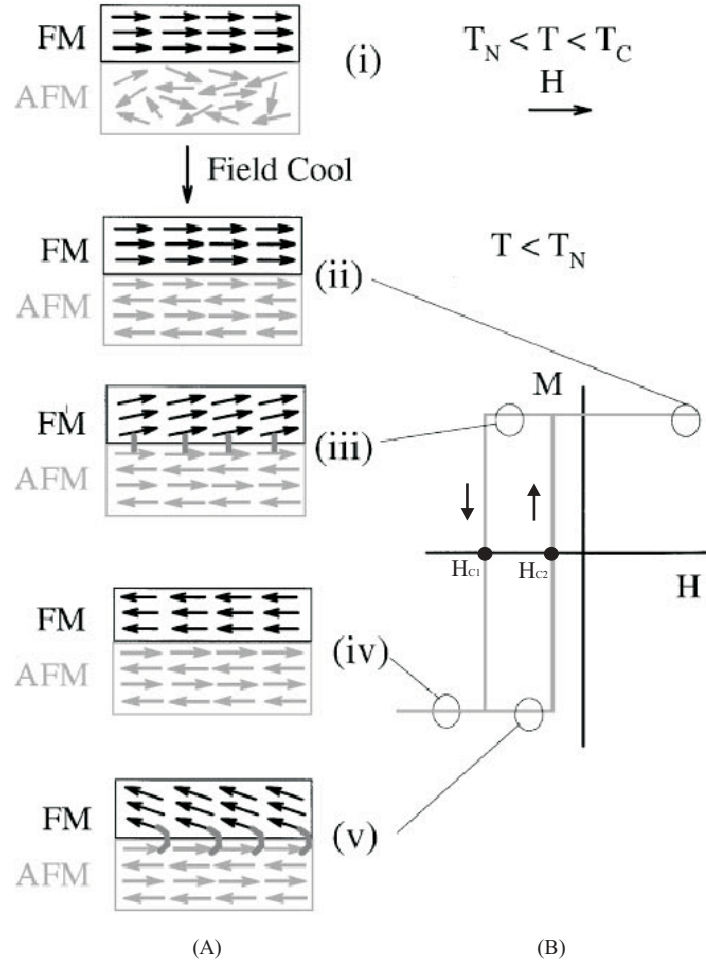


Figure 1.3: Schematic diagram of the spin configuration of FM/AFM bilayer. An exchange biased hysteresis loop (B), (A)(i)-(v) at different states. Note that the spin configurations are just a simple cartoon to illustrate the effect of the coupling and they are not necessarily accurate portraits of the actual rotation of the magnetization of FM or AFM layers. From Ref. [5]

that the interfacial spin plane of AFM film is fully uncompensated. Since the moments of AFM materials are fully compensated, their spins are alternatively aligned parallel or antiparallel. An intuitive picture of this simplest model is schematically shown in Fig.1.3. When a magnetic field is applied in the temperature range of $T_N < T < T_C$ (T_N and T_C are Néel temperature of AFM film and Curie temperature of FM film, respectively), the spins of FM film line up with the field, while the AFM film is in nonmagnetic state and its spins remain random (Fig.1.3A(i)). When the temperature cooling down to $T < T_N$ in presence of a sufficiently strong magnetic field, the spins of AFM layer next to the FM layers align parallel to those of the FM spins (assuming collinear coupling). The spins of other layers

in AFM materials “follow” the spins of the first layer alternatively, so as to produce zero net magnetization (Fig.1.3A(ii)). During the reversal of magnetization, the spins of the FM film assume to be rotated coherently, while the spins of the AFM film remain fixed (Fig.1.3A(iii)). The spins of AFM film at the interface exert a microscopic torque on FM spins (Fig.1.3A(iv) and (v)). The magnetic field to reverse the magnetization of the FM film with decreasing field branch is larger than that with increasing field branch (Fig.1.3(B)). An extra field is needed to overcome the microscopic torque (Fig.1.3A(ii) and A(v)). Thus the hysteresis loop is shifted, i.e., an exchange bias and unidirectional anisotropy is observed. The phenomenological formula of the exchange bias field H_E can be written:

$$H_E = \frac{\Delta\sigma}{M_{FM}t_{FM}} = \frac{2J_{ex}S_{FM} \cdot S_{AFM}}{a^2M_{FM}t_{FM}} \quad (1.1)$$

Where $\Delta\sigma$ is the interfacial exchange energy density, and M_{FM} and t_{FM} are the magnetization and thickness of FM film, respectively. J_{ex} is the exchange parameter, S_{FM} and S_{AFM} are the spins of FM and AFM films, and a is the cubic lattice constant. However, the observed exchange bias fields H_E for all types of FM/AFM systems are two-to-three orders smaller than the values of theoretically expected. It shows that this simple ideal model does not realistically represent the interfacial environment of FM/AFM systems.

To explain the discrepancy between the exchange bias field values predicted by simple theory and experimental observations, Mauri et al. [38] proposed a model that would effectively lower the interfacial energy cost of reversing the FM magnetization without removing the conditions of strong interfacial FM/AFM coupling [10]. They proposed the formation of planar domain walls at interface with the reversal of FM magnetization. The planar domain walls could be either in AFM or FM side, wherever the total energy of exchange coupling is lower. They examined a case that the domain wall formed in AFM side. With the magnetization reversal of the FM film, the increase of interfacial exchange energy would be equal to the energy per unit area of an planar domain wall $4\sqrt{A_{AF}K_{AF}}$, where A_{AF} and K_{AF} are the exchange stiffness and the AFM magnetocrystalline anisotropy, respectively. In this case the exchange bias field is written:

$$H_E = \frac{2\sqrt{A_{AF}K_{AF}}}{M_{FM}t_{FM}} \quad (1.2)$$

By spreading the exchange energy over a domain wall width $\pi\sqrt{A_{AF}K_{AF}}$ instead of a single atomically wide interface, the interfacial exchange energy is reduced by a factor of $\pi\sqrt{A_{AF}K_{AF}}/a \approx 100$, which would provide the correct reduction to be consistent with the observed values. Their numerical calculation over a range of interfacial exchange energies yields the following two limiting cases:

Strong interfacial coupling:

$$H_E = -2\left(\frac{\sqrt{A_{AF}K_{AF}}}{M_{FM}t_{FM}}\right), \quad (1.3)$$

Weak interfacial coupling:

$$H_E = -\left(\frac{J_{ex}}{M_S t_{FM}}\right), \quad (1.4)$$

Where J_{ex} is the effective interfacial coupling energy, t_{FM} and M_S are the thickness and the saturation magnetization of the FM materials. This model highlights the formation of an AFM planar domain wall in the limit of strong interfacial exchange. Recent experimental results show a spiraling spin structure in an exchange-coupled AFM film – Py/FeMn/Co trilayer system [44]. This experiment supports the formation of AFM domain walls at interface. However, this model does not shed light on the mechanism being responsible for the reduced interfacial exchange coupling energy density [10].

The similar exchange bias field was obtained in a random field model proposed by Malozemoff [39–41]. Contrary to the simplest model, Malozemoff assumes that the interface of FM/AFM bilayer systems is not an atomically perfect boundary. In his model the random field, which induced by the roughness and structural defects at interface, causes the AFM film to be broken into domains, whose size is inversely proportional to the exchange bias field. In the model he gives the exchange bias field:

$$H_E = \frac{2z\sqrt{AK}}{\pi^2 M_{FM} t_{FM}} \quad (1.5)$$

Where A and K are the exchange stiffness and uniaxial anisotropy per unit volume of AFM materials. a is the cubic lattice parameter, z is the number of order unity. Quantitatively, the random field model also accounts for the 10^{-2} reduction of the exchange field estimated from the simplest model. Both of the random field model and Marie’s model proposed the formation of AFM domain walls. But the former model has lateral domain wall and the latter has planar domain wall. The random field model is specifically formulated for single crystal AFM systems and does not clearly propose how the model can be extended to polycrystalline systems. The argument of a statistical basis for the density of uncompensated spins is intriguing but not explicitly convincing [10].

The “spin-flop” model was proposed by Koon [42]. On the basis of his micromagnetic numerical calculations, Koon proposed the existence and stability of unidirectional anisotropy in thin films with a fully compensated AFM interface. He calculated the interfacial energy density as a function of the angle between the FM spins and the Néel axis of the AFM spins at interface. The fully uncompensated interface gives the expected results of collinear coupling. However, the fully compensated interface gives the surprising result that an energy minimum is at 90° with the spins of FM and AFM at

interface, which indicates perpendicular interfacial coupling between FM and AFM spins at interface. One limitation of Koon's model is that he examines a very special system, which is difficult to apply the model to other systems. But the work by Schulthess and Butler [43] yielded findings contrary to Koon's calculations. Their calculation shows that the "spin-flop" coupling does not lead to exchange bias, but rather gives rise to a uniaxial anisotropy which in turn causes the large coercivity observed in exchanged biased films. Recent experiments of X-Ray PEEM in Co/NiO(001) single crystal [45] and exchange biased Co/FeMn bilayer [46] show collinear exchange coupling.

The experimental correlation between the uncompensated CoO spins at interface and the exchange bias field in Permalloy/CoO bilayers was demonstrated by Takano et al. [47, 48]. They measured the thermoremanent magnetization (TRM) in Co/MgO multilayers after field cooling. The TRM, which originates from the uncompensated interfacial AFM spins, is interfacial and is about 1% of the spins in a monolayer of CoO. The TRM exhibited the same magnitude and temperature dependence as the exchange bias field of Permalloy/CoO bilayers. They proposed a model which based on a calculation of the density of interfacial uncompensated spins and accounts for grain size, orientation, and interfacial roughness. The model shows that the origin of the exchange biasing mechanism is the cause of uncompensated interfacial AFM spins. But this model do not tell the type of interfacial coupling, i.e. collinear or perpendicular coupling. CoO has very high magnetocrystalline anisotropy, while the lower anisotropy materials like NiO are not included in this model.

1.3 NiO(001) single crystal and Fe/NiO(001) systems

Since the discovery of exchange anisotropy in FM/AFM systems [1], numerous investigations have been carried out both from a theoretical and an experimental points of view. Among all the reported investigations involved in insulating AFM materials, FeF_2 and monoxides such as NiO, CoO, and $Ni_xCo_{(1-x)}O$ et al., NiO is one of the candidates for applications [5, 10]. It has advantages of relatively high Néel temperature T_N , no current shunting, excellent thermal stability and excellent corrosion resistance [49], which makes it attractive for commercial applications. Comparing to polycrystalline bilayers, the epitaxial Fe films grown on NiO(001) single crystals have better controlled interface conditions. The NiO(001) single crystals eliminates the complexity of having small grains with different crystallite orientation. Furthermore, the annealed NiO(001) single crystals used at present works have very large AFM domains in size of several mm [50, 51], which simplify the complexity of AFM domains.

The magnetic properties of anti-ferromagnetic NiO single crystals have been investigated by Roth and Slack by neutron diffraction and optical observations [50, 52–54]. The Néel temperature of NiO crystal T_N is 523K. Above T_N , NiO crystal is paramagnetic,

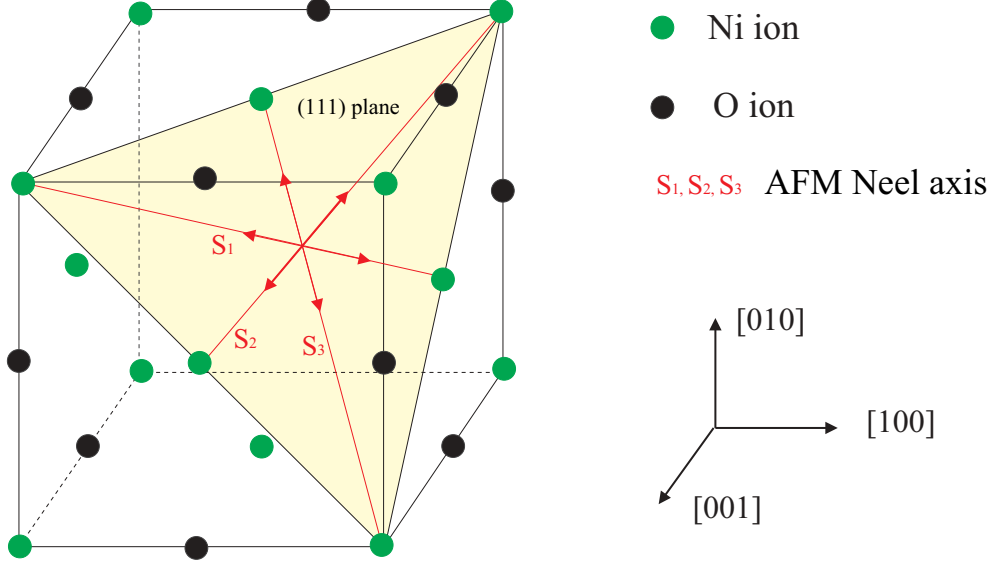


Figure 1.4: Schematically illustrates the lattice and spin structures of NiO single crystal. Here (111) plane is the ferromagnetic sheet indicated as filled plane. All of the Ni ion spins lie in FM sheet. S_1 , S_2 and S_3 are the possible Néel axes.

and its crystal structure is a perfect face center cube (fcc). The unit cell of NiO crystal is schematically illustrated in Fig.1.4. Below T_N , it is anti-ferromagnetic. The magnetic moments of Ni ions have spin-only values with $S = \frac{1}{2}$ [57, 58]. The super-exchange interaction between Ni ions on opposite sides of an oxygen ion causes the spins of nickel ions to be aligned antiparallel. The spins of Ni ions are collinear alignment [50, 53, 59], which are parallel or anti-parallel to the characterized Néel axis. The spins of Ni ions lie within their ferromagnetic (FM) planes [52, 54], shown as the filled (111) plane in Fig.1.4. Besides (111) FM plane, the NiO crystal has three other possible FM planes, $(\bar{1}11)$, $(1\bar{1}1)$ and $(11\bar{1})$ planes (not shown in Fig.1.4). The Néel axis of NiO lies within the associated (111) FM plane. It has six-fold symmetry in (111) FM plane, which has three possible Néel axes along $[211]$, $[121]$ and $[112]$ directions denoted as S_1 , S_2 and S_3 in Fig.1.4. An S (spin-rotation) wall is caused by rotation of the direction of Néel axis. The S-wall separates the regions of the crystal in which there is no change of FM plane, but merely a rotation of the spin direction within the FM plane [50].

Below T_N , the antiferromagnetic ordering results in a slight rhombohedral deformation from the original cubic unit cell along one of the $\langle 111 \rangle$ axes [50, 52, 55, 56]. Because this contraction may occur along any of four equivalent directions in the parent cubic lattice, crystallographic twinning which is related to the antiferromagnetic ordering may take place. A rhombohedral unit cell, which is a slightly distorted cube, is shown in

Fig.1.5. The amount of this distortion increases with the temperature decreasing. The rhombohedral angle α is slightly larger than 90° , which is reported to be $90^\circ 4'$ at room temperature [52]. This small rhombohedral distortion may cause the macroscopic crystal to be twinned below T_N , and to be composed of many small regions with each characterized by a rhombohedral axis along one of four $\{111\}$ directions. These small regions are termed as T (twin) domains. For example regions I and II shown in Fig.1.5 are two T domains. The T domains are separated by T wall plane which terminates a T-wall on the surface. On (001) surface plane the terminated T-walls are oriented along $[100]$, $[010]$, $[110]$ or $[\bar{1}10]$ direction. The T walls can be determined both by neutron diffraction and by optical observation. The S walls have not been observed directly, though their properties have been studied by rotation torque and neutron diffraction measurements on single crystals in magnetic field [52].

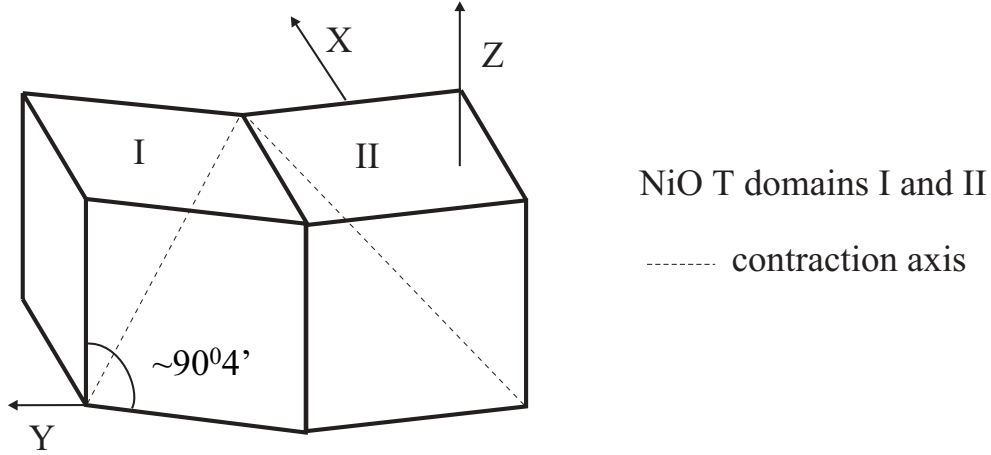


Figure 1.5: An exaggerated model of the rhombohedral distortion in $\text{NiO}(001)$ single crystal below T_N . The crystal was contracted along the axes of dashed lines, which causes the lattice constant slightly distorted. T(win)-domains I and II were formed. From Ref [52].

Fe film has small lattice mismatch between bcc Fe and fcc-like $\text{NiO}(001)$ single crystal. The lattice constants of fcc $\text{NiO}(001)$ single crystal a_{NiO} and bcc Fe film a_{Fe} are 0.4178 nm [60] and 0.287 nm at room temperature, respectively. The lattice mismatch of them $\Delta = \frac{(a_{\text{NiO}}/\sqrt{2} - a_{\text{Fe}})}{a_{\text{NiO}}/\sqrt{2}}$ is about 2.85%, which promotes a pseudomorphic growth of Fe film on $\text{NiO}(001)$ substrates.

Chapter 2

Experimental setup

The techniques to characterize the magnetic domains of FM (Fe and Permalloy) films and NiO(001) single crystals are briefly described in this chapter. Scanning Electron Microscopy with Polarization Analyser (SEMPA) is used to characterize the ferromagnetic domain structures. Its basic setup and physical principle are described in section 2.1. A novel extension technique of in-field SEMPA, which allows to perform SEMPA in external magnetic fields, is developed and presented in section 2.2. With this advanced extension of SEMPA it is possible to investigate the magnetization reversal processes by using SEMPA. The last section 2.3 describes the optical technique to image T domains.

2.1 SEMPA

Scanning Electron Microscopy with Polarization Analyser (SEMPA) or spin-polarized Scanning Electron Microscopy (SP-SEM) is a powerful imaging technique for the observations of ferromagnetic magnetic domain structures. The technique was originally suggested by DiStefano in 1978 [61, 62]. The first working instrument was built by Koike and Hayakawa [63], who combined an electron gun with a spin detector to visualize magnetic domains of Fe(100) single crystal. Shortly afterward, Unguris et al. [64] used an ultrahigh-vacuum SEM with an attached home-built spin analyzer to image magnetic domain patterns. In the meantime, various SEMPA systems have been built throughout the world. SEMPA has the advantages of high lateral resolution and outstanding surface sensitivity, which is particularly suitable for the investigations of ultrathin ferromagnetic films without the need to thin specimens as that in transmission electron microscopy [62, 65–68]. These features are at present highly sought, since many industrial applications such as magnetic RAMs (Magnetic Random Access Memories) and sensors are essentially sub- μm elements [23].

2.1.1 Overview of the system

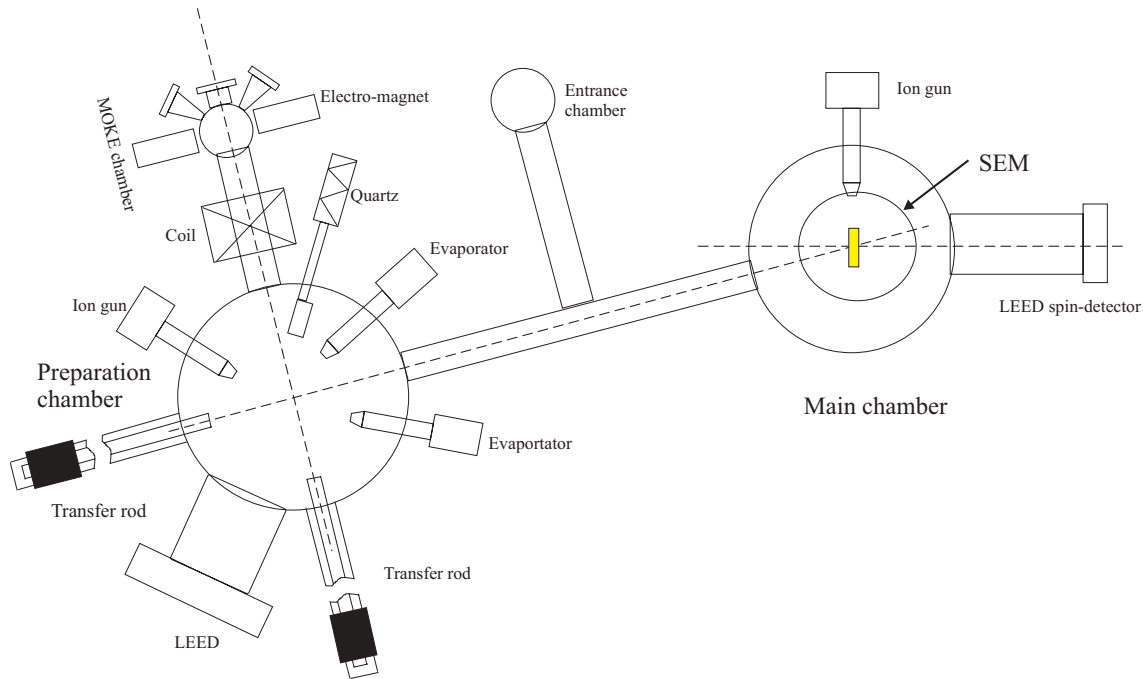


Figure 2.1: *Top view of SEMPA system. The setup consists of a main chamber for microscopy techniques (SEM, AES and SEMPA), a preparation chamber for film growth and characterization, a MOKE chamber for optical measurements and an entrance chamber.*

Fig.2.1 schematically shows the entire SEMPA system, which consists of several ultra-high vacuum (UHV) chambers. The sample surface cleaning, thin film evaporation and film thickness calibration by a Quartz microbalance are performed in preparation chamber. A Low Energy Electron Diffraction (LEED) is attached to the preparation chamber to characterize the sample surface properties. The chemical composition and surface topography are characterized by an Auger Electron Spectroscopy (AES) and a Scanning Electron Microscopy (SEM) in main chamber. A high focused ion gun in the main chamber is used for milling the sample during the procedure of depth profiles both of SEM and SEMPA. The spin polarization of secondary electrons emitted from ferromagnetic samples can be analyzed by a LEED spin detector which is attached to the main chamber. MOKE and other optical measurements are carried out in a “MOKE” chamber. A pair of electro-magnets outside the “MOKE” chamber can apply magnetic field up to $\sim 0.4T$ in surface plane. The system is equipped with series of roughing pumps, turbo pumps and ion pumps to obtain ultra-high vacuum. The base pressure is about 4×10^{-11} mbar. To avoid vibrations during SEMPA measurements the entire SEMPA system is put on a (commercially available) damping system. A magnetic field compensation consisting of

three pairs of Helmholtz coils is used to avoid magnetic field fluctuation.

2.1.2 SEMPA setup

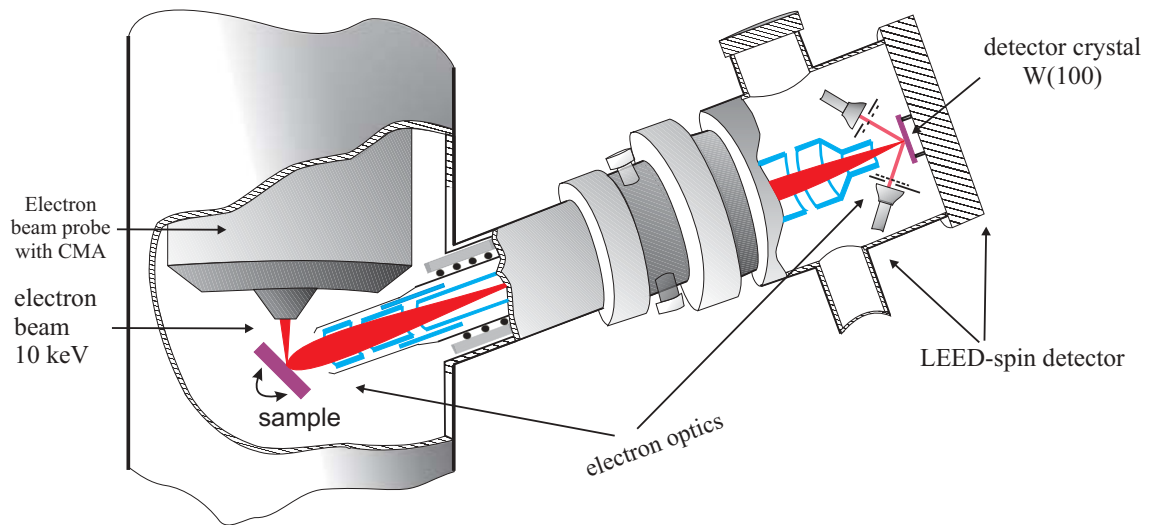


Figure 2.2: *Basic setup of SEMPA consisting of an electron source (PHI SAN 670), electron optics and a Low Energy Electron Diffraction (LEED) spin detector.*

SEMPA is a straightforward extension of standard Scanning Electron Microscopy (SEM). The basic setup of SEMPA is schematically shown in Fig.2.2. It consists of an electron beam source (PHI SAN 670), electron optics and a spin detector. The Low Energy Electron Diffraction (LEED) spin detector is used in present setup.

SEM and SEMPA use a common bright electron beam which is generated by a field emission tungsten tip coated with LaB_6 film. The electron beam is accelerated to high energy ($1 \sim 25kV$) and finely focused on sample surface. The incident electrons are scattered at the electrons in near-surface region of the sample in various ways [62, 66, 69]. The predominant process is inelastic scattering: An incoming primary electron transfers part of its energy to an electron of the sample. In most cases upon scattering, the electron loses only a small amount of energy. This process occurs repeatedly until it has essentially lost its energy and a cascade of excited low-energy secondary electrons has been created. A considerably number of excited secondary electrons travel back to the surface and are ejected into the vacuum. The number of secondary electrons depends on the local curvature of the surface. Scanning the primary beam across the sample surface, an image of the sample topography is obtained by recording the number of secondary

electrons at each position of the incoming electron beam. If it is a ferromagnetic sample, the excited secondary electron beam is spin polarized [69–72]. The spin polarization of the secondary electrons are detected by the attached spin detector. By scanning the incident electron beam images of surface topography and magnetic structures can be obtained simultaneously.

2.1.3 LEED spin detector and domain imaging

The spin polarization of the excited secondary electrons depend strongly on their kinetic energy [69–72]. The spin polarization P and the beam intensity I are shown as function of kinetic energy of secondary electrons in Fig.2.3 [62]. At kinetic energy above 20eV the polarization has the value which expected from the spin imbalance of the bands near the Fermi level. But at very low energy the polarization peaks at a value typically two or three times of that expected above 20eV. This enhancement of spin polarization at very low energy is attributed to the preferential inelastic scattering of \downarrow spin electrons, which leads to a higher escape probability for \downarrow spin electrons. Since the intensity of secondary electrons is also highest at the lowest energies, it is an relatively large energy window (typically 0 to 10 eV) with their high polarization [62].

The spin polarization of excited secondary electrons is characterized by a spin detector. There are varieties of spin detectors, e.g. LEED detector [73], Mott detector [74] and low-energy diffuse scattering detector [64]. The physical principle behind most of them is the same, which uses spin-orbit interaction as a means of transforming a spin polarization into the spatial asymmetry. The LEED spin detector, which is schematically shown in Fig.2.2, is described in following. The secondary electrons excited from the sample are extracted by electronic lens. They are subsequently accelerated to an energy of 104.5 eV and scattered by a W(100) single crystal. This scattering is polarization-dependent because of the spin-orbit interactions. Therefore, electrons of \uparrow and \downarrow spins with respect to the scattering plane are preferentially scattered into different directions. Since the incident electron beam is perpendicular to W(001) surface, at the energy of 104.5 eV the diffracted electron beams have four equivalent peaks at $[20]$, $[\bar{2}0]$, $[02]$ and $[0\bar{2}]$. The number of scattered electrons are counted by a channeltron located in front of W(100) and face to one of four diffraction beams, seen in Fig.2.2. The spin polarization P is then determined by the asymmetry A in a pair of counts N_{\uparrow} and N_{\downarrow} :

$$P = \frac{1}{S} \cdot A. \quad (2.1)$$

$$A = \frac{(N_{\uparrow} - N_{\downarrow})}{(N_{\uparrow} + N_{\downarrow})} \quad (2.2)$$

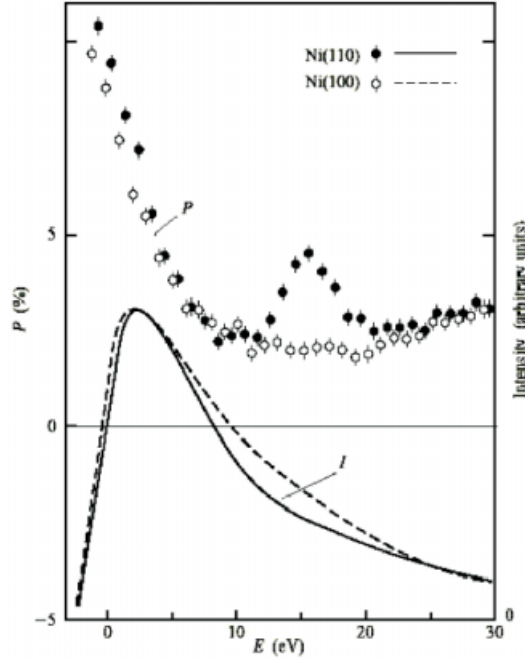


Figure 2.3: The spin polarization P and beam intensity I as a function of kinetic energy of secondary electrons from Ni(100) and Ni(110), recorded at a primary-electron energy of 600 eV. Note the large polarization enhancement at low kinetic energies. Similar enhancements occur for the other 3d transition metal ferromagnets Fe and Co, with peak values of $\sim 50\%$ and $\sim 35\%$, respectively. The polarization peak at 16 eV in Ni(110) is a signature of the spin-polarized band structure for this particular crystallographic orientation. [62]

Where S is the integrated Sherman function. For the entire range of collected angles at LEED spin detector $S=0.25$. Normally the LEED spin detector are equipped by two pairs of channeltrons which give two orthogonal components of polarization. The polarization of excited secondary electrons is proportional to the magnetization of sample but with opposite direction:

$$\vec{P} \propto \vec{A} \propto -\vec{M} \quad (2.3)$$

The domain imaging procedure of SEMPA measurements can be simply illustrated in Fig.2.4. The unpolarized primary beam is finely focused on a ferromagnetic domain with magnetization \vec{M} . The excited secondary electron beam is spin polarized with polarization $\vec{P} \propto -\vec{M}$. These secondary electrons are accelerated and scattered at a W(100) single crystal and consequently counted by a pair of channeltrons. The acquired asymmetry A is proportional to the sample magnetization. Additionally, the channeltrons are configured in two pairs so that two components of the spin polarizations can be recorded simultaneously. Scanning the incident beam across the sample surface, both of the topography and magnetic information as a function of incident beam position were obtained

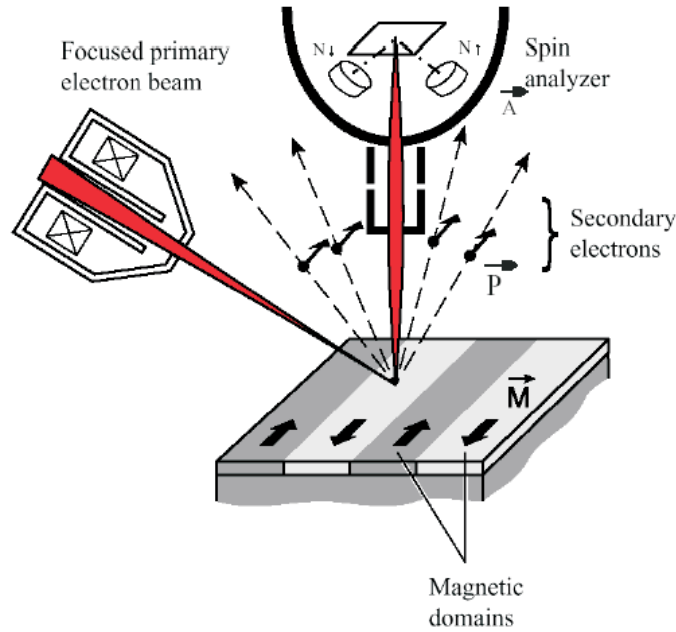


Figure 2.4: *Schematic illustration of the SEMPA principle. An unpolarized, focused electron beam is scanned across a ferromagnetic surface (\vec{M}), and the spin polarization (\vec{P}) of the excited secondary electrons, a measurement of the surface magnetization, is determined by asymmetry (\vec{A}) of spin analyzer. From Ref. [62].*

simultaneously. A significant advantage of SEMPA over most other magnetic imaging techniques follows from equation 2.2: the polarization is a normalized quantity, which the fluctuations of the incoming beam current and the emitted secondary electrons (from surface morphology) are completely separated from the magnetization images.

Compare to other spin detectors, the LEED spin detector can be quite small due to the low energy of the scattering electrons. Furthermore, it has a higher Sherman function and figure of merit. The figure of merit F for a spin detector is defined as: $F = S^2 I / I_0$. Where I is the backscattered current intensity collected at the electron counters and I_0 is the incident beam intensity. The figure of merit is the characteristic of the counting statistic of a polarization experiment. In general, the figure of merit of a spin detector is of the order of 10^{-4} [75]. The efficiency of spin detector is low which makes the image acquisition very slow.

In summary SEMPA is a powerful technique for magnetic domain imaging by quantitatively measuring the magnetization distribution on ferromagnetic samples. Comparing to other magnetic imaging techniques it has advantages: 1). High lateral resolution. It is governed primarily by the size of the probing electron. 2). High surface sensitivity. This is because of the short probing depth of SEMPA, which is determined by the short inelastic mean free path of the secondary electrons. The depth of information is only a

few atomic layers. Therefore ultrathin films already provide sufficient spin polarization signal.

2.2 In-field SEMPA

As described in preview section, the use of low energy secondary electrons has the advantages of higher polarization and higher intensity. But it also has the disadvantage that very weak external magnetic field can disturb the polarization measurements. When the sample is exposed in a magnetic field several difficulties may be conceived. First, the spot size of the primary beam could be deteriorated by aberrations. Furthermore, the spin polarization of the secondary electrons could be falsified due to spin precession, and finally, the secondary electron beam could be significantly deflected by the magnetic field, so that the electrons do not reach the spin detector. Thus only remanent states were typically investigated by SEMPA. Though some groups resorted performing SEMPA either in very weak magnetic fields [62] or with special samples [76], they are not really successful to apply magnetic fields within the imaging procedure. Contrary to these experimental approaches, a new in-field technique was proposed and developed to allow imaging domains that are directly exposed in strong external magnetic fields [77].

2.2.1 Operation principle

The main idea behind the approach is very simple. All disturbing effects caused by a magnetic field at the sample surface may be reduced by decreasing the transit time through the magnetic field. This is accomplished by using a locally confined magnetic field and an additional electric field to accelerate the slow secondary electrons directly after emission.

Based on this idea a device with a miniature magnet circuit and an electrostatic quadrupole is developed and added to SEMPA setup, which is illustrated in the left panel of Fig.2.5. Both the primary and secondary electron beam pass through the magnetic gap. The secondary electrons are accelerated by the potentials applied to the sample, the magnetic foil and the electrostatic quadrupole. In this device the magnetic circuit ends towards the sample with a narrow gap (pole distance $120 \mu m$) from which the magnetic field protrudes. The magnetic field generated by the magnetic circuit is confined to a small volume. The volume between the magnetic pole pieces is shown in the right panel in Fig. 2.5. The sample is positioned very close to the magnetic pole pieces ($10 - 40 \text{ mm}$) so that the surface region near the gap can be exposed in strong magnetic fields. The adjustable distance between sample and pole pieces h is typically chosen between 10 and $40 \mu m$. Further dimensions are: magnetic foil thickness $d = 100 \mu m$, magnetic gap width $g = 120 \mu m$, and magnetic foil width $w = 1 \text{ mm}$. The incidence angle of the

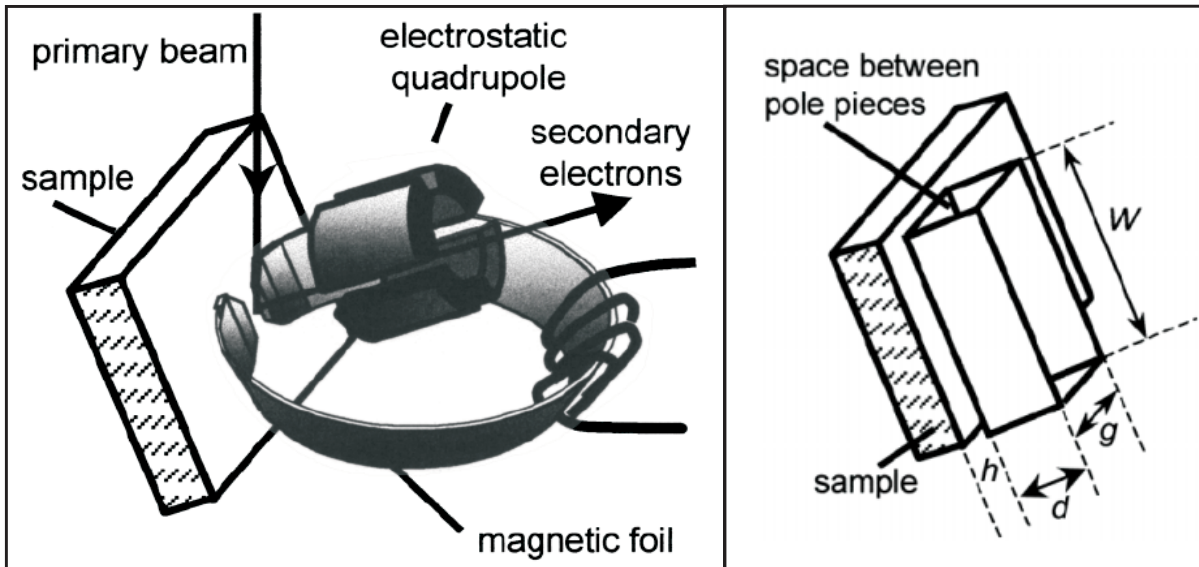


Figure 2.5: *Left panel: A miniature magnet circuit and an electrostatic quadrupole for in-field SEMPA measurements. The incidence angle of the primary electron beam used in the experiment is 52° with respect to the sample normal. Right panel: The volume between the magnetic pole pieces. The adjustable distance between sample and pole pieces h is typically chosen between 10 and 40 μm . Further dimensions are: magnetic foil thickness $d = 100\mu\text{m}$, magnetic gap width $g = 120\mu\text{m}$, and magnetic foil width $w = 1\text{mm}$.*

primary electron beam used in the experiment is 52° with respect to the sample normal. The accelerating electric field is generated by placing the magnetic foil and the sample on different potentials, typically several hundreds of volts, depending on the distance chosen between sample and magnet. Typical values are: -100 V (sample), ground potential (magnetic foil) and 400 V (electrostatic quadrupole). Thus the magnetic pole pieces serve not only as sources of the magnetic field but also as electrostatic electrodes. A subsequent electrostatic quadrupole is used to further accelerate the secondary electrons after passing the gap and to correct for small deflections induced by the magnetic field.

The magnetic circuit was machined from a high permeability foil [78] by using a laser cutter. For precise positioning, the entire assembly is mounted on a three-axes piezo-driven positioner. By using the SEM mode the positioning of the magnetic circuit with respect to the sample surface is monitored accurately.

2.2.2 Performance characterization by simulation

The beam size of the primary electron beam and the spin precession associated with

the secondary electrons are two main characteristics of the device. The performance of the spin precession can be characterized by numerical simulation.

As described above, for in-field measurements the magnetic field is confined locally in the volume of circuit gap. In general the magnetic field produced by the magnetic circuit is not only given by the excitation current of magnetic circuit, but also depends on magnetic sample. In the case of most ultrathin films the contribution resulting from magnetic sample is small and may be neglected completely. But this magnetic field generation may be significantly influenced by the magnetic films with a thickness of several μm or more, which results in the difficulty for this in-field technique [77]. So only the samples of ultrathin film and magnetic microstructures ($< a \text{ few } \mu m$) are suitable for in-field SEMPA measurements.

To discuss the performance of the setup it is useful to recall at the outset that the precession of electron spin polarization and the deflection of electrons in a magnetic field are closely related phenomena [79]. This may be seen by examining the equations of motion for the electron velocity \vec{V} and the spin-polarization \vec{P} in a magnetic field \vec{B} :

$$m\dot{\vec{V}} = e\vec{V} \times \vec{B}, \quad m\dot{\vec{P}} = e\vec{P} \times \vec{B} \quad (2.4)$$

where the approximate gyromagnetic ratio of 2 was used, instead of the more accurate value 2.0024. This approximation is completely sufficient in the present context and makes it apparent that both equations of motion are identical. Thus only one solution needs to be considered, which describes the well-known precession of a vector around the direction of the magnetic field. The precession frequency is given by the Larmor frequency ($\omega = geB/2m$), which is independent of vector directions. For a given electron trajectory the time integral over the Larmor frequency may be used to define the total angle of precession φ that is induced by the magnetic field. Since the equations are identical, it is clear that the total precession caused by a magnetic field is the same for the velocity vector and the polarization vector. Therefore both difficulties associated with secondary electrons, i.e., the bending of the trajectories away from the detector and the precession of spin, can be controlled by considering only a single quantity – the total angle of precession φ . When this value remains small for all detected electrons it is certainly possible to perform meaningful measurements. The dimensions of our setup were chosen to fulfill this requirement, even though it is stricter than absolutely necessary, since one could easily correct for larger values of φ as long as the scatter of φ in the detected electron beam remains small.

Since the electric and magnetic field produced by the magnetic circuit are inhomogeneous, they can be determined by numerical simulation. A three-dimensional ray tracing program was used for the numerical simulation [80]. For calculating fields close to the center of the gap it is found that the two-dimensional approximation is satisfactory, which might be expected from the large aspect ratio of the pole pieces ($\frac{d}{w} = 10$). As a boundary condition for magnetic field calculation constant magnetic potentials on the surfaces of

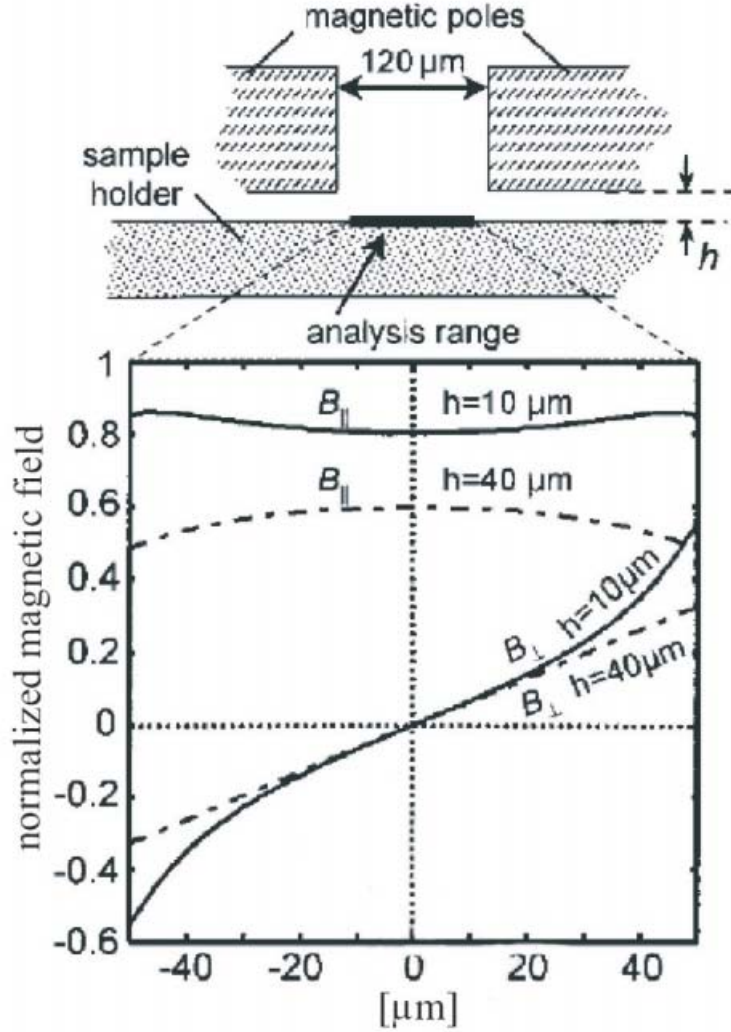


Figure 2.6: *In-plane ($B_{||}$) and out-of plane (B_{\perp}) field components in the analysis range of 100 μm for different distances (h) of 10 and 40 μm between magnetic pole pieces and sample surface. The magnetic field is normalized to the averaged field B_0 .*

the pole pieces were used. This is applicable due to the high permeability of the magnetic material ($> 25\,000$) [78].

The electric and magnetic field are calculated by solving the Laplace equations:

$$\Delta E = 0, \quad \Delta B = 0 \quad (2.5)$$

The result for the magnetic field on sample surface is shown in Fig.2.6. The field strength is normalized to the field (B_0) given by the ratio of the magnetostatic potential drop

across the gap and the gap distance. The in-plane field is extremely homogeneous over a large fraction of the pole piece distance. In addition, the magnetic field does not drop steeply with increasing distance between sample and magnet, e.g., for 10 and 40 μm distance the field at the sample surface and in the middle of the gap is about 0.8 and 0.6 B_0 , respectively. However, the magnetic field is not completely in the plane of the surface. Since the perpendicular component vanishes in the antisymmetry plane its relative importance depends mainly on the size of the imaging range. For scan ranges that do not deviate from the antisymmetry plane by more than about 5 μm , the perpendicular component amounts to only a few percent of the in-plane field. It should be noted that in-plane fields are applied to investigate ultrathin systems with in-plane easy axes. In most cases, the weak perpendicular component is very unlikely to have an effect on these systems.

A ray tracing simulation is performed to investigate the trajectories of secondary electrons. Again, the two dimensional approximation turns out to give accurate results for electrons starting near the center of gap, since most of the spin precession takes place when the electrons are slow and the fields are strong, i.e., in the region close to the sample surface. Due to that the fields are truncated at a distance of 0.6 μm from the sample surface. For simplicity the electrostatic quadrupole shown in Fig.2.5 left panel is omitted which leads to a slight overestimate of the precession angle. To guarantee that w remains below 30° for electrons starting perpendicularly along the central axes of the setup, it is found from the ray tracing simulation that the electric field E_0 must be 10^7 V/m for a magnetic field at the sample surface of 0.1 T and a sample to magnet distance of 40 μm .

2.2.3 In-field magnetic microscopy

For in-field measurements the demagnetized magnetic circuit was inserted and positioned close to the sample surface (35 μm). The positioning was directly monitored by using SEM mode. The primary beam energy of 15 kV was chosen. During imaging it is found that focus and astigmatism have to be readjusted after changes of the magnetic field. Using a properly adjusted primary beam of 10 nA with a spot size below 30 nm no deterioration of resolution due to the magnetic field is detected in the SEM mode [77]. However, we find that the presence of the magnetic circuit decreases the time that the surface remains clean by using AES. Mainly carbon is detected shortly after inserting the magnetic circuit, which might be caused by electron induced desorption from the magnetic circuit. The carbon contamination decreases the spin polarization and therefore prolongs the necessary data acquisition time in SEMPA measurements. The reduced signal and the prolonged measurement time lead to a slight decrease of resolution in the subsequent SEMPA measurements.

The magnetic field acts as a deflection unit on the primary beam. For the primary beam energy and the sample-magnet distance chosen, it is found that the scan range shifts on the sample surface by the amount of 1.9 $\mu\text{m}/\text{mT}$. This value was determined by using

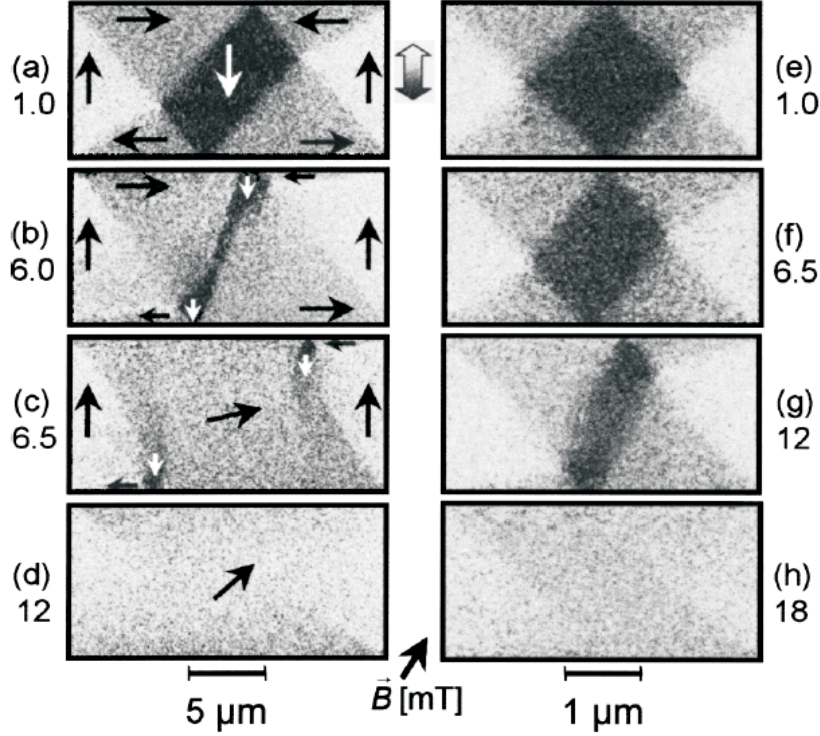


Figure 2.7: Switching processes of Permalloy rectangles (50nm thick) with lateral dimensions $20 \times 10 \mu\text{m}^2$ (left column) and $4 \times 2 \mu\text{m}^2$ (right column). The images display the in-plane spin polarization component in the up-down direction, as indicated by the shaded arrow. The magnetization directions given by the arrows within the images follow from the combination of both measured in-plane components. For simplicity, only one component is shown here. The switching processes (a)-(d) and (e)-(h) were observed by increasing the field from zero in the direction given by the arrow at the bottom. Both elements were on the same substrate so that the elements could be imaged sequentially in the same field. The field strength is given to the left and right in mT. From ref. [77].

a calibration sample, as explained in more detail elsewhere. It is important to note that the shift of the primary beam position is experimentally extremely helpful, since it allows for direct measure of the magnetic field strength. For example, to reproduce a certain field value, the excitation coils of the circuit are simply set to the value that reproduces the previously recorded primary beam position. The small hysteresis of the magnetic circuit, that is encountered, causes no practical problems, since the magnetic field is determined by primary beam position and not by reference to the current to field relationship of the magnetic circuit.

As an exemplary application, the switching behavior of Permalloy microstructures was demonstrated [77], which is illustrated in Fig. 2.7. The Permalloy microstructures were $Ni_{80}Fe_{20}$ (50nm) rectangles on Si(111) wafer produced in a variety of sizes and shapes by electron-beam lithography and lift-off. As reported the observed switching process agrees qualitatively with micromagnetic calculations [81], even though the sizes and field directions considered in the calculation are quite different. Most importantly, the results clearly show that SEMPA measurements in strong magnetic fields can be accomplished. So far, 37 mT were the largest fields that could be produced by the present setup. Larger fields were not applied due to limitations of the excitation current caused by overheating and due to flux leakage of the magnetic circuit. Up to the maximum field of 37 mT no losses of spin signal or SEM resolution were detected, which indicates that the field strength limit for in-field SEMPA measurements should be encountered at considerably larger fields.

In summary, the simple idea that locally confined magnetic fields combined with strong electric fields was described. a miniature magnet consisting of a magnetic circuit and a quadrupole was developed for the in-field measurements which allows the direct observation of switching processes of (ultrathin film or microstructures) by SEMPA. The magnetic field distribution was analyzed by numerical simulation, where the in-plane component is quite homogeneous and the out-of plane component is only a few percentage in the center of the gap. The in-field SEMPA measurements were demonstrated on the switching process of Permalloy rectangles.

2.3 Optical technique for T domains observation

A few imaging techniques are known to allow the observation of antiferromagnetic domains, such as neutron and X-ray diffraction [50, 82–84], and optical [50, 51, 85, 86] techniques. A recent developed technique, X-ray photoemission electron microscopy (XPEEM) [87] with linear dichroism, allows to observe the surface AFM domains by determining the AFM axis (Néel axis). To determine T-domains of NiO(001) single crystal an optical technique is applied *in situ* at present work.

The principle of the optical measurements [52] is illustrated in Fig. 1.5. As mentioned in section 1.3, for the rhombohedral deformation of NiO crystal below T_N causes crystal T(win) domains, the surface normals of T-domains I and II are slightly different. With the incidence of parallel light, the mirror reflection from domain I and II are slightly different which causes intensity contrast on the location of T-wall. With this reason some of T-walls can even be seen with the unaided eye. The contrast of a T-wall performs a straight line in NiO(001) surface. Since the T domains of NiO(001) single crystals are associated with antiferromagnetic ordering, the contrast of T-wall disappears at temperature above T_N and reappears at temperature below T_N .

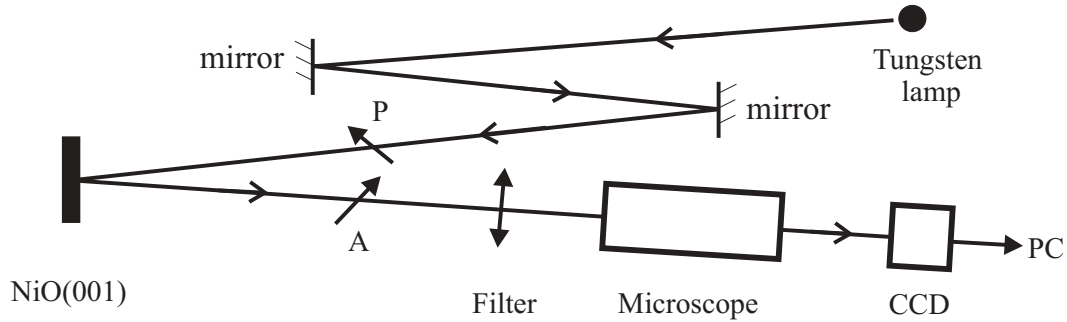


Figure 2.8: Schematic representation of the setup for the observation of T domains. P and A are polarizer and analyzer.

The setup of this optical technique was performed in “MOKE” chamber. The schematic representation of the setup for this optical technique is illustrated in Fig.2.8. It consists of a W light source, a polarizer(P), an analyzer(A), a filter, an optical microscope, a CCD camera, and associated lens. To obtain better signal-to-noise ratio polarized light is used in the experiments. The incident light is nearly along the surface normal but with a small angle about 5° from it. The analyzer is set to be an small angle α from its extinguish position. With the help of the optical microscope a map of T-walls on NiO(001) sample are consequently recorded by a CCD camera. For each measurement it is recorded twice at $+\alpha$ and $-\alpha$. The final image will be the differential one of these two records. As an example a map of T-walls on NiO(001) will be shown in Fig.3.7 in next section.

Chapter 3

Experimental results

The exchange interaction of the FM/AFM system of Fe films epitaxially grown on NiO(001) single crystals is investigated experimentally by using the magnetic domain imaging techniques described in previous chapter 2. The experimental results are presented in this chapter, and all conclusions drawn in the thesis are based on these experimental observations. This chapter is organized as following: Section 3.1 describes the preparations of FM (Fe and Permalloy) films epitaxially grown on NiO(001) single crystals. The ferromagnetic domain structures of as-grown Fe films are characterized by SEMPA and their measurements are presented in section 3.2. The T walls of antiferromagnetic NiO(001) single crystal can be determined by optical observation. The correlation of T domains of NiO(001) single crystal and Fe domains on top of it is studied. They are described in section 3.3. To verify if this correlation is induced by the exchange interaction between Fe film and NiO at interface, a comparison experiments of Fe film and Py film grown on the same NiO(001) single crystal are investigated and described in section 3.4. The last two parts of the chapter are devoted to the study of magnetization reversal processes of Fe films. The MOKE (Magneto-optical Kerr Effect) measurements are presented in section 3.5. The detailed magnetic domain behaviors in external magnetic fields are characterized by SEMPA in last section 3.6. For our knowledge it is the first time to apply SEMPA in studying the domain behaviors of ultrathin Fe film in magnetization reversal processes.

3.1 Preparations of FM/NiO(001) samples

NiO(001) single crystals with two different surface preparations are used in present experiments. Type I: NiO(001) single crystal was cleaved *ex situ*. to obtain an almost fully compensated surface. Type II: NiO(001) single crystal was polished *ex situ*. to obtain an optical smooth surface. In order to release the strain induced by mechanical forces during

the mechanical procedure of cleaving or polishing, NiO(001) single crystals with both types of surface preparations are subsequently annealed at temperature $1400^0 \pm 100^0C$ in an argon atmosphere containing about 10^{-4} part of oxygen. In this heat treatment the trace oxygen prevents the reduction of NiO into Ni. Only resident T-walls were left after the NiO(001) crystal was slowly cooled down to room temperature [52, 88].

Before film deposition the NiO(001) single crystal was annealed in UHV at about 110^0C for several hours to desorb the contaminations for its exposure in air. The type I NiO(001) single crystal was additionally post-treated by cycles of 1kV Ar^+ ions bombardment. The ferromagnetic (FM) films of Fe or Permalloy are epitaxially grown on NiO(001) single crystals by electron beam assisted thermal evaporation. During film depositions the NiO(001) substrates are always at room temperature. The evaporator sources are cut from high purity (99.99% both for Fe or Py) metal wires with diameter of 2mm. The film thickness can be estimated with a Quartz microbalance by multiplying the deposition time and evaporation rate. The normal evaporation rate used in the experiments is between 0.05 and 0.15 nm/min. The base pressure of the preparation chamber is about 5×10^{-11} mbar. The pressure during film deposition is 1×10^{-10} mbar for Fe film evaporation and 9×10^{-11} mbar for Py film.

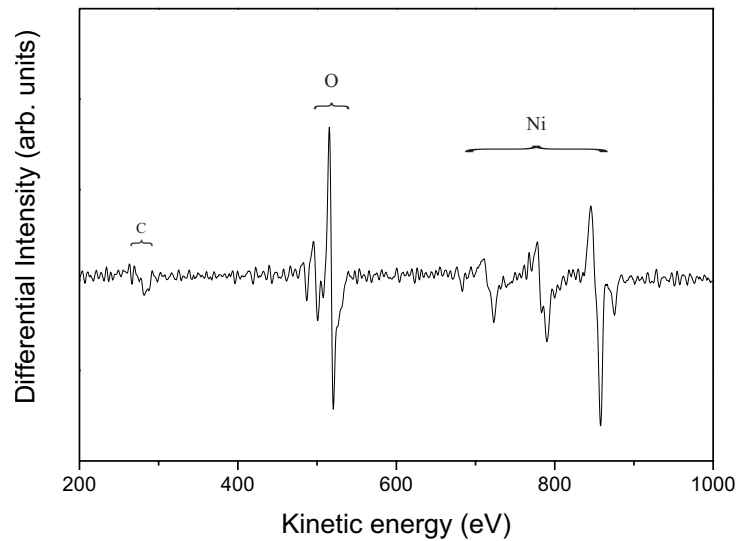


Figure 3.1: An Auger spectrum obtained from a NiO(001) single crystal.

The chemical composition is characterized by Auger Electron spectroscopy (AES). Fig.3.1 shows an Auger spectrum obtained from a NiO(001) single crystal before FM film deposition. The whole Auger spectrum shifts to right in kinetic energy axis since NiO crystal is an electronic isolator. The magnitude of the energy shift depends on the density of incident electron beam. Compared with the Auger spectrum given in AES handbook [89], the dominant peaks of O and Ni can be recognized shown in Fig.3.1, while

the Auger transition peak of C is weak.

In general case of the bilayer system, the Auger intensity of uniform coverage material I_{cov} and substrate material I_{sub} can be written as:

$$I_{sub} = I_0 S_{sub} e^{-\frac{t_{cov}}{0.74\lambda}} \quad (3.1)$$

$$I_{cov} = I_0 S_{cov} (1 - e^{-\frac{t_{cov}}{0.74\lambda}}) \quad (3.2)$$

where I_0 represents the intensity of incident electron beam. t_{cov} denotes the thickness of coverage. λ denotes the mean-free-path of Auger electrons in coverage material, and the factor 0.74 means that the Auger electrons collected by CMA have 42° from sample surface normal where $\cos 42^\circ = 0.74$. S_{sub} and S_{cov} represent the relative sensitivity factors of substrate and coverage materials, respectively. Here the relative sensitivity factor S is defined as the ratio between the probability of Auger transition of certain material and the probability of MNN transition of Ag at other constant measurement parameters (e.g. the primary beam energy, beam current etc.).

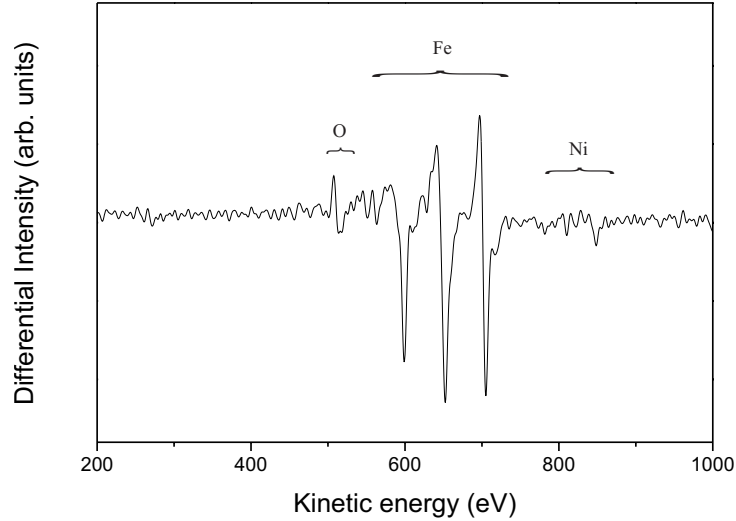


Figure 3.2: A typical Auger spectrum obtained from a 20ML Fe film grown on NiO(001) single crystal.

Fig.3.2 shows a typical Auger spectrum obtained from a 20ML Fe film grown on NiO(001) single crystal. Three strongest peaks of LMM transitions of Fe are recognized at 592eV, 647eV, and 701eV. The peaks of Auger transition of O and Ni come from the NiO substrate, and their Auger intensities are weak for 20ML Fe coverage. The peak of Auger transition of C is very weak.

Fig.3.3 shows a typical Auger spectrum obtained from a 1.25nm Permalloy (Fe at 20% and Ni at 80%) film grown on NiO(001) single crystal. The peaks of LMM transitions of

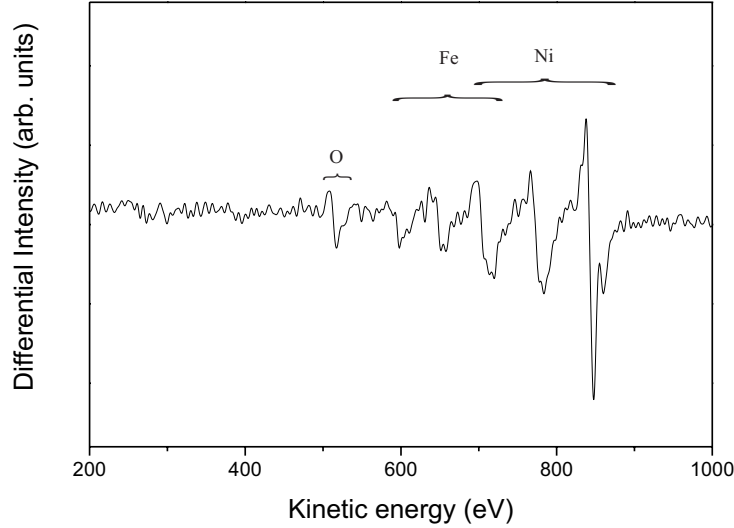


Figure 3.3: A typical Auger spectrum obtained from *Permalloy(1.25nm)/NiO(001)*.

Fe and Ni are dominant. There are an overlap peak at 705eV and two separated peaks of LMM transitions both of Fe at 592eV and 647eV and of Ni at 774eV and 840eV. The Auger intensity of Ni consists of two parts: main contribution from Permalloy and a partial contribution from NiO(001) substrate. The peak of Auger transition of C is also very weak.

3.2 Domain structures of as-grown Fe/NiO(001)

The magnetic domain structures of Fe films grown on NiO(001) crystals are characterized by SEMPA measurements at room temperature. No magnetic field was applied during film deposition, and no field cooling procedure was dealt after film growth.

3.2.1 Fe domains

Fig.4.5 shows a typical SEMPA measurement of 10 atomic monolayer (ML) Fe film epitaxially grown on NiO(001). The kind of type I NiO(001) single crystal, cleaved-and-annealed, is used in this experiment. Two magnetic images and one surface morphology image are obtained simultaneously in one SEMPA measurement as is shown in Fig.4.5 (A), (B) and (C), respectively. As mentioned in section 2.1, the asymmetry \vec{A} determined by the LEED spin detector is proportional to the magnetization $-\vec{M}$ of Fe film, so the acquired magnetic images (Fig.4.5(A) and (B)) directly represent the magnetic domain

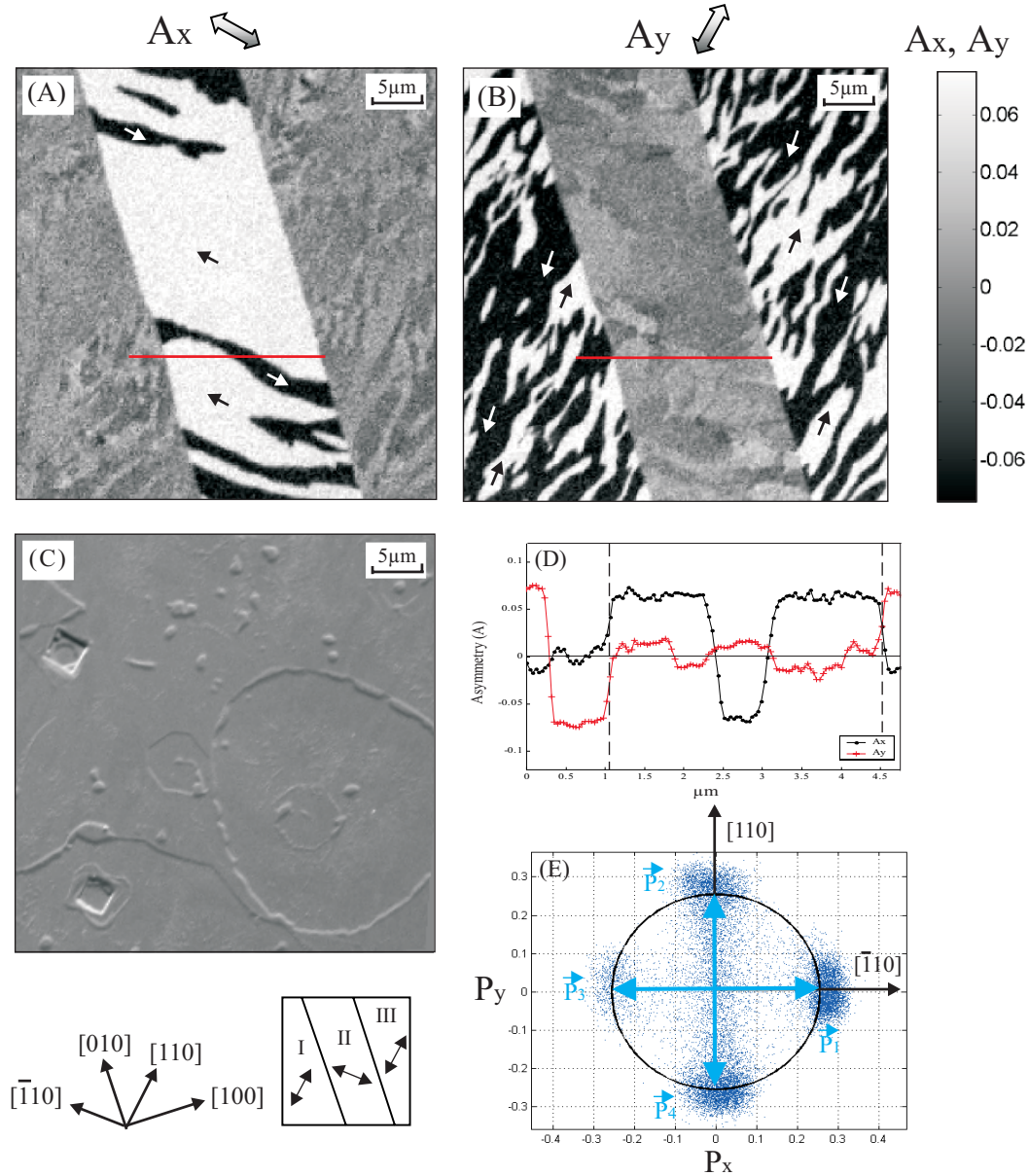


Figure 3.4: A typical SEMPA measurement of 10ML Fe film grown on NiO(001) single crystal. (A) and (B) represent the magnetic domains of Fe film in the asymmetry components of A_x and A_y , respectively. (C) shows a surface morphology image obtained simultaneously by SEMPA measurement. (D) shows a line profile. (E) shows the spin histogram of Fe domains. The coordinates used here are corresponding to the orientation of NiO(001) single crystal. See text for explanation.

structures of Fe film epitaxially grown on NiO(001) single crystal. Fig.4.5(A) and (B) show the unique domain pattern in ways of orthogonal asymmetry components A_x and A_y . At present geometry of SEMP setup, both of asymmetry components A_x and A_y are lying in NiO(001) surface plane. The axes of asymmetry A_x and A_y are oriented along $[\bar{1}10]$ and $[110]$ directions which indicated as double hollow arrows on top of Fig.4.5(A) and (B), respectively. The coordinates used here are corresponding to the orientation of NiO(001) single crystals. Dark or white contrast in the magnetic domain images represents the magnitude of asymmetry. The quantity is given by the same grey level as a grey-scale bar indicated at right panel in Fig.4.5(B). Fig.4.5(A) and (B) use the same grey-scale bar.

Straight domain walls along $[010]$ direction are clearly visible in magnetic domain images of Fe film shown in Fig.4.5(A) or (B). These walls are extended to a length of several millimeter and related to crystalline axes of NiO(001) single crystal. The magnetizations of Fe film on adjacent regions separated by a straight wall are drastically different. For simplicity of the description, these straight walls are sketched as straight lines, and the regions separated by them are named regions I, II and III, seen in the panel under the bottom of Fig.4.5(C). The domains on regions I, II and III have irregular wall shapes. The magnetic domains of Fe film on region II have dark or white contrast in asymmetry component A_x (seen in Fig.4.5(A)), and grey in another asymmetry component A_y (seen in Fig.4.5(B)). The spins of Fe domains on region II are indicated as arrows in Fig.4.5(A). The magnetization of Fe film on region II is oriented along the asymmetry axis of A_x , which is parallel or anti-parallel to $[\bar{1}10]$ direction. The local easy axis of Fe film on region II is oriented along $[\bar{1}10]$ direction. Using the similar analysis, the domains of Fe film on regions I and III have dark or white contrast in asymmetry A_y (seen in Fig.4.5(B)) and grey in asymmetry A_x (seen in Fig.4.5(A)). The spins of Fe domains are indicated as arrows in Fig.4.5(B). The local easy axes of Fe film on regions I and III are oriented along $[110]$ direction. The easy axis of Fe film has 90° rotation across the straight wall as indicated double arrows on the sketch panel under the bottom of Fig.4.5(C).

To accurately obtain the directions of Fe spins, a spin histogram of Fe domains is plotted in Fig.4.5(E). The horizontal and vertical axes denote spin polarization P_x and P_y , where their axes are along $[\bar{1}10]$ and $[110]$ directions, respectively. According to equation 2.1, spin polarization $\vec{P} = \frac{1}{S} \cdot \vec{A} = 4\vec{A}$. Each pixel of domain images of Fig.4.5(A) and (B) corresponds to a polarization vector in Fig.4.5(E). Due to the unsharpness of domain walls, the vector of spin polarization of Fe film has a cluster-like distribution in spin histogram. The spin polarization is defined as a vector \vec{P}_i ($i = 1, 2, 3$ and 4) starting from origin point to the center of spin cluster, which is illustrated as the blue arrows in Fig.4.5(E). P_1 and P_3 represent the spin polarization of Fe film on region II, which are oriented exactly along the axis of $[\bar{1}10]$ with a deviation of $\pm 12^\circ$. P_2 and P_4 represent the spin polarization of Fe film on regions I and III, which are oriented along the axis of $[110]$ with a deviation of $\pm 12^\circ$.

According to the definition by Chikazumi [90], magnetic domain walls are classified into two categories: 180° walls separating two oppositely magnetized domains, and 90° walls separating two domains whose magnetizations make a 90° angle. The Fe domain

walls with irregular shapes in regions I, II and III are 180° walls, and the straight walls are 90° -type walls. Fig.4.5(D) presents a line profile. The asymmetries A_x and A_y are plotted as a function of lateral distance indicated as the red solid lines in Fig.4.5(A) and (B). The vertical dash line in Fig.4.5(D) indicates the region with a straight wall. It separates two domains with magnetization along $[\bar{1}10]$ and $[110]$ directions, which is 90° -type wall. The Fe domain wall with irregular shape on region II separates two domains with opposite magnetizations along $[\bar{1}10]$ and $[1\bar{1}0]$ directions ($[110]$ and $[\bar{1}\bar{1}0]$ directions on regions I and III), which is 180° wall. Owing to the high signal-to-noise ratio, one notices that the asymmetry A_y on region II (between dash lines in Fig.4.5(D)) is not “zero”, which indicates small modulation of Fe spins. This spin modulation represents a kind of fine structures of Fe domains, which is clearly visible on region II in Fig.4.5(A) and on regions I and III in Fig.4.5(B).

The magnetic domain structures shown in Fig.4.5 are quite general for 10ML Fe film grown on NiO(001) single crystal. The appearance of straight 90° -type wall is a characteristic for this Fe/NiO(001) sample, which is drastically different from the domains of Fe films grown on other nonmagnetic substrates (“free” Fe films) [91–94]. Instead of such kind of straight and long 90° domain wall, the magnetic domains of “free” Fe films are nearly one single domain [91, 92], or very small multidomains [92–94]. Finally it is worth to point out that the magnetic domains and easy axes of Fe film have no correlation to the sample surface morphology seen in Fig.4.5(C). These unusual domain structures of Fe film sample should correlate to the exchange interaction between ferromagnetic Fe film and underlying antiferromagnetic NiO(001) substrate.

3.2.2 Thickness dependence

For ferromagnetic ultrathin films grown on single crystal substrates, one of their most remarkable features is that 2D ferromagnetism is stabilized exclusively by the balance of variety magnetic anisotropies [95]. For a “free” FM film the balance is the competition between the surface anisotropy [96–100] and the shape anisotropy which determines the easy magnetization direction [94]. In Fe/NiO(001) system, the 2D ferromagnetism can be stabilized at Fe thickness from 4ML up to ~ 30 ML. In this film thickness range the magnetic domains of as-grown Fe films have very stable patterns at room temperature. The detailed information of the magnetic domains are presented in the following.

In present SEMPA setup the Fe film deposition and the SEMPA measurements are performed in SEMPA system described in 2.1.1. By using SEM mode the imaging area can be positioned exactly at the same location for SEMPA measurements with different film thickness t_{Fe} . Fig.3.5 shows the typical magnetic domains of as-grown Fe films on NiO(001) single crystals at $t_{Fe} = 14$ ML and 24ML. Fig.3.5(A) and (B) are magnetic domain images of Fe film at $t_{Fe} = 10$ ML with two asymmetry components A_x and A_y . Fig.3.5(C) and (D) are magnetic domains of Fe film at $t_{Fe} = 24$ ML. Similar to that shown in Fig.4.5, the domains of Fe films at both thickness have the common features: straight

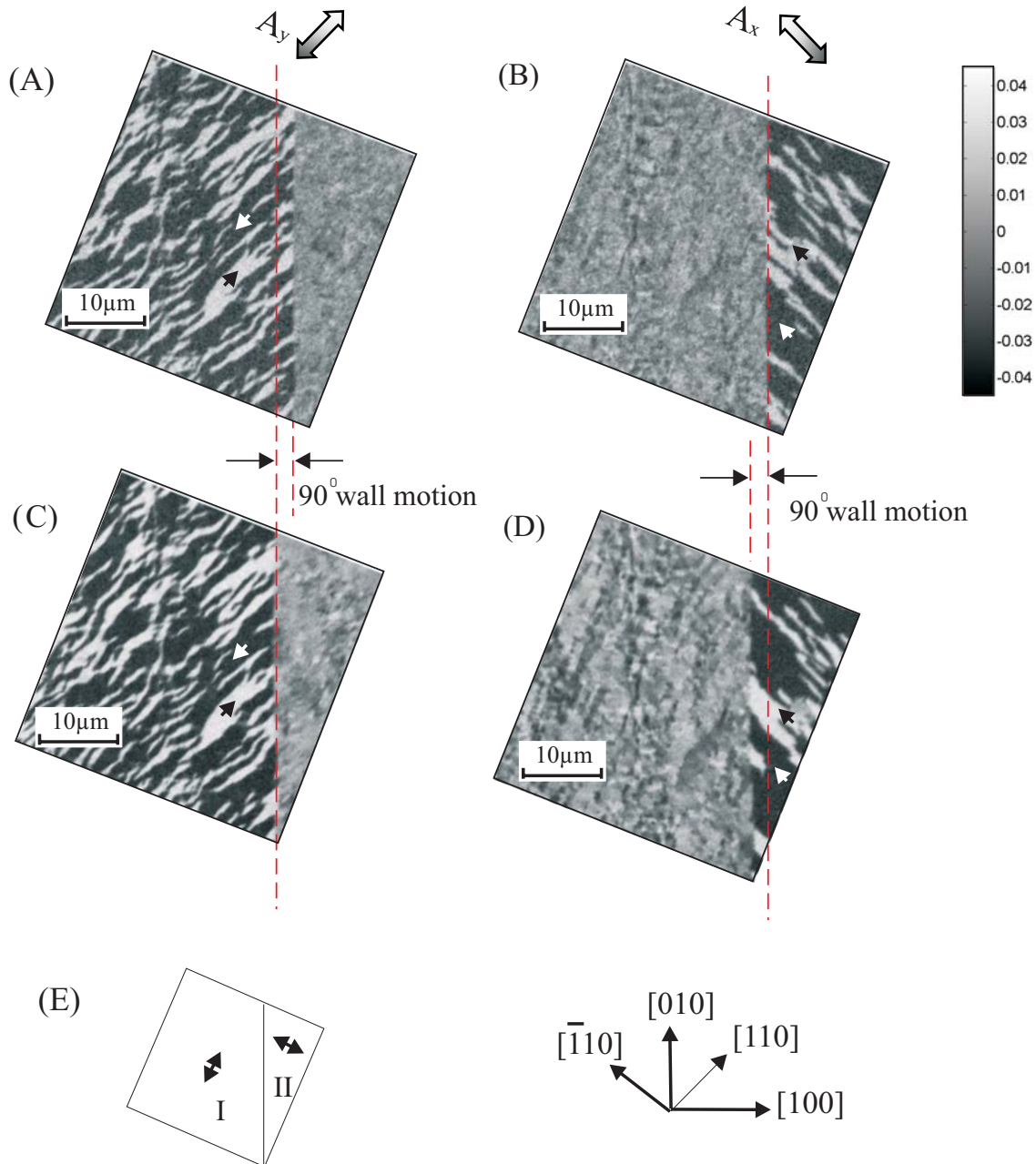


Figure 3.5: *Fe domain configurations of the Fe/NiO(001) samples. (A) and (B) are magnetic domains in two orthogonal asymmetries components at $t_{Fe} = 14ML$. (C) and (D) are magnetic domains at $t_{Fe} = 24ML$. The 90° -type wall along $[010]$ direction has a motion of about $1.8\mu m$. (E) sketch of two straight walls and easy axes of Fe film.*

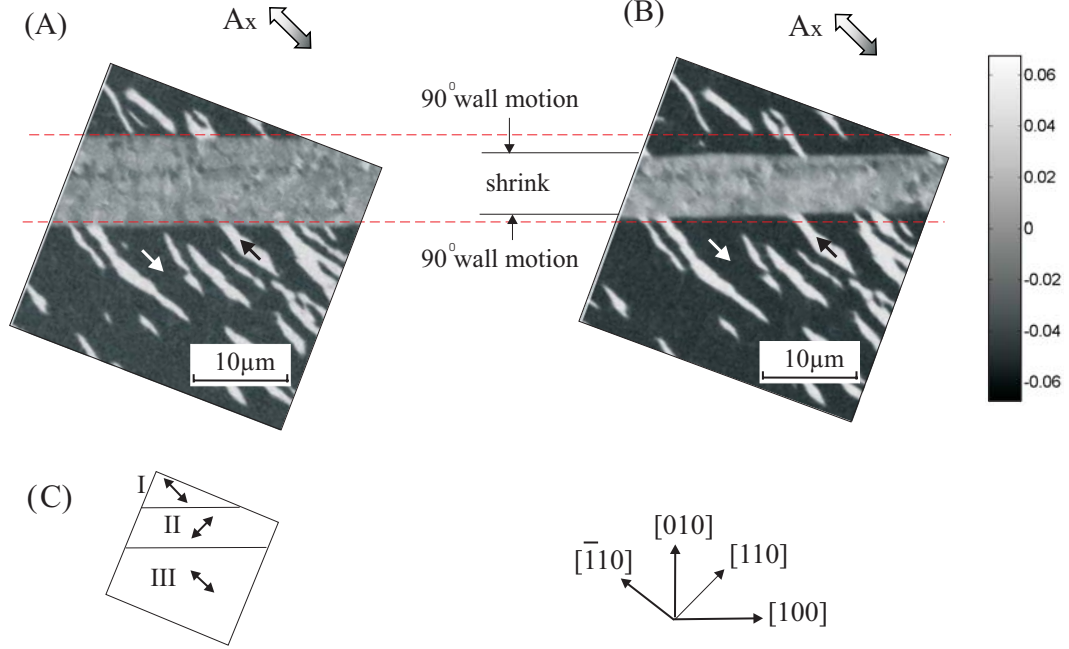


Figure 3.6: (A) and (B) are Fe domains of Fe/NiO(001) samples at $t_{Fe} = 14ML$ and $24ML$, respectively. (C) sketch of straight 90° -type walls and easy axes of Fe film.

90° -type walls along $[010]$ direction and 180° walls with irregular shapes in between. With increasing t_{Fe} from 14ML to 24ML, the magnetic domains on regions I and II have almost the same patterns except that their wall boundaries with irregular shapes become shaper. It is known from the SEMPA measurements that at most of the straight 90° -type walls remain the same shapes and stay at their original locations with increasing Fe thickness, while a fraction of straight 90° -type walls are shifted to new positions. Fig.3.5 shows a case of wall shift. The location of the straight 90° -type wall has a shift of about $1.8\mu m$ with increasing t_{Fe} from 14ML to 24ML. Since the easy axis of Fe films on regions I and II are orthogonal, a direct effect for this wall motion is that the direction of local Fe spins rotate 90° on the wall motion area. The wall shift does not simply depend on the thickness of Fe film. Fig.3.6 shows another case of wall motion at the same sample. Fig.3.6(A) and (B) represent the magnetic domains of Fe films at $t_{Fe} = 14ML$ and $24ML$, respectively. With increasing t_{Fe} the straight 90° -type walls move towards opposite directions, while their shifts from their original positions are not equal. This shows that the wall motion of straight 90° -type walls does not only depend on Fe film thickness but also on local features (such as stress, defect et al.). As is to be known later, the straight 90° -type walls of Fe film are correlated to T-walls of underlying NiO(001) single crystal. The observation of wall shift indicates that T-domains of NiO crystal can be modified by Fe film.

In summary the magnetic domains of as-grown Fe films on NiO(001) single crystals (type I) are studied by SEMPA measurements. Straight 90° -type walls oriented along [010] or [100] direction are observed, and the Fe domains with irregular shapes are 180° -type walls. The easy axis of Fe film is oriented along $[\bar{1}10]$ (or [110]) direction, and it has 90° rotation across the straight wall. With increasing the thickness of Fe film, the magnetic domain remains almost unchanged except a small wall motion for a fraction of straight 90° -type walls.

3.3 The correlation of Fe domains and T-domains

To understand the exchange interaction the magnetic domains of both Fe film and NiO(001) single crystal should be characterized. As already shown in previous, the Fe domains are characterized by SEMPA. The T-walls of NiO(001) single crystal can be detected by optical observation described in section 2.3.

Fig.3.7(A) illustrates an image of T-walls on a type II, polished-and-annealed, NiO(001) single crystal. Many straight and scratch-like lines which oriented along [110], $[\bar{1}10]$ and [010] directions are observed. Since the T-walls are associated with the antiferromagnetic properties of NiO(001) crystal, they disappear when the NiO(001) single crystal is heated up to above T_N , and reappear after cooling down from T_N . The observed straight-line contrast in Fig.3.7(A) indicates a T-wall which oriented along the same direction on NiO(001) surface. Instead of a single domain, the NiO(001) single crystal is divided into many T-domains. A map of T-walls is sketched as straight lines and shown in Fig.3.7(B). As described in section 1.3, the optical observation is not able to characterize the spins of NiO crystal, so the three easy directions of NiO spins in FM planes are still not yet determined. In order to know if the T-walls in bulk NiO crystal are modified after the deposition of Fe film, the NiO(001) substrate was partially deposited by Fe film steps. The thickness of Fe steps are indicated as thickness cartoon in the panel at the bottom of Fig.3.7(A). T-walls oriented along [110], $[\bar{1}10]$ and [010] directions are also observed on the area with Fe coverage. At the boundary of regions with and without Fe coverage, no wall shift is observed. In conclusion no modification of T-walls in bulk NiO(001) crystal are observed upon the deposition of ultrathin Fe film.

To obtain the correlation of Fe domain and T-domain in sample of Fe film grown on NiO(001) single crystal, the domains of both materials should be determined domain by domain, which means that the SEMPA measurement and optical observation should be carried out at the same imaging area. This combination is possible by performing both measurements on an identical imaging area with the helps of their topography images. In SEMPA measurements the topography image is simultaneously obtained with the magnetic domain images. In optical observation it is equal to a normal optical microscopy when the incident light is unpolarized. Then the acquired image is a normal

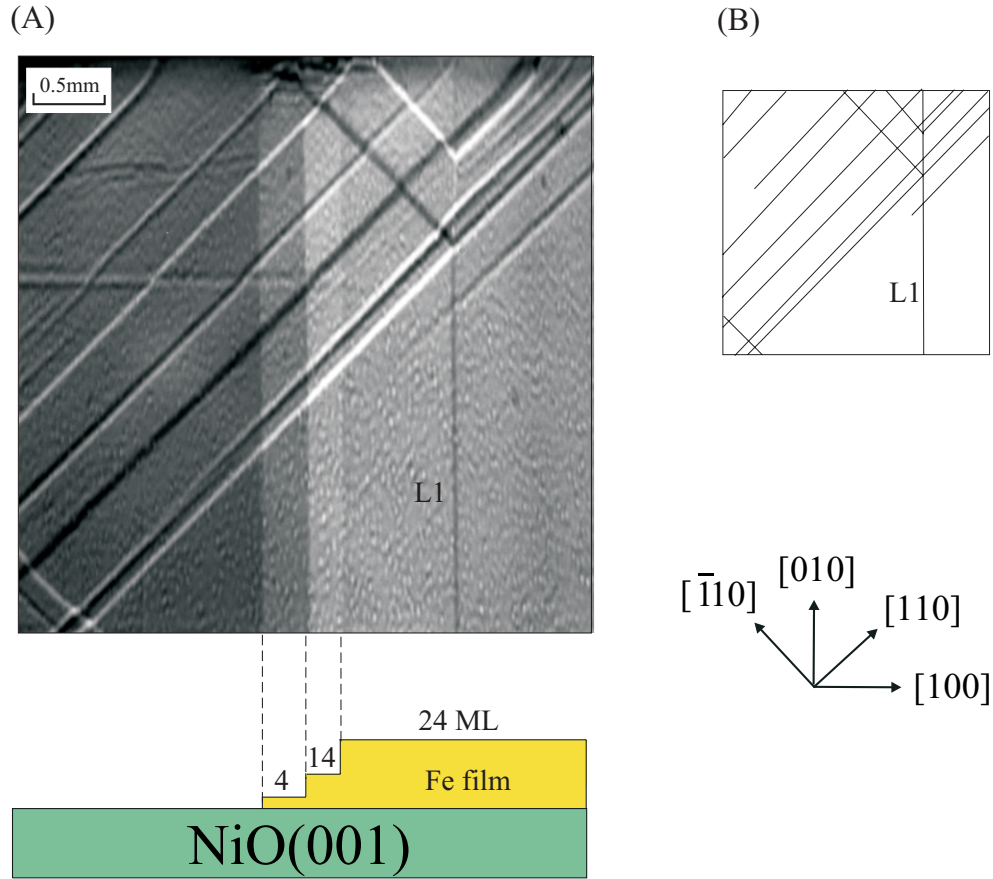


Figure 3.7: (A) An image of T-walls on polished and annealed NiO(001) crystal by using optical technique. The NiO(001) crystal is partially covered with Fe film steps, shown as the thickness cartoon at bottom. (B) A sketch for T-domain walls of (A).

topography image. With carefully positioning the imaging area, the measurements can be accomplished on the same sample region.

Fig.3.8 shows combined measurements by SEMPA and optical observation. Fig.3.8(A) indicates the T-domains by optical observation which has been explained previously. Fig.3.8(B) shows the magnetic domains of 24ML Fe film grown on NiO(001) single crystal. A view of zoom in image is shown in Fig.3.8(C). The imaging region of SEMPA measurement (Fig.3.8(B)) is positioned at a region marked as square at top-right corner in Fig.3.8(A). In this imaging region there are T-walls oriented along [010], [110] and $[\bar{1}10]$ directions. It is found out that in the middle of the imaging area a T-wall oriented along [010] direction corresponds to a straight 90° -type wall of Fe film at the same position and along the same direction. In another word the straight 90° -type wall of Fe film is a representation of T-wall in NiO(001) single crystal. But for the T-walls along [110] or

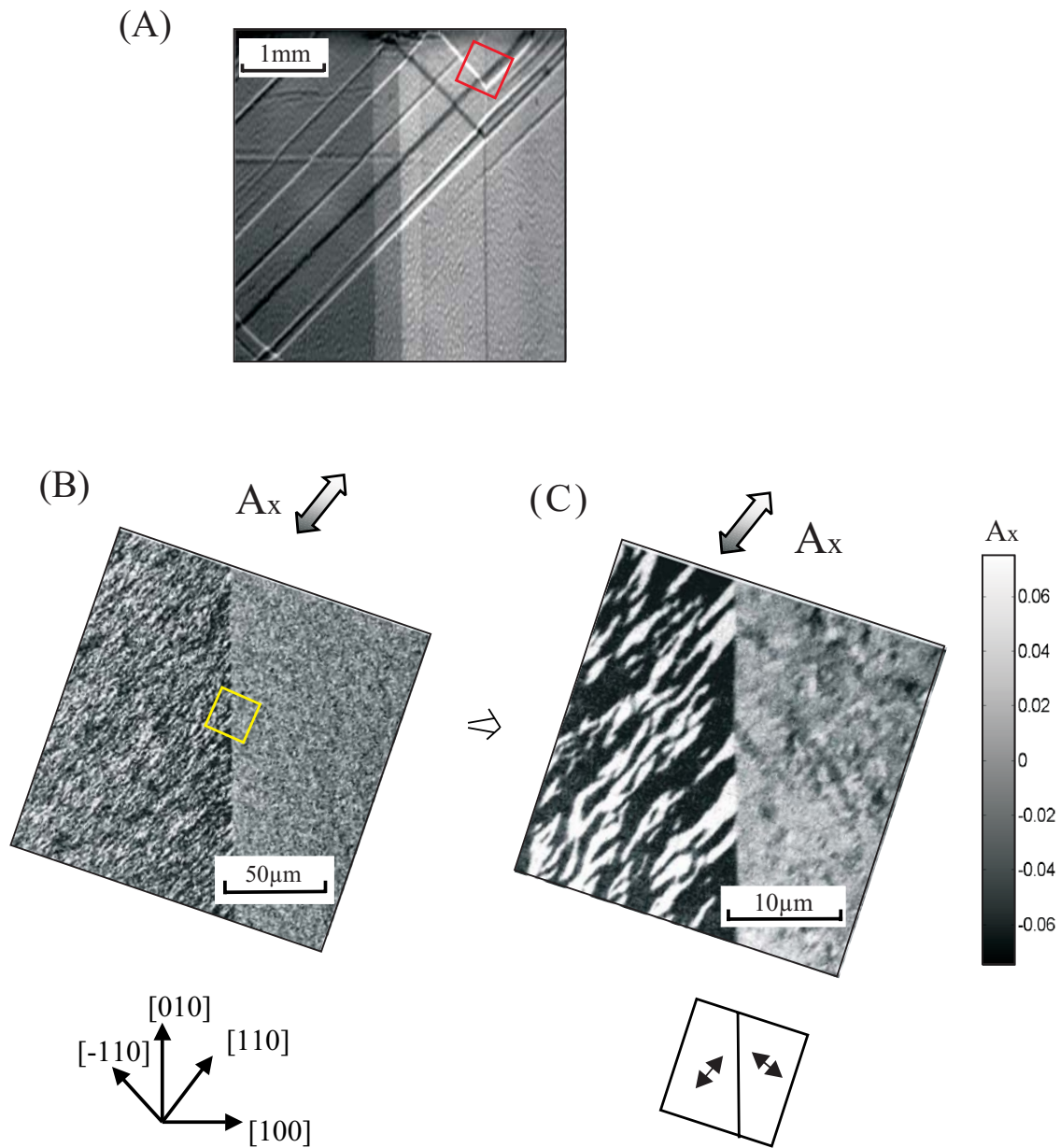


Figure 3.8: A combined measurement of Fe (24ML) domains and T-walls of NiO(001) of the Fe/NiO(001) sample by using SEMPA and optical technique. (A) The image of T walls by optical technique. (B) Fe domains on the imaging area of square P_1 by SEMPA measurement, and (C) the view of the zooming in.

$[\bar{1}10]$ direction, no any kind of straight 90° -type wall of Fe film is observed to be related to the T walls oriented along $[110]$ or $[\bar{1}10]$ direction. The T-walls along these directions on NiO(001) single crystal are absent in magnetic domains of Fe film.

With the determination of T-wall, the magnetic domains of Fe film grown on region I or II in Fig.3.8(C) represent the magnetic domains of Fe film grown on a single T-domain. Either on region I or II only the Fe domains with 180° -type walls are presented. The easy axis of Fe film on a single T domain (region I or II) is unique, which is indicated as double arrows in the panel on bottom of Fig.3.8(C). These domain structures reveal that the Fe film grown on a single T-domain has uniaxial anisotropy which will be further confirmed by MOKE measurements in next section.

The correlation of Fe domains and T-domains can be phenomenologically explained by the collinear coupling between the Fe spins and AFM spins at the interface. It based on three assumptions: 1). It assumes that the T domains of NiO(001) single crystal are identical both in bulk and at the interface. 2). Since ultrathin Fe film used here is $<24\text{ML}$ (3.5nm), it is far to the width to form a Bloch wall (200-250 nm) [101]. It assumes that the spins of Fe film are isotropic along film thickness direction. 3). It also assumes that the Fe spins and AFM spins are collinear coupling at the interface. Because the Fe spins and AFM spins in bulk NiO crystal are not parallel, the spins on one material or both should be rotated at the interface for the interaction of exchange coupling. As a simple approach, this section only presents the case that the spins of Fe film are aligned along its crystallographic easy axis $[110]$ (or $[\bar{1}10]$) direction and the AFM spins are rotate at the interface. A general model with the spin rotations in both materials will be discussed later in section 4.1.

Fig.3.9 illustrates the spin model of two crystal units of NiO which containing a T-wall plane and two adjacent T-domains. Only the Ni ions are shown in the units and the O ions are not considered. Fig.3.9(A) shows the case of a (100) T-wall plane which terminates a T-wall along $[010]$ direction. It is equal to the case with a (010) T-wall plane which terminates a T-wall along $[100]$ direction. Fig.3.9(B) and (C) shows the case of a $[\bar{1}10]$ T-wall plane which terminates a T-wall along $[110]$ direction. Since T domains are the results of NiO(001) crystal twin by the rhombohedral deformation below T_N , the T-wall plane is a crystal mirror plane for two adjacent T domains [52]. The possible FM planes in left and right T-domains are symmetric and parallel to the filled $\{111\}$ planes in left and right T-domains, as is indicated in Fig.3.9 (A), (B) and (C). As mentioned in Fig.1.4, the AFM spins (the spins of Ni ions) lie in FM plane and along one of possible Néel axes which are indicated as solid lines in Fig.3.9. The AFM spins at interface rotate from their easy axis towards $[110]$ (or $[\bar{1}10]$) direction and collinear couple to Fe spins.

In the case of a T-wall along $[010]$ direction shown in Fig.3.9(A), at interface the AFM spins in left T domain rotate 30° from easy axis to $[110]$ direction and collinear couple to Fe spins. The AFM spins in right T domain rotate -30° from easy axis to $[\bar{1}10]$ direction and collinear coupled to Fe spins. As the results of this spin modification: 1). A straight 90° -type wall along $[010]$ direction is formed on Fe film at the location of T-wall; 2). The

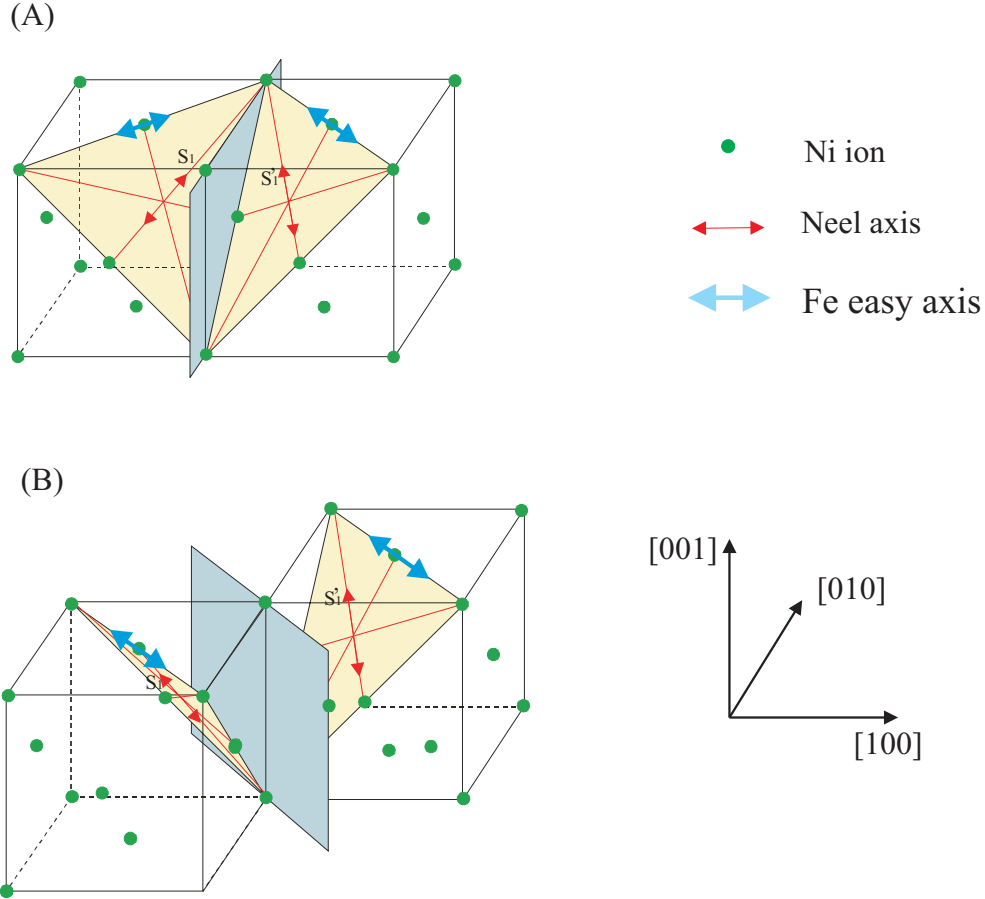


Figure 3.9: Spin models for the exchange coupling of Fe film grown on NiO(001) single crystal. Only the Ni ions are shown. Spins of Ni ions lie in FM sheet indicated as filled $\{111\}$ planes. The Ni spins at interface are rotated and collinear coupled to Fe films indicated as the double arrows along $[110]$ or $[\bar{1}10]$ direction. (A) shows the case with a T-wall along $[010]$ direction. A straight 90° -type wall of Fe film is formed at the position of T-wall. (B) shows the case with a T-wall along $[\bar{1}10]$ direction. Any kind of straight 90° -type wall along $[110]$ or $[\bar{1}10]$ direction is absent on Fe domains.

spins of Fe film are pinned by exchange coupling. The four-fold symmetry of Fe film is broken by the this pinning effect, which explains the uniaxial anisotropy of Fe film grown on a single T domain.

In the case of a T-wall along $[\bar{1}10]$ direction it is shown in Fig.3.9(B). At interface the spins of AFM spins in left T domain rotate 30° to $[\bar{1}10]$ direction and collinear couple to Fe spins. The AFM spins of right T-domain rotate -30° to $[\bar{1}10]$ direction and collinear couple to Fe spins. In this configuration the spins of Fe film on left and right T-domains are

parallel (or antiparallel) and parallel to T-wall oriented along $[\bar{1}10]$ direction. No contrast of straight 90° -type wall along $[\bar{1}10]$ direction is expected on Fe film. This explains why the T-walls oriented along $[110]$ or $[\bar{1}10]$ direction are absent on Fe domains.

In summary, the magnetic domains of Fe films and T-walls of NiO(001) single crystals are studied by SEMPA measurements and optical observations. The T-wall oriented along $[100]$ (or $[010]$) direction presents a straight 90° -type wall on Fe film at the same position; the T-wall along $[110]$ (or $[\bar{1}10]$) direction is absent on Fe domains. It has uniaxial anisotropy of Fe film grown on a single T-domain. The correlation of Fe domains and T-domains is explained by the collinear coupling between the Fe spins and AFM spins at the interface.

3.4 FM grown on type II NiO(001)

As described in previous sections the domains of Fe film grown on type I NiO(001) single crystal are drastically different from “free” Fe film, which is explained as the collinear coupling between the spins of Fe film and AFM spins in NiO crystal at the interface. This section presents the SEMPA measurements of Fe film grown on type II NiO(001) single crystal. Another purpose is to verify if the distortion of lattice structure in NiO(001) would modify the anisotropy of FM films.

Since the lattice of NiO crystal has slightly rhombohedral distortion below T_N , the 2D lattice of NiO(001) surface is distorted along their diagonal directions $[110]$ and $[\bar{1}\bar{1}0]$. The lattice of Fe film epitaxially grown on NiO(001) is subsequently distorted along diagonal directions. The distortion $\delta = \frac{\Delta l}{l}$ along two diagonal directions can be estimated from the rhombohedral angle α (shown in Fig.1.5). At room temperature $\delta \approx 1.2 \times 10^{-3}$, which is much larger than the magnetostriction constant of bulk Fe, 20.7×10^{-6} along $[100]$ and -21.2×10^{-6} along $[111]$ direction [102]. This distortion on NiO(001) lattice may cause magnetostriction effect in pseudomorphic Fe film and subsequently modify the anisotropy of Fe film. As is known that the magnetostriction coefficient of bulk Permalloy (Py) film is essentially zero at the composition of 81 at.% Ni and 19 at.% Fe [103, 104]. Thus, Py in its bulk form is insensitive towards structural effects (Here means rhombohedral distortion). Even though the magnetostriction constant of Py might be modified in the ultrathin regime [105, 106], the main tendency should still hold and anisotropy induced by structural effect would be much weaker in Py film than in Fe film.

To allow for a meaning comparison of Py and Fe films, the same substrate of NiO(001) single crystal was used in the experiments. During the deposition of Fe film, part of the crystal was protected from the Fe beam by a shutter in front of the sample. Subsequently the NiFe-film was brought upon the remaining clean NiO surface while the Fe-film was protected by a shutter. As mentioned in section 3.1, the Py film is deposited from a single FeNi alloy (20% at Fe and 80% at Ni) rod.

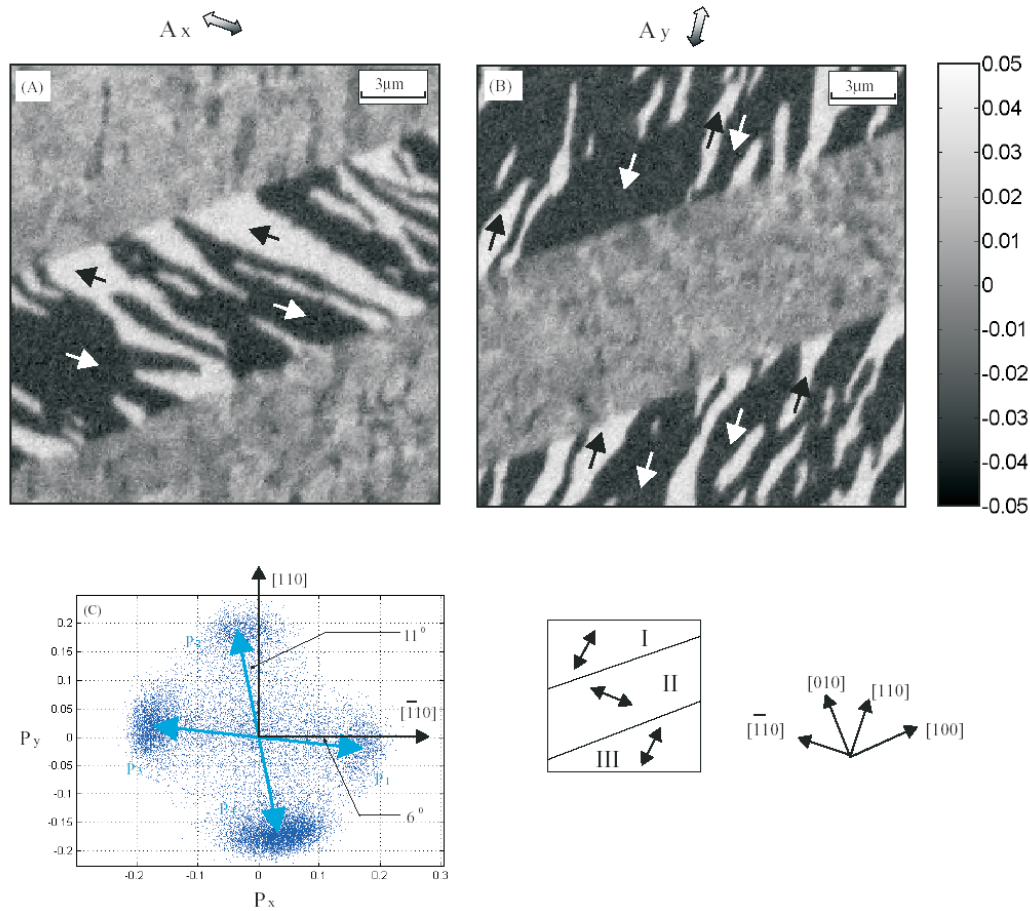


Figure 3.10: Magnetic domains of 14ML Fe film grown on type II NiO(001) single crystal. (A) and (B) represent the Fe domains in two orthogonal asymmetry components A_x and A_y . The axes of A_x and A_y are selected along $[\bar{1}10]$ and $[110]$ directions, respectively. (C) shows the spin histogram of Fe domains. The spins of Fe film on region II are inclined $6^\circ \pm 12^\circ$ from $[\bar{1}10]$ direction; the spins of Fe film on regions I and II are inclined $11^\circ \pm 12^\circ$ from $[110]$ direction.

Fig.4.6 shows the magnetic domains of 14ML Fe film grown on type II NiO(001) single crystal. Fig.4.6(A) and (B) are the Fe domains in two orthogonal asymmetry components A_x and A_y , respectively. The T-domains and easy axes are sketched in the panel at right-bottom corner. The spin histogram is illustrated in Fig.4.6(C), where P_i ($i = 1, 2, 3$ and 4) means the spin polarization of Fe film. P_x and P_y are set to along the directions of A_x ($[\bar{1}10]$ direction) and A_y ($[110]$ direction), respectively. The domain pattern of Fe film on type II NiO(001) shown here is very similar to those on type I NiO(001) (seen in Fig.4.6). Their main features are the same: Straight 90° -type domain walls which corresponds to a T-wall oriented along $[100]$ (or $[010]$) direction; 180° -type walls with irregular shapes on

regions I, II and III; uniaxial anisotropy of Fe film on a single T-domain; the rotation of easy axis across T-wall. One notice that the spin polarization P_i (seen in Fig.4.6(C)) is not along the diagonal directions: $[\bar{1}10]$ and $[110]$, which has an inclined angle. For P_1 and P_3 which is the spin polarization of Fe film grown on region II, they have the inclined angle of $6 \pm 12^\circ$ from $[\bar{1}10]$ direction. For P_2 and P_4 which is the spin polarization of Fe film grown on regions I and III, they have the inclined angle of $11 \pm 12^\circ$ from $[110]$ direction. Since the main features of Fe films grown on both types of NiO(001) single crystals, this small modification of Fe spins is possibly induced by the discrepancy of interface properties of NiO(001) single crystals. As well as the anisotropy of Fe film grown on type I NiO(001) single crystal, the anisotropy of Fe film grown on type II NiO(001) single crystal is also induced by the exchange interaction between the Fe spins and AFM spins in NiO crystal. But it can not be simply explained as the collinear coupling as described in section 3.3. A more general model is needed.

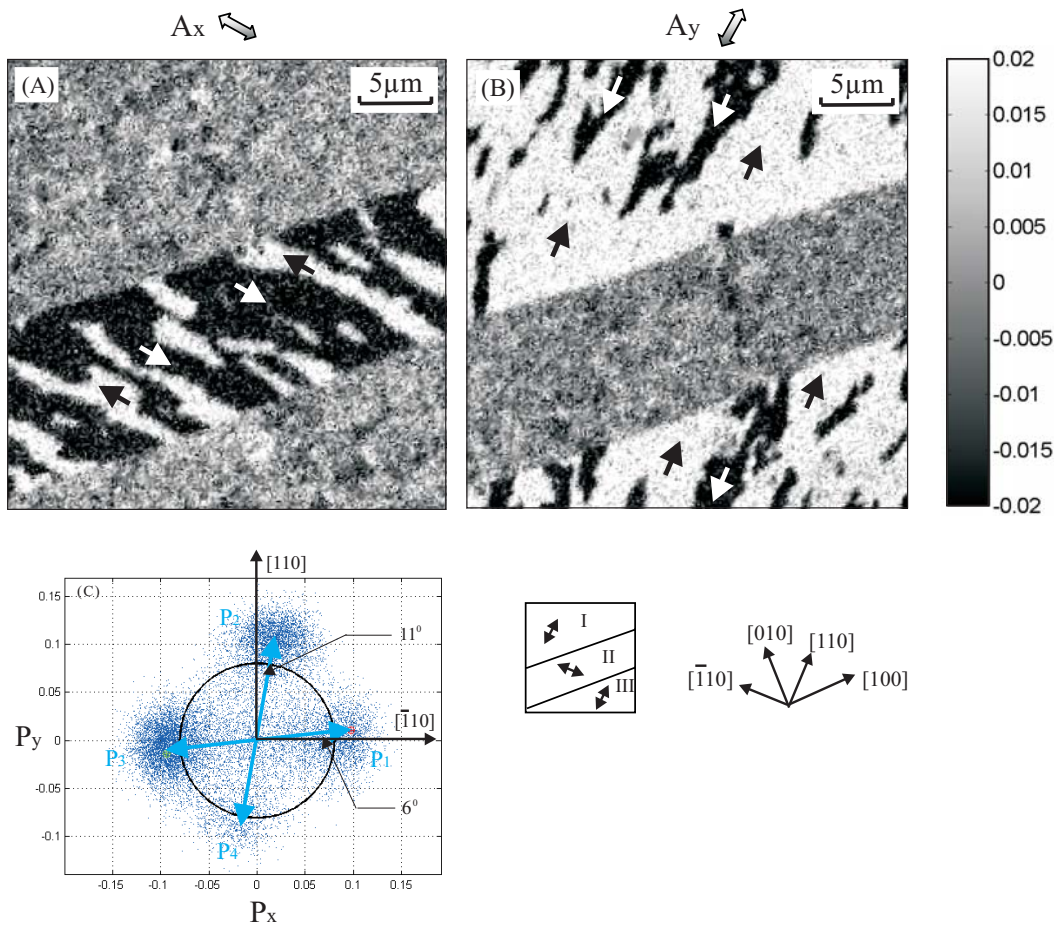


Figure 3.11: Magnetic domain structures of as-grown $Py(1.25nm)/NiO(001)$ by using SEMPA. (A) and (B) are two magnetic images. (C) shows the T-walls of NiO(001) and easy axes of Py film.

Fig.3.11 shows the magnetic domains of 1.25nm Py film epitaxially grown on NiO(001) single crystal. As well as the SEMPA measurements for Fe domains, Fig.3.11(A) and (B) represent the Py domains in orthogonal asymmetry components A_x and A_y . The axes of asymmetry components A_x and A_y are selected along $[\bar{1}10]$ and $[110]$ directions, respectively. In the Py domains, straight 90° -type walls along $[100]$ direction, which correspond to T-walls, are observed. The T-walls and easy axes of Py film are sketched in the panel at right-bottom corner. Compare with the Fe domains shown in Fig.4.6, both of them have very similar domain patterns and the main features of FM domains are exactly the same. Fig.3.11(C) represents the spin histogram of Py domains. P_i ($i = 1, 2, 3$ and 4) indicates the spin polarization of Py film. Because of small magnetic moment ($0.6\mu_B$ for Ni and $2.2\mu_B$ for Fe), the magnitude of the asymmetry of Py film has smaller value than that of Fe film. Apart from the discrepancy of magnitude, the P_i of Py film is also inclined from $[\bar{1}10]$ (or $[110]$) direction. P_1 and P_3 are the spin polarization of Py film grown on region II, and they have an inclined angle of $6 \pm 12^\circ$ from $[\bar{1}10]$ direction. P_2 and P_4 are the spin polarization of Py film grown on regions I and III, and they have an inclined angle of $11 \pm 12^\circ$ from $[110]$ direction.

Based on the domain observations of Fe and Py films epitaxially grown on type II NiO(001) single crystal, one comes back to the question: does the structural distortion in NiO(001) modify the anisotropy of FM film? Since the magnetostriction constant of bulk Permalloy (Py) is zero [103, 104] (though it rises in ultrathin film regime [105, 106]), the structure distortion of NiO lattice should not (or weakly) modifies the anisotropy of pseudomorphic Py film and subsequently its domain structures. In fact the same domain structures are observed for both Fe and Py films epitaxially grown on the same NiO(001) single crystal, which manifests that the structure effect of FM (Fe and Py)/NiO(001) is very weak. Furthermore, the structure distortion only breaks the symmetry along diagonal directions $[\bar{1}10]$ and $[110]$ (corresponding to the orientation of NiO(001)). If one assumes that the structure effect is dominant in ultrathin Py or Fe film, the spin polarization \vec{P} is expected to be along one $[\bar{1}10]$ or $[110]$ direction. The measurements show that this assumption is not the case for FM films grown on type II NiO(001) single crystal. In conclusion, the unusual domain structures of Fe films grown on NiO(001) single crystal are not caused by the rhombohedral distortion of NiO lattice. A plausible reason would be the exchange interaction between the Fe spins and AFM spins in NiO crystal at the interface.

3.5 MOKE measurements

The magnetization reversal processes of Fe films grown on NiO(001) single crystals are carried out by Magneto-Optic Kerr Effect (MOKE). Since the MOKE measurements are done in UHV, no protection layers for Fe film is necessary. It uses S-polarized light

generated by a He-Ne laser diode (650nm). The incident beam has an angle of 45° from sample surface normal. Because the size of the light spot is less than 0.5mm, it is small enough to focus the laser beam on surface region only with a single T domain. The magnetic field, which generated by a pair of electro-magnets outside the chamber, is applied in surface plane. In present geometry the magnetic field is applied parallel to the beam plane (longitudinal MOKE).

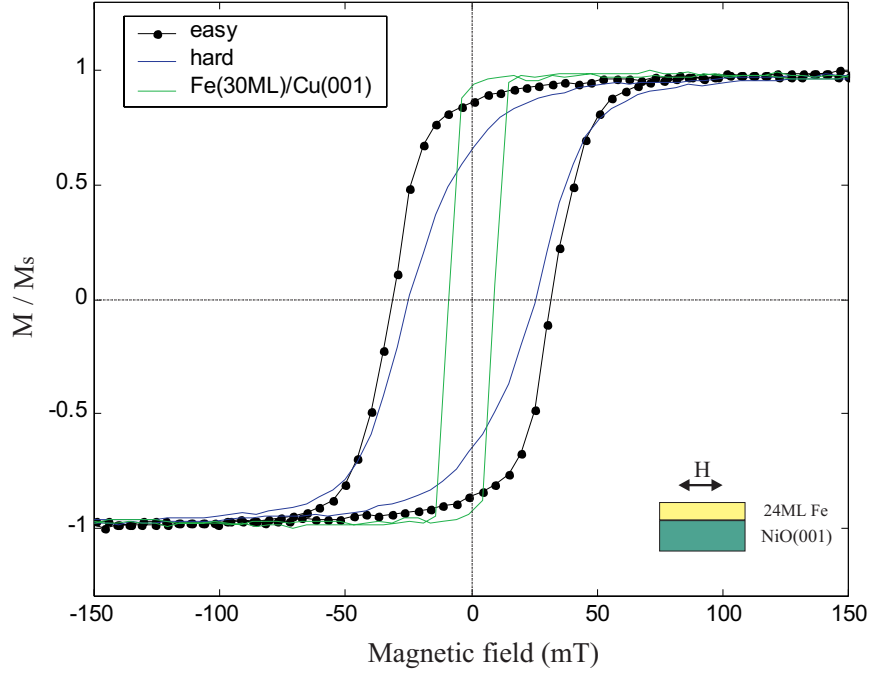


Figure 3.12: The hysteresis loops of $Fe(24ML)/NiO(001)$ by MOKE measurements at RT. The loops in easy and hard axes are symmetric and no exchange bias is observed. ($H_c^{Fe/NiO}$) = 31.6mT. The hysteresis loop of $Fe(30ML)/Cu(001)$ in easy axis is also plotted. ($H_c^{Fe/Cu}$) = 8.9mT. The coercivity of $Fe/NiO(001)$ is enhanced.

With the determination of T-domains, the incident laser beam is focused on a single T-domain, thus a hysteresis loop of Fe film on a single T-domain is given by MOKE measurement. The MOKE measurements in azimuth angle are obtained by rotating the sample in surface plane. It shows that Fe film has uniaxial anisotropy, which agrees to the domain observations of Fe films. Fig.3.12 shows the easy and hard loops obtained from a 24ML Fe film grown on NiO(001) single crystal. Since the as-grown Fe/NiO(001) sample was not dealt by the procedure of field cooling, the macroscopic effect of exchange bias is not expected. No exchange bias is observed. The shape of hysteresis loops are quite symmetric along the field axis, which indicates that the magnetization reversal processes of Fe film are symmetric with increasing and decreasing field. For comparison a sample of ultrathin Fe film grown on a clean nonmagnetic Cu(001) single crystal was prepared

by e-beam evaporator at room temperature. The easy loop of Fe(30ML)/Cu(001) is plotted together with that of Fe/NiO(001) in Fig.3.12. ($H_c^{Fe/NiO}$) and $H_C^{Fe/Cu}$ denote the coercivities of Fe(24ML)/NiO(001) and Fe(30ML)/Cu(001), respectively. From the measurements ($H_c^{Fe/NiO}$) = 31.6mT and $H_C^{Fe/Cu}$ = 8.9mT. $H_C^{Fe/NiO}$ is more than three times of $H_C^{Fe/Cu}$ though the $H_C^{Fe/Cu}$ has a little different for 24ML Fe film. The coercivity of Fe film grown on antiferromagnetic NiO(001) single crystal is enhanced.

3.6 Reversal processes by in-field SEMPA

Since the MOKE measurement only reveals the effect averaged magnetization, the currently developed technique of in-field SEMPA allows to directly characterize domain structures in presenting of a sufficiently strong magnetic field. In present work the detailed domain behaviors of the magnetization reversal processes are studied. The sample uses Fe film grown on type II NiO(001) single crystal as same as the one used for MOKE measurements. No field cooling procedure was dealt after film deposition. In the following, it consists of two parts to present the Fe domain structures of the reversal processes in the branches with increasing and decreasing field.

3.6.1 Reversal process with decreasing field

Fig.3.13 demonstrates the measurements of in-field SEMPA obtained from a 20ML Fe film epitaxially grown on type II NiO(001) single crystal. Fig.3.13(A) represents the domain structures of as-grown Fe film. As the SEMPA measurements described in previous sections, the images in left and middle columns are the Fe domains in orthogonal asymmetry components A_x and A_y . The axes of A_x and A_y are selected along $[\bar{1}10]$ and $[110]$ directions, respectively. The coordinates are corresponding to the crystalline orientation of NiO(001) single crystal. The dark-white contrast indicates the quantity of asymmetry which has the same grey level as the grey-scale bar shown in right-top corner in Fig.3.13. The domain patterns shown here are quite general as those shown in section 3.4: Straight 90° -type wall which corresponds to T-wall along $[010]$ direction; 180° walls with irregular wall shapes. The T-domains and easy axes of Fe film are sketched in Fig.3.13(D). As described in section 2.2 an static external magnetic field is applied during the process of in-field SEMPA measurement. The magnetic field is generated by a miniature magnet positioned in front of sample surface. The direction of field is applied in surface plane and along the page horizontal indicated at right column of Fig.3.13. At the same imaging area the Fe domains at the applied field $H = 17\text{mT}$ and 37mT are shown in Fig.3.13(B) and (C), respectively. The magnetic images at left and middle columns represents the Fe domains with orthogonal asymmetry components A_x and A_y , respectively. The axes of

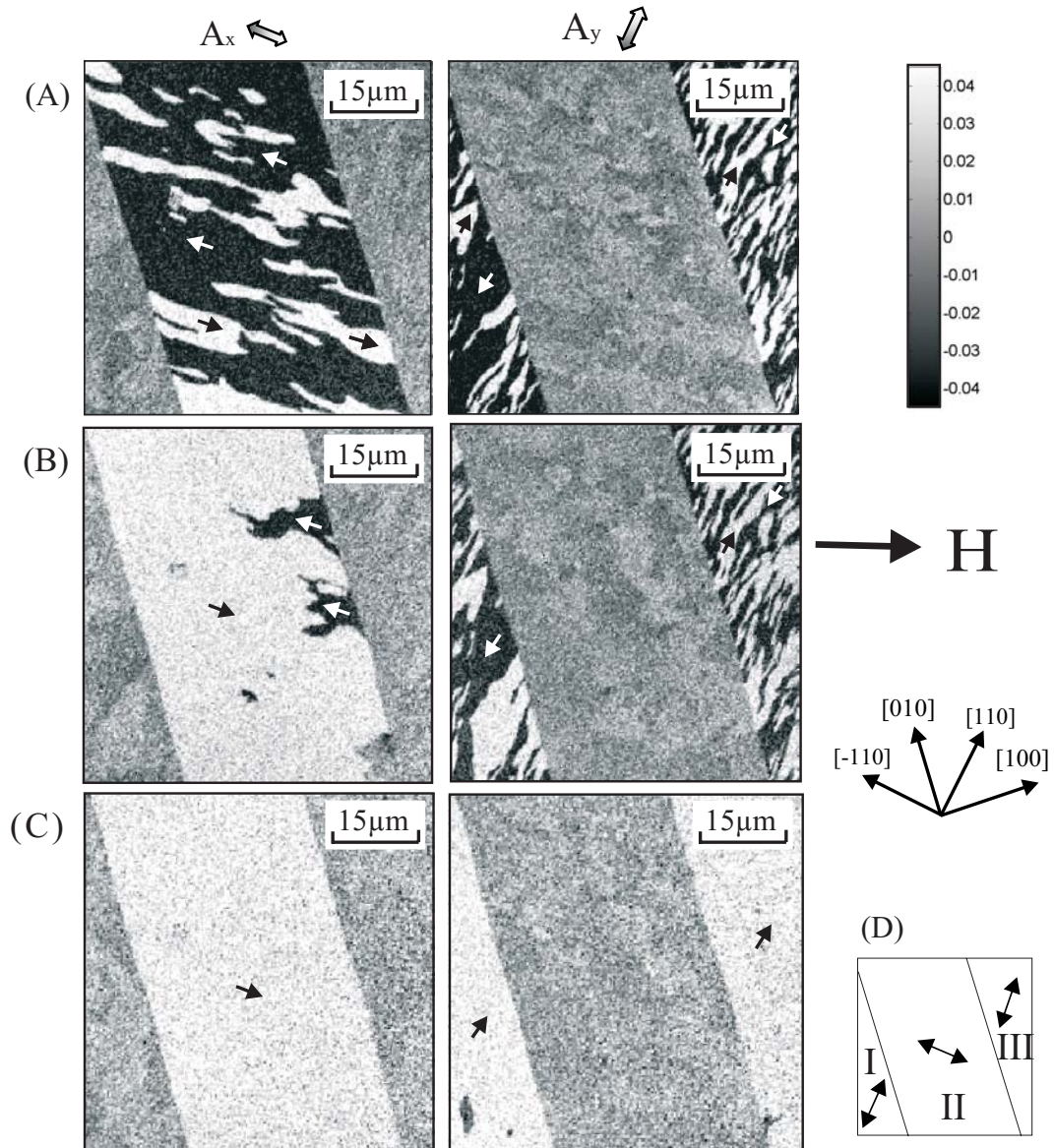


Figure 3.13: Magnetic domain structures of 20ML Fe film grown on type II NiO(001) single crystal by in-field SEMPA. The magnetic field is applied in surface plane. The direction of applied field H is indicated an arrow at right column. (A) as-grown, (B) $H = 17$ mT and (C) $H = 37$ mT. The left and middle columns are Fe domain images in orthogonal asymmetry components A_x and A_y . The axes of A_x and A_y are along $[\bar{1}10]$ and $[110]$ directions, indicated as hollow arrows at the top of (A). (D) A sketch for T-walls and easy axes of Fe film.

A_x and A_y are also along $[\bar{1}10]$ and $[110]$ directions. The dark-white contrast indicates the quantity of asymmetry which has the same grey level as the common grey-scale bar.

With increasing the applied field, the magnetic domains of Fe film on region II start to switch earlier than that on regions I and III, for the easy axis on region II are more close to field direction. At $H = 17\text{mT}$, the Fe domains on region II have merged to merely a single domain indicated as white contrast, while Fe domains on regions I and III have rarely switched, seen in Fig.3.13(B). Continue to increase the applied field, at $H = 37\text{mT}$ a single domain is formed on each region, as shown in Fig.3.13(C). One finds out that the straight 90° -type walls stay at their original positions, which means the T-wall keeps unchanged in this field range. The Fe domains with 180° walls are switched and merged to a single domain. But the magnetic domains of Fe film on region II and I (or III) perform differently for the different orientation of T-domains. The T-walls “isolate” the Fe film on other T-domain. The magnetization reversal of Fe film on narrow region II (or I and III) therefore represents the Fe film on a single T-domain. Owing to the high resolution of in-field SEMPA, it is possible to study the magnetization reversal process of Fe film grown on a single T-domain.

To avoid complicated reversal mechanisms, a convenient scheme is to saturate the Fe film and subsequently to measure the Fe domains by changing the applied field. As is shown in Fig.3.13(C), at the currently maximum field $H = 37\text{mT}$, the Fe film is in a single domain state but it is still not completely saturated. It defines that the positive field is pointing from left to right in horizontal, and negative field from right to left. The magnetic domains of 20ML Fe film on NiO(001) single crystal are measured with the applied field starting from $H = 37\text{mT}$ to -37mT . Some typical domain structures of Fe film are shown in Fig.3.14(A)–(E) with the applied field $H = 0, -23.2, -23.6, -33$ and -37mT . To study the domains of Fe film on region II, the domain images with only one asymmetry A_x are shown. The T-domains and easy axes of Fe film sketched in Fig.3.14(G) are the as-grown domains in Fig.3.13(A). Decreasing the applied field from maximum value 37mT , it keeps a single domain state of Fe film on region II. Fig.3.14(A) shows the Fe domains at remanent state. Nucleations with reversed magnetization (dark-contrast domains) are initiated until the applied field reaches $H = -23.2\text{mT}$ shown in Fig.3.14(B). The size of these nucleations grows in two ways: One is to slightly increase the applied field (for example from -23.2 to -23.6mT); another is to wait for a long time (several hours) by fixing the applied field at $H = -23.2\text{mT}$. Fig.3.14(C) shows the Fe domains by waiting for about 5 hours and fixing the field $H = -23.2\text{mT}$. The Fe domains with white contrast switched to a merely single domain with dark contrast. A few small domains with white contrast are pinned by the T-walls or interface defects in the middle of region II. These small multidomains are hard to be reversed by waiting for a longer time. They may be reversed by continuing to decrease the field, as shown in Fig.3.14(E) and (F). A single domain with dark contrast (opposite magnetization) is formed at $H = -37\text{mT}$, which is illustrated in Fig.3.14(E). From above observation, the magnetization reversal of Fe film on region II is a process with domain nucleation and wall growth.

Near the coercivity the domain nucleation and wall creeping of Fe film grown on

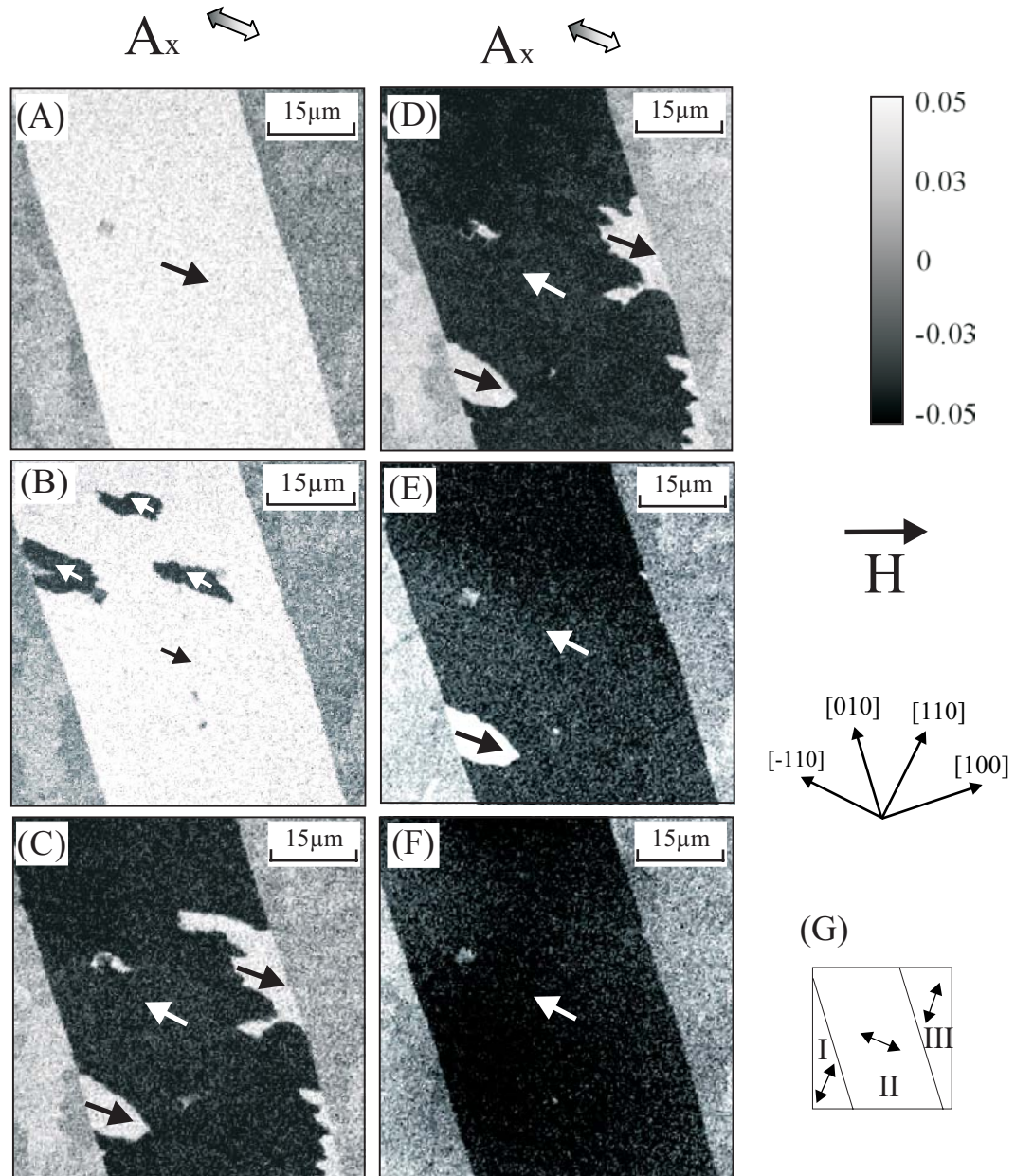


Figure 3.14: The magnetization reversal processes of Fe(20ML)/NiO(001) by in-field SEMPA. The magnetic field is in the sample plane. (A), (B), (C), (D), (E) and (F) are sequences of magnetic images at the field $H = 0, -23.2, -23.2, -23.6, -33$ and -37 mT. Only one asymmetry component is shown. The T-walls and easy axes of as-grown Fe film are sketched in (G). See text for explanation.

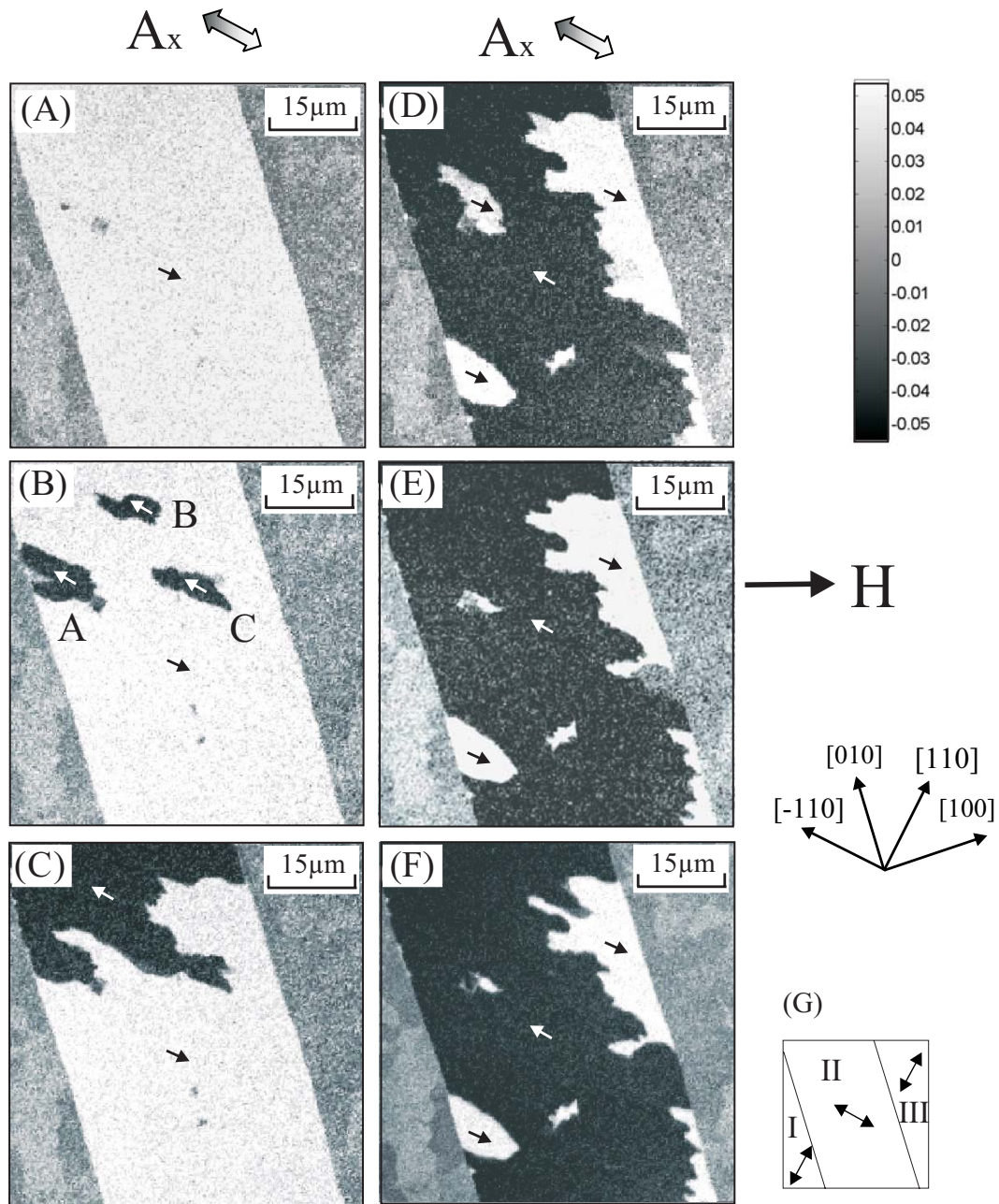


Figure 3.15: *The domain wall creeping of 20ML Fe film on NiO(001). The applied field is fixed at $H = -23.2\text{mT}$. (A) shows the Fe domains image at beginning. (B) after one hour; (C) 2 minutes more; (D), (E) and (F) are sequences of Fe domains in 2 hours. (G) a sketch for T-walls and easy axes of Fe film. See text for explanation.*

region II are observed as is shown in Fig.3.14(B) and (C). To obtain the detailed domain processes, a magnetic field is fixed at $H = -23.2\text{mT}$ during SEMPA measurements. By using scanning mode of SEMPA measurements the domain image can be recorded in speed of one frame per minute. With the time elapse, sequences of Fe domains are obtained at fixed field. They are shown in Fig.4.7. Fig.4.7(A) is a single domain of Fe film on region II at beginning. After about one hour, three nuclei with reversed magnetization (dark contrast) appear at locations A, B and C, seen in Fig.4.7(B). The locations of the nuclei seem random, where nuclei B and C appear in the middle of region II and nucleus A appears at the boundary of a T wall. The front of nuclei with dark contrast extends towards outside slowly which results their size enlargement. This slow wall motion was known as so-called domain wall creeping [108, 109]. In 2 minutes (2 scanning frames) since their appearance, the domain structures are developed from three nuclei shown in Fig.4.7(B) into a large domain shown in Fig.4.7(C). Keeping the magnetic field and waiting longer, the reversed domains may continue to extend to all of the sample by wall creeping, as is shown in Fig.4.7(D), (E) and (F), separately. After several hours, it reaches a state dominated by reversed magnetization as already shown in Fig.3.14(C). The domain wall creeping is very slow. For a simple estimation, the averaged velocity is estimated between $1 \sim 100 \text{ nm/s}$ at room temperature. Because the wall creeping is very sensitive to the magnetic field, a very weak field fluctuation (induced by the current fluctuation) may significantly influence the wall creeping speed. Therefore the precise measurement of the velocity of the wall motion becomes very difficult.

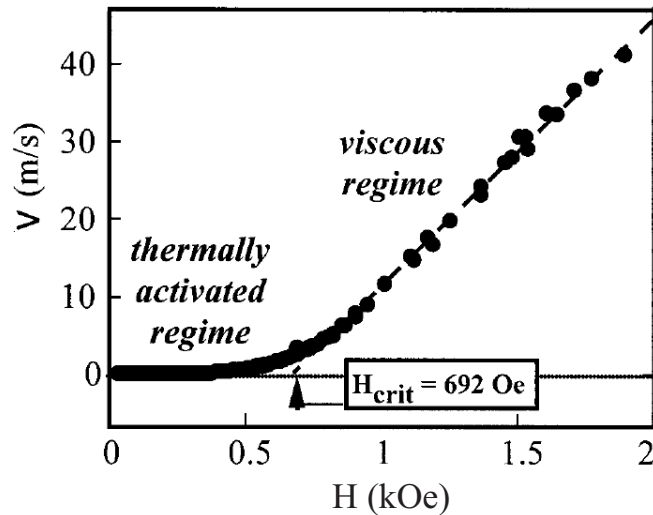


Figure 3.16: Variation of the domain wall velocity with the applied field. From Ref. [109]

The classical creep was known as the thermally activated motion of the vortices of hard type-II superconductors [107]. Feigelman et al. have proposed an exact “creep” theory [107]. Ferré et al. studied the reversal process of Co/Pt film with perpendicular

anisotropy by using Magneto-optical (MO) imaging technique [108, 109]. By using an 1D Ising model, they gave the first experimental proof in magnetism for the universal “creep” theory. Because of uniaxial anisotropy of Fe film grown on a single T domains, it can be treated as 1D Ising system though it has with in-plane magnetization. Then the “creep” theory can be directly extended to the magnetism with uniaxial in-plane anisotropy, i. e. to domain wall motion. Similar to Ferré et al. [108, 109], in the quasi-static limit the domain wall velocity v can be expressed as:

$$v = v_0 \exp\left[-\left(\frac{U_c}{kT}\right)\left(\frac{H_{crit}}{H}\right)^\mu\right] \quad (3.3)$$

T , H and k are temperature, magnetic field and Boltzmann constant, respectively. The activation energy U_c is therefore and experimental accessible quantity [107]. μ is an exponent quantity which equals to $\frac{1}{4}$ in a 1D interface. The critical field H_{crit} corresponds to the applied field at pinning-depinning transition. The relation of creeping velocity to applied field is schematically plotted in Fig.3.16. H_{crit} separates two regions: the low field part which corresponds to a thermally activated regime and the high field part which is related to a viscous regime. In the activated regime, domain walls are pinned by intrinsic defects while, in the viscous regime, the field is large enough to overcome all energy barriers. In our case, the applied field is only about 23.2mT (232Oe) and the velocity of the domain wall motion is very slow. The domain wall creeping for Fe/NiO(001) is located in the region of thermally activated regime.

3.6.2 Reversal process with increasing field

The magnetization processes of Fe film grown on NiO(001) single crystal are characterized by in-field SEMPA at another branch with increasing applied field from $H = -37\text{mT}$ to 37mT . Some typical domain structures of Fe film are presented in this section. Similar to Fig.3.14, Fig.3.17(A)-(F) show Fe domains with the applied field at $H = -22, 19, 23, 23, 25$ and 37mT . With increasing the applied field it is a single domain of Fe film on region II. Until the field reaches at $H = 19\text{mT}$, nuclei with reversed magnetization (white contrast) occur at regions A and B. But these nuclei A and B will not induce the subsequently wall creeping as shown in Fig.4.7. Their domain sizes grow with the field increasing, and also nucleus C may occur, shown in Fig.3.17(C). At this field $H = 23\text{mT}$, the domain wall creeping happens and the magnetization of Fe film on most of region II are reversed to white contrast by slightly increase the applied field, as is shown in Fig.3.17(D). Some “remained domains” (dark contrast) will be reversed by stronger field in Fig.3.17(D), (E) and (F). Finally one notice that domain wall creeping does not occur even with the appearance of nuclei A and B in Fig.3.17(B) until the field reaches near coercivity; the nucleus B remains unchange during the wall creeping process in Fig.3.17(B) and (C). It indicates that the applied field is more important for the wall creeping.

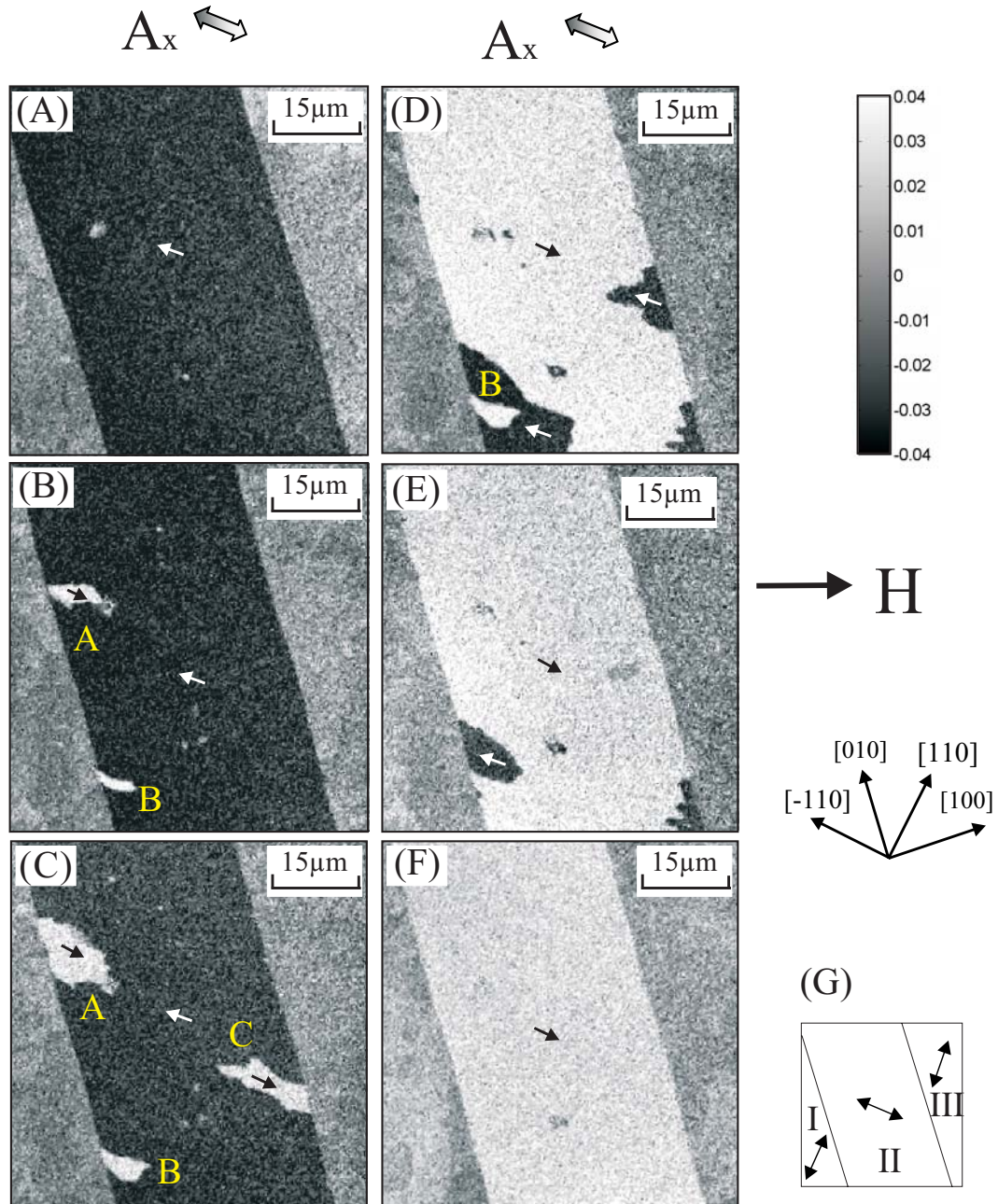


Figure 3.17: *The magnetization reversal processes of Fe(20ML)/NiO(001) by in-field SEMPA. (A), (B), (C), (D), (E) and (F) are sequences of domain images measured at the field $H = -22, 19, 23, 23, 25$ and 37 mT. Only one asymmetry component is shown. The T -walls and easy axes of as-grown Fe film are sketched in (G). See text for explanation.*

In summary, the magnetization reversal process of Fe film epitaxially grown on a single T-domain are studied by in-field SEMPA measurements. The magnetization reversal of Fe film is process of domain nucleation and wall motion. The domain nucleation and wall creeping were only observed in a narrow field range near the coercivity. The Fe domains have no correlation to that of as-grown domains. The reversal processes are quite similar in the branches both with decreasing and increasing fields. No exchange bias was observed.

Chapter 4

Discussions and conclusions

This chapter discusses the experimental results. A phenomenological model is proposed to explain the exchange interaction of Fe films grown on NiO(001) single crystals in section 4.1. In section 4.2, some discussions and comments are made on the magnetization reversal processes of Fe/NiO(001) samples. The conclusions are given at last section 4.3.

4.1 a phenomenological model

Based on the experimental observations, a phenomenological model is proposed to explain the spin structures of Fe films epitaxially grown on NiO(001) single crystals. Before going into the detailed model, it has to mention two recent experiments carried out by Matsuyama et al. [110] and Ohldag et al. [45]. 1). Matsuyama et al. [110] investigated the relationship between the spin polarization of an Fe film and a compensated NiO(001) by using SP-SEM (spin Polarized SEM, another name of SEMPA). They observed that the magnetization of Fe film were in plane and the Fe spin polarization were inclined about 15° (or 14°) from $[\bar{1}10]$ (or $[\bar{1}\bar{1}0]$) to $[\bar{1}00]$ direction. In their model the AFM spins of NiO crystal were rigid and will not be rotated by the exchange interaction; then the Fe spins have to be rotated and follow the AFM spins due to the exchange interaction. They concluded that the Fe spins were near perpendicular coupling to one of Néel axis of bulk NiO. 2). Ohldag et al. [45] investigated the spin structures of Co (and Fe) film epitaxially grown on NiO(001) single crystal by using XPEEM (X-Ray Photoemission Electron Microscopy [111]). They observed bulklike antiferromagnetic domains on cleaved NiO(001) single crystal (without Co coverage). Upon Co deposition the AFM spins of NiO crystal at the interface are reoriented and aligned to be parallel to Co spins. Their observations show collinear exchange coupling between the spins of Co film and NiO(001). Their conclusion was completely contradicted to Matsuyama et al. [110].

Comparing with both experiments, our experimental observations were also carried out

on the Fe/NiO(001) system by using similar imaging techniques. Our experimental results are partially consistent with their observations. The common parts: We have observed that T-walls oriented along [100] (or [010]) direction present a straight 90° -type wall on Fe film, while T-walls oriented along [110] (or $\bar{1}10$) direction absent on Fe domains; The Fe film has a uniaxial anisotropy instead of a four-fold anisotropy. The discrepancy parts: For Fe film grown on type I NiO(001) single crystal, the spins of Fe film are solely aligned along [110] (or $\bar{1}10$) direction due to the exchange interaction at interface, which is a collinear coupling. The case of collinear coupling is consistent with Ohldag et al., but contradicts with Matsuyama et al.. For Fe film grown on type II NiO(001) single crystal, the spins of Fe film are found to be inclined $11 \pm 12^\circ$ from [110] direction and $6 \pm 12^\circ$ from $\bar{1}10$ direction.

We argue that the discrepancy of the Fe spin configuration are caused by the discrepancy of NiO interface property. The inclined angles of Fe films can be explained neither by the collinear coupling [45] nor by the nearly perpendicular coupling [110]. A phenomenological model in general is proposed to explain the exchange interaction of ultrathin Fe (or other ferromagnetic) film epitaxially grown on NiO(001) single crystal.

Since the spins of Fe film and antiferromagnetic spins of bulk NiO(001) single crystal are not parallel, a vertical domain wall would be formed due to the exchange interaction at interface. The vertical domain wall has to be formed in the side of NiO because of ultrathin Fe film whose thickness is not thicker enough to form a Bloch wall (wall width 210nm) [101] in vertical direction. The model is based on two assumptions: 1). It assumes that the spins of Fe film are isotropic in vertical direction. 2). It assumes that the T domains (or equally the ferromagnetic planes) of NiO are identical both in bulk and at interface. In NiO crystal the anisotropy constant of out of FM plane K_1 is two orders larger than that of in-plane anisotropy K_2 [112, 113], so that the AFM spins are more energy favorable to rotate in FM plane than out of FM plane. With these two assumptions the vertical domain wall at interface is therefore formed by the rotation of AFM spins in their FM planes. The lattice mismatch and slightly rhombohedral deformation are ignored.

Similar to the model proposed by Mauri et al. [38], the spin configuration of the vertical domain wall is illustrated in Fig.4.1. In this model it assumes that the NiO(001) single crystal only contains a single T domain. The spins of Fe film S^{Fe} are oriented in (001) plane with an inclined angle from $\bar{1}10$ direction. Only one sublattice of AFM spins (the spins of Ni ions) is shown. The AFM spins S^{NiO} of bulk NiO(001) crystal are oriented parallel to one of Néel axes $\bar{2}11$ (it can be also oriented along other two Néel axes). For the exchange interaction the AFM spins are rotated in ferromagnetic plane (111), which forms a vertical wall at interface. At present configuration S^{NiO} is rotated from its easy axis $\bar{2}11$ towards $\bar{1}10$ direction at interface as shown in Fig.4.1. The S^{NiO} at topmost layer has maximum angle rotating from $\bar{2}11$ Néel axis. It defines that α is the maximum rotation angle from S^{NiO} to $\bar{2}11$ direction in (111) FM plane, and β is the inclined angle from the spin polarization of Fe film S^{Fe} to its easy axis $\bar{1}10$ direction. It also defines γ is the angle between S^{Fe} and nearest S^{NiO} . In present geometry γ is not an independent parameter. It is related to α and β :

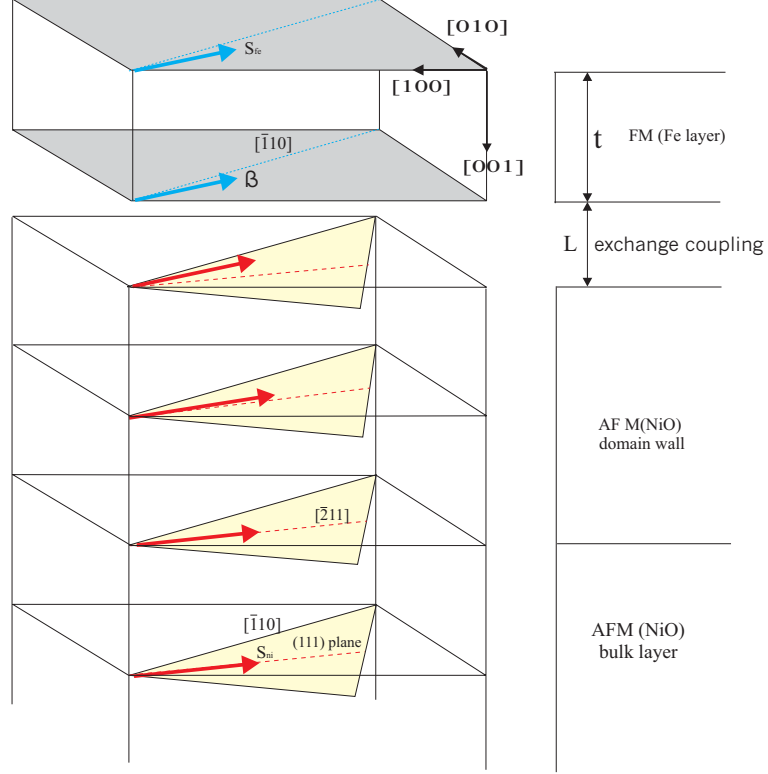


Figure 4.1: A micromagnetic drawing of the exchange coupled Fe/NiO(001) system. AFM spins of only one sublattice are depicted and a single T-domain is assumed. The coordinate corresponds to NiO bulk. The Fe spins are in (001) plane and inclined from [110] direction with an angle β . The AFM spins in bulk NiO crystal are along $[12\bar{1}]$ direction. At a distance L at the interface, an Fe film of thickness t_{Fe} follows NiO layers.

$$\cos\gamma = \sqrt{\frac{2}{3}}[\cos\alpha \cos(45^\circ - \beta) + \sin(\alpha + 30^\circ) \sin(45^\circ - \beta)] \quad (4.1)$$

Ignore the constant items, the total energy per unit area of the interface can be written as [38]:

$$\Delta = 2\sqrt{AK_2}(1 - \cos\alpha) + \frac{A_{12}}{L}(1 - \cos\gamma) + K_{Fe}t\sin^2\beta \quad (4.2)$$

where Δ represents the total energy. L and t denote the exchange distance and the thickness of Fe film. The first term is the energy of the vertical wall extending into the bulk of NiO(001) single crystal according to Zijlstra [114], where A represents the exchange stiffness of bulk NiO(001) crystal. The second term is the exchange energy, where A_{12} represents the exchange stiffness at interface. The third term is the anisotropy

energy of the Fe film. K_{Fe} denotes the anisotropy constant of Fe film (uniaxial anisotropy is assumed here). The total energy in unit of $2\sqrt{AK_2}$ can be derived from equation 4.2:

$$\delta = \frac{\Delta}{2\sqrt{AK_2}} = (1 - \cos\alpha) + \lambda(1 - \cos\gamma) + \mu\sin^2\beta \quad (4.3)$$

where $\lambda = \frac{A_{12}}{2L\sqrt{AK_2}}$, $\mu = \frac{K_{Fe}t}{2\sqrt{AK_2}}$.

In case of $\lambda = 0$, it is the limitation case for bilayer systems without exchange interaction. In following discussion, $\lambda > 0$ and $\mu > 0$.

(1). In case of $\lambda \ll 1$, to minimize the total energy, α has to be very small. The limitation is $\alpha = 0$, which means that S^{NiO} has no spin rotation at the interface. $\delta = \lambda(1 - \cos\gamma) + \mu\sin^2\beta$. In this case the spins of AFM are too ‘‘hard’’ to rotate and no vertical wall is formed at interface.

(2). In case of $\lambda \gg 1$, to minimize the total energy, γ has to be very small. The limitation is $\gamma = 0$, which means that Fe spins have no inclined angle. $\delta = (1 - \cos\alpha) + \mu\sin^2\beta$. In this case S^{Fe} and S^{NiO} are parallel (or anti-parallel) at interface, which is collinear coupling as in section 3.3 and Ref. [45].

(3). In case of medium λ , α and γ are not zero, both of them are depending on the parameters λ and μ .

From above discussions, γ is an important criterion to describe the spin configuration of exchange coupled Fe/NiO(001) system. The magnitude of γ depends on the experimental measurements of A_{12} , A and K_2 . In a simple estimation it uses $K_2 = 1.5 \times 10^{-4} J/m^3$ [112], $A = 3 \times 10^{-11} J/m$ [110], $K_{Fe} = 4.72 \times 10^{-4} J/m^3$ [115], Fe film thickness $t = 3$ nm. It assumes that $L = 0.287$ nm (the same as the lattice constant of cubic Fe crystal). Since the exchange stiffness at interface A_{12} is unknown, it assumes $A_{12} = A$. One obtains $\lambda = 0.78 \times 10^2$ and $\mu = 0.0105 \ll 1$. The third item of $\mu\sin^2\beta$ in equation 4.3 is a second order term and can be ignored. Then the equation 4.3 can be written:

$$\delta = (1 - \cos\alpha) + \lambda(1 - \cos\gamma) \quad (4.4)$$

The parameter γ has the medium value. In the numerical calculation λ is varied from 0.01 to 100 because of the unknown A_{12} . For a given λ and β , the angles of α and γ can be calculated by using equation 4.1 and minimizing the total energy shown in equation 4.4.

Fig.4.2 shows the numerical calculations. The angle α and γ are plotted as a function of λ at $\beta = 1^\circ, 6^\circ, 11^\circ, 15^\circ, 20^\circ, 30^\circ$ and 44° . The magnitude of inclined angle β can be measured by experimental. For a given β , with increasing λ the AFM spins have larger rotation angle α at interface, and they are more close to Fe spins (smaller γ). The following part it only discusses the case at the calculated $\lambda = 78$ indicated as a vertical solid line in Fig.4.2. In case of $\beta = 1^\circ$, then one obtains $\alpha = 29^\circ$ and $\gamma = 1^\circ$. In this case S^{NiO} and S^{Fe} are collinear coupled, and they are oriented along [110] (or $[\bar{1}10]$) direction at interface, as described in section 3.3 and in Ref. [45]. When $\beta = 6^\circ, 11^\circ$ and 15° as shown previously in Fig.4.6 and by Matsuyama et al. [110], then one has $\alpha = 26^\circ, 23^\circ$

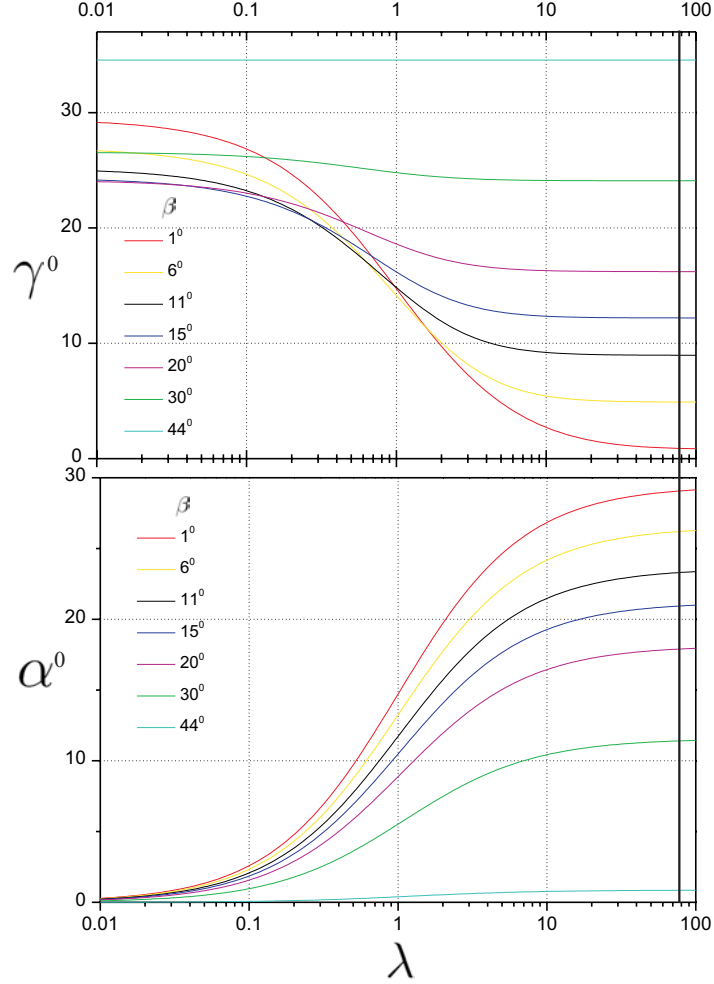


Figure 4.2: The numerical calculation with λ from 0.01 to 100. The angles α and γ plotted as a function of λ at $\beta = 1^\circ, 6^\circ, 11^\circ, 15^\circ, 20^\circ, 30^\circ$ and 44° .

and 21° , and $\gamma = 4.9^\circ, 9^\circ$ and 12° , respectively. S^{NiO} is corresponding to rotate $26^\circ, 23^\circ$ and 21° from $[\bar{2}11]$. In these cases S^{Fe} and S^{NiO} are not parallel at interface, which are the nearly collinear coupling. And when $\beta = 44^\circ$, $\alpha = 0^\circ$ and $\gamma = 34^\circ$. There is no spin rotation of S^{NiO} at interface for variety λ . Finally one notice that β is different for Fe film grown on adjacent T-domains which is still an open question. A possible reason might be the strain. The different strain might influence the A_{12} , which gives different λ .

In general the phenomenological model described here would be also possible to explain the exchange interaction of other FM films (Co, Ni and Py) grown on NiO(001) single crystal. Since the parameter of exchange stiffness at interface A_{12} is strongly correlated to the the interface conditions, the application of the model will also depend on the

knowledge of the interface.

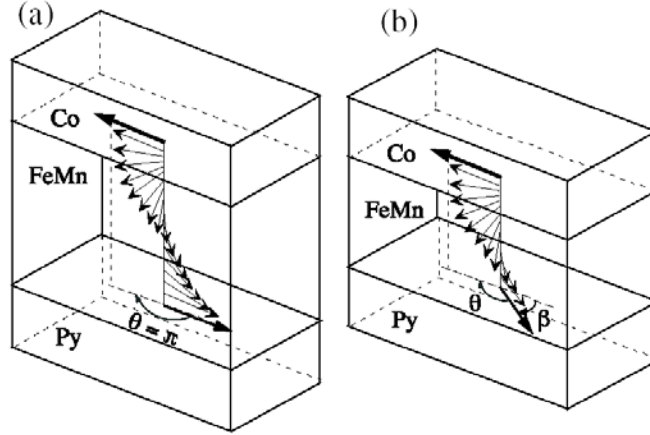


Figure 4.3: Schematic diagram of the spin structures in Py/FeMn/Co trilayers (a) for FeMn thickness $t_{AFM} > 90\text{\AA}$ with $\theta = \pi$ between the magnetization of Co and Py, and (b) for $t_{AFM} < 90\text{\AA}$ with $\theta < \pi$. For clarify, only one AFM sublattice of FeMn is depicted. From Ref. [44].

Many realistic theoretical investigations have concluded a dynamic AF spin structure [38, 42, 43, 116]. A recent experiment demonstrated spiraling spin structure of antiferromagnetic wall in an exchange coupled FM/AFM bilayers [44], as shown in Fig.4.3. They investigated the hysteresis loop of trilayers of Permalloy/FeMn/Co system with varied thicknesses t_{AFM} of the AFM FeMn layer. They found out that when $t_{AFM} < 90\text{\AA}$, they estimated the turn angle θ of the spiral FeMn spins varying as $\theta = (1.76^\circ/\text{\AA}) \times t_{AFM}$; when $t_{AFM} > 90\text{\AA}$, the turn angle remains constant. They concluded that the exchange interaction of Py/FeMn/Co system was an interface effect and had spiraling spin structure with FeMn.

4.2 Discussion on magnetization reversal process

The enhanced coercivity is observed in almost all of exchange coupled FM/AFM systems. Though the exchange bias and enhanced coercivity are two associated phenomena for the exchange coupled FM/AFM systems, the mechanism of enhanced coercivity is seldom studied systematically. It can not be quantitatively derived from the simplest model of coherent rotation magnetization [1]. In this case the exchange anisotropy only leads to a shift of hysteresis loop along the field axis, while the coercivity of the FM/AFM bilayers remains equal to the coercivity of “free” FM film. In fact, it has been pointed out that the single-domain character of a magnet is largely irrelevant to the problem of

coercivity in general [117]. A random field model was recently proposed to explain the exchange interaction of FM/AFM bilayer [118]. In this model, the enhanced coercivity was determined as a function of the thickness of the ferromagnetic layer, the grain size, and the interface random field. Their theory is consistent with recent experiments [119]. On perfectly flat interfaces, it is shown that spin-flop coupling does not lead to exchange bias, but rather gives rise to a uniaxial anisotropy which in turn causes the large coercivity observed in exchange biased bilayer [120, 121].

In the development of a comprehensive theory of exchange anisotropy, it is important to experimentally understand the microscopic details of magnetization reversal [118, 122]. As described in section 3.5 and 3.6 the magnetization reversal processes of Fe film grown on NiO(001) single crystal are investigated by MOKE and in-field SEMPA. The coercivity is found to be enhanced, but no exchange bias is observed. It seems that the mechanism of enhanced coercivity and exchange bias are different. During the magnetization reversal it is merely a single domain state. The domain nucleation and wall creeping are only observed in a narrow field rang near coercivity. The wall creeping is considered as a thermally activated regime.

Many other magnetic imaging techniques have recently performed to study the microscopic details of the magnetization reversal processes of FM/AFM systems: such as Magnetic force Microscopy (MFM) [49, 123], Magneto-optic Kerr Microscopy [124], magneto-optical indicator film (MOIF) technique [125, 126] and high resolution interference-contrast-colloid (ICC) [122, 127]. The magnetization reversal of epitaxial NiO/NiFe bilayers grown on MgO(001) was studied by Nikitenko et al. using MOIF [125]. They concluded that the unidirectional-axis magnetization reversal proceeded by domain nucleation and growth; the nucleation centers appeared asymmetry, which were governed by defect structures in the AFM layer [125]. The experiments, by using Magneto-optic Kerr effect microscopy [124] and ICC technique [122], also show the magnetization process of nucleation and domain wall growth because of exchange coupling of the NiFe/NiO and Co/NiO bilayers, respectively. The magnetization measurements by using these techniques are somehow indirect which causes complex to understand the experimental details. SP-SEM with the help of pulsed magnetic field by Iwasaki et al. [128] measured the domain configuration of NiFe/NiO(111) single crystal. As a standard SEMPA they can only characterize the domain structures at remanent state instead of in external field.

We use the proposed phenomenological model which described in previous section to explain the enhanced coercivity of Fe/NiO(001) system. Since all of these experiments reveal that the magnetization reversal of FM/AFM system is a process with domain nucleation and wall motion of FM film, the spin variations along the interface should be considered. Due to the force of exchange coupling, a vertical wall is formed by rotating AFM spins at interface. During the magnetization reversal process the spins of Fe film are now nonuniform, and the SFM spin configuration of vertical wall is realigned. The total energy of the interface has to take account into this energy modification, which is simply an extension of equation 4.2:

$$\begin{aligned} \Delta = & 2\sqrt{AK_2}(1 - \cos\alpha) + \frac{A_{12}}{L}(1 - \cos\gamma) + K_{Fe}t\sin^2\beta \\ & + HM_S t(1 - \sin\beta) + A_{Fe}t\left(\frac{d\beta}{dx}\right)^2 + A\xi\left(\sqrt{\frac{3}{2}}\frac{d\alpha}{dx}\right)^2 + K_2\xi\sin^2\alpha \end{aligned} \quad (4.5)$$

H, A_{Fe} , and M_S are the applied field along $[\bar{1}10]$ direction, the exchange constant, and saturation magnetization Fe film, respectively. $\xi = \sqrt{\frac{A}{K_2}}$ is related to the vertical wall thickness in NiO crystal. The first three items has been explained in equation 4.2. Item $HM_S t(1 - \sin\beta)$ is Zeeman energy. Items $A_{Fe}t\left(\frac{d\beta}{dx}\right)^2$ and $A\xi\left(\sqrt{\frac{3}{2}}\frac{d\alpha}{dx}\right)^2$ represent the exchange energy caused by the nonuniform spins of Fe film and NiO crystal, respectively. x is in surface plane which assumes along $[\bar{1}10]$ direction. The last item $K_2\xi\sin^2\alpha$ is the anisotropy energy of NiO crystal at interface.

According to the treatment of Nikitenko et al. [129] and Khapikov [130], for the free FM film its coercivity is:

$$H_C^{FM} = \frac{2K_{FM}}{M_S} - \frac{M_S^3 t^2}{8A_{FM}} \quad (4.6)$$

For our special system of Fe film grown on NiO(001) single crystal, it has [129]:

$$H_C^- = -\frac{2K_{Fe}}{M_S} - \eta \cdot \frac{2K_2}{M_S} \frac{2\xi}{t} - \frac{M_S^3 t^3}{8(A_{Fe}t + A\xi)} \quad (4.7)$$

$$H_C^+ = \frac{2K_{Fe}}{M_S} + (1 - \eta) \cdot \frac{2K_2}{M_S} \frac{2\xi}{t} + \frac{M_S^3 t^3}{8(A_{Fe}t + A\xi)} \quad (4.8)$$

Where H_C^+ and H_C^- are the coercivities at the magnetic field orientations parallel and antiparallel to the applied field, respectively. η is between 0 to 1. Then the coercivity and exchange bias are:

$$H_E = \frac{H_C^+ + H_C^-}{2} = (1 - 2\eta) \frac{2K_2 \xi}{M_S t} \quad (4.9)$$

$$H_C = \frac{H_C^+ - H_C^-}{2} = \frac{2K_{Fe}}{M_S} + \frac{2K_2 \xi}{M_S t} - \frac{M_S^3 t^3}{8(A_{Fe}t + A\xi)} \quad (4.10)$$

In this treatment it assumes that the vertical AFM wall has a planar distribution in interface plane. In case of a completely uncompensated interface $\eta = 0$, and the case of a completely compensated interface $\eta = 0.5$. The interface conditions are strongly depending on the procedure of sample preparation, field cooling and deposition in the field. The compensated interface is assumed in our Fe/NiO(001), and then no exchange bias is expected.

From the expressions 4.6 and 4.10, it shows that the coercivity of Fe/NiO(001) system is enhanced. This enhancement is related to the properties of the dynamic AFM wall. The Fe spins are pinned by AFM spins by the force of exchange coupling. The coercivity is a critical field to reverse the Fe magnetization. When the applied field is reversed, the twisted vertical wall in NiO crystal stores energy which is attributes to the increasing of

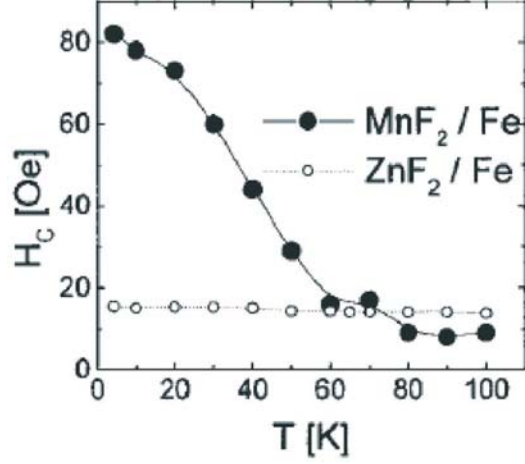


Figure 4.4: H_C as a function of T for cooling field $H_{FC}=2kOe$. The solid symbols are for Fe/MnF_2 (AFM, $T_N=67K$), and open symbols are for Fe/ZnF_2 (nonmagnetic). The lines are guides to the eye. From Ref. [132].

the critical field. At near coercivity the Zeeman energy is not strong enough to reverse the Fe magnetization. The nuclei with reversed Fe spins are generated by the magnetostatic field at the boundaries of crystal defect or T-wall. With the help of thermal activity, the spins on near region are then reversed by wall creeping. These phenomena of nucleation and domain wall creeping are observed and shown in section 3.6. Apart from the field strength, the temperature plays a role at this reversal process. In some experiments the coercivity H_C as a function of temperature was recently performed on exchanged coupled MnF_2/Fe system [17, 119, 131, 132], shown in Fig.4.4. With increasing the temperature H_C of MnF_2/Fe system decreases and becomes constant above T_N . For comparison when Fe film was grown on nonmagnetic substrate of ZnF_2 , the coercivity remains constant at variety temperature.

4.3 Conclusions

This thesis is devoted to the investigation of exchange interaction of ferromagnetic (FM) material contacting with antiferromagnetic (AFM) material. At present works the system of ultrathin Fe films epitaxially grown on NiO(001) single crystals are used for this investigation. The spin polarization of as-grown Fe/NiO(001) are characterized by Scanning Electron Microscopy with Polarization Analysis (SEMPA), and T-walls of NiO(001) single crystal by optical observations. The magnetization reversal processes of Fe film grown on NiO(001) are studied by Magneto-optical Kerr Effect (MOKE). And the detailed domain behaviors in magnetization reversal processes are characterized by in-field SEMPA. The main conclusions are described in the following:

1). The spin polarizations of Fe film are strongly correlated to the spins of underlying NiO(001) single crystal due to the exchange interaction at interface. With the thickness up to 30ML, the Fe spins are in plane and the Fe film reveals uniaxial anisotropy. The axis of uniaxial anisotropy rotates nearly 90° when the Fe film grown on NiO(001) with T-domains with wall oriented along [100] (or [010]) direction. It is also observed that the directions of Fe spins in each domain are correlated to the preparations of NiO(001) single crystals. The Fe spins are solely aligned along [110] (or $\bar{1}10$) direction when Fe film is epitaxially grown on type I NiO(001) single crystal. They are inclined $6^\circ \pm 12^\circ$ from $\bar{1}10$ direction or inclined $11^\circ \pm 12^\circ$ from [110] direction when Fe film is epitaxially grown on type II NiO(001) single crystal. Very similar spin structures are observed for Permalloy (Fe at 20% and Ni at 80%) grown on a same NiO(001) single crystal. In conclusions, the spin structures of Fe (and Permalloy) films are correlated to the exchange interaction rather than structural effects.

2). A phenomenological model is proposed to explain the exchange interaction of ultrathin Fe film grown on NiO(001) single crystal. The model reveals a vertical domain wall formed in NiO crystal at interface. The T-domain (or equally FM plane) of NiO(001) are assumed to be not changed both at interface and in bulk. Since K_1 (out of plane anisotropy) is about two orders larger than K_2 (in-plane anisotropy), the spins of NiO are energy favorably to rotate in their FM planes. For various NiO crystal preparations the surface exchange stiffness was assumed to be different. It uses a parameter λ (proportional to the exchange stiffness at interface) to describe discrepancy of crystal interface. 1. For $\lambda \gg 1$, the spins of both Fe film and NiO are parallel and along [110] (or $\bar{1}10$) direction at interface, which is a type of collinear coupling. It explains the observation of Fe film grown on type I NiO(001) single crystal. 2. For $\lambda \ll 1$, the exchange interaction at interface is too weak to form any vertical wall in NiO crystal. 3. For medium λ , a vertical domain wall can be formed at the interface, but the exchange interaction is not strong enough to align the spins of Fe and NiO to be parallel. In the results the Fe spins are never aligned along [110] (or $\bar{1}10$) direction while they are inclined from [110] (or $\bar{1}10$) direction. The Fe film grown on type II NiO(001) single crystal belongs to this case.

3). The magnetization reversal processes of Fe film grown on NiO(001) single crystal

are investigated. MOKE measurements show that Fe film has uniaxial anisotropy. The shape of hysteresis loop is quite symmetric in field axis which reveals symmetric reversal process. No exchange bias is observed in MOKE measurements. The coercivity of Fe film on NiO(001) single crystal, which is more than three times of “free” Fe film, is enhanced. The enhancement is explained by the generation of a twist wall in AFM NiO crystal at interface. The detailed domain behaviors are characterized by in-field SEMPA. Direct experimental observations show that the demagnetization of Fe film proceeds with domain nucleation and wall growth. Nuclei with reversed magnetization initiate at the boundary of the defects or T-walls. The Fe domains with reversed magnetization grow by wall creeping with the help of thermally activity. The wall creeping is only happened when the magnetic field is applied very close to coercivity. This creeping process completed in a very narrow field range. The reversal processes are quite symmetric in the branches both with decreasing and increasing applied fields, and no exchange bias is observed in the reversal process.

Finally it is worth to mention the experimental aspects. The characterization of magnetization reversal processes is owing to the setups of MOKE and in-field SEMPA. It is the first time to apply SEMPA on the magnetization reversal process of ultrathin Fe/NiO(001).

Bibliography

- [1] W. H. Meiklejohn, C. P. Bean, Phys. Rev. **102**, 1413 (1956).
- [2] W. H. Meiklejohn, C. P. Bean, Phys. Rev. **105**, 904 (1957).
- [3] C. P. Bean, in *Structure and Properties of Thin Films*, edited by C. Neugebauer, J. Newkirk, and D. Vermilyea (Wiley, New York, 1959), P. 331.
- [4] See J. S. Kouvel, J. Phys. Chem. Solids **21**, 57 (1961), and related works.
- [5] J. Nogués, Ivan K. Schuller, J. Magn. Magn. Mater. **192**, 203 (1999).
- [6] P. J. Van der Zaag, R. M. Wolf, A. R. Ball, C. Bordel, L. F. Feiner, R. Jungblut, J. Magn. Magn. Mater. **148**, 346 (1995)
- [7] W. C. Cain, M. H. Kryder, J. Appl. Phys. **67**, 5722 (1990).
- [8] Review - Applications - GMR: J. C. S. Kools, IEEE Trans. Magn. **32**, 3165 (1996)
- [9] Review - Applications: C. Tang, J. Appl. Phys. **55**, 2226 (1984).
- [10] A. E. Berkowitz, Kentaro Takano, J. Magn. Magn. Mater. **200**, 552 (1999).
- [11] J. Nogués, T. J. Moran, D. Lederman, Ivan K. Schuller, K. V. Rao, Phys. Rev. B **59**, 6984 (1999).
- [12] J. Nogués, D. Lederman, T. J. Moran, and Ivan K. Schuller, Phys. Rev. Lett. **76**, 4624 (1996).
- [13] C. Leighton, J. Nogués, Harry Suhl, and Ivan K. Schuller, Phys. Rev. B **60**, 12837 (1999).
- [14] K. Zhang, T. Zhao, and H. Fujiwara, J. Appl. Phys. **89**, 6910 (2001).
- [15] V. I. Nikitenko, V. S. Gornakov, A. J. Shapiro, R. D. Schull, Kai Liu, S. M. Zhou, and C. L. Chien, Phys. Rev. Lett. **84**, 765 (2000).
- [16] M. R. Fitzsimmons, P. Yashar, C. Leighton, Ivan K. Schuller, J. Nogués, C. F. Majkrzak, and J. A. Dura, Phys. Rev. Lett. **84**, 3986(2000).
- [17] N. J. Gökemeijer, and C. L. Chien, J. Appl. Phys. **85**, 5516 (1999).
- [18] Y. I. Jiri, J. A. Borchers, R. W. Erwin, S. H. Lee, P. J. Van der Zaag, and R. M. Wolf, Phys. Rev. Lett. **80**, 608 (1998).
- [19] T. J. Moran, J. Nogués, D. Lederman, and Ivan K. Schuller, Appl. Phys. Lett. **72**, 617 (1998).

- [20] R. D. Hempstead, S. Krongelb, and D. A. Thompson, *IEEE Trans. Magn.* **MAG-14**, 521 (1978).
- [21] B. Dieny, V. Speriosu, S. S. P. Parkin, B. A. Gurney, D. R. Wilhoit, and D. Mauri, *Phys. Rev. B* **43**, 1297 (1991).
- [22] B. Dieny, A. Granovsky, A. Vedyayev, N. Ryuhanova, C. Comache, and L. C. pereira, *J. Magn. Magn. Mater.* **151**, 387 (1995).
- [23] S. S. Parkin, K. P. Roche, M. G. Samant, P. M. Rice, R. B. Berers, R. E. Scheuerlein, E. J. O'Sullivan, S. L. Brown, J. Bucchigano, D. W. Abraham, Y. Lu, M. Rppls, P. L. Trouilloud, R. A. Wanner and W. J. Gallagher, *J. Appl. Phys.* **85**, 5828 (1999).
- [24] H. Ohno, *Science*. **281**, 951 (1998).
- [25] G. Prinz, *Science*. **282**, 1660 (1998).
- [26] V. S. Speriosu, B. Dieny, P. Humbert, B. A. Gurney, and H. Lefakis, *Phys. Rev. B* **44**, 5358 (1991).
- [27] D. Dieny, *J. Magn. Magn. Mater* **136**, 335 (1994).
- [28] C. Meny, J. P. Jay, P. Panissod, P. Humbert, V. S. Speriosu, H. Lefakis, J. P. Nozieres, and B. A. Gurney, in *Magnetic Ultrathin Films: Multilayers and Surfaces/Interfaces and Characterization*, edited by B. T. Jonker et al., MRS Symposia Proceedings No. 313, Materials Research Society, Pittsburgh, (1993), Vol. 313, pp. 289.
- [29] J. S. Moodera, L. R. Kinder, T. M. Wong, and R. Meservey, *Phys. Rev. Lett.* **74**, 3273 (1995), and references therein.
- [30] J. S. Moodera, L. R. Kinder, T. M. Wong, and R. Meservey, *J. Appl. Phys.* **79**, 4724 (1996), and references therein.
- [31] L. M. Falicov, *Phys. Today*. **45(10)**, 46 (1992).
- [32] J. Daughton, *J. Appl. Phys.* **81**, 3758 (1997).
- [33] J. B. Kortright, D. D. Awschalom, J. Stöhr, S. D. Bader, Y. U. Idzerda, S. S. P. Parkin, Ivan K. Schuller, H. -C. Siegmann, *J. Magn. Magn. Mater* **207**, 7 (1999).
- [34] M. N. Baibich, J. M. Broto, A. Fert, F. Nguyen Van Dau, and F. Petroff P. Eitenne, G. Creuzet, A. Friederich, and J. Chazelas, *Phys. Rev. Lett.* **61**, 2472 (1988).
- [35] C. Tsang, and K. Lee, *J. Appl. Phys.* **53**, 2605 (1982).
- [36] G. Binasch, P. Grünberg, F. Saurenbach, and W. Zinn, *Phys. Rev. B* **39**, 4828 (1989).
- [37] W. H. Meiklejohn, *J. Appl. Phys.* **33**, 1328 (1962).
- [38] D. Mauri, H. C. Siegmann, P. S. Bagus, E. Kay, *J. Appl. Phys.* **62**, 3047 (1987).
- [39] A. P. Malozemoff, *J. Appl. Phys.* **63**, 3874 (1988).
- [40] A. P. Malozemoff, *Phys. Rev. B* **37**, 7673 (1988).
- [41] A. P. Malozemoff, *Phys. Rev. B* **35**, 3679 (1987).

- [42] N. C. Koon, Phys. Rev. Lett. **78**, 4865 (1997).
- [43] T. C. Schulthess, W. H. Butler, Phys. Rev. Lett. **81**, 4516 (2000).
- [44] E. Y. Yand and C. L. Chien, Phys. Rev. Lett. **85**, 2597 (2000).
- [45] H. Ohldag, A. Scholl, F. Nolting, S. Anders, F. U. Hillebrecht, and J. Stöhr, Phys. Rev. Lett. **86**, 2878(2001).
- [46] W. J. Antel, Jr., F. Perjeru, and G. R. Harp. Phys. Rev. Lett. **83**, 1439(1999).
- [47] Kentaro Takano, R. H. Kodama, A. E. Berkowitz, W. Cao, G.Thomas, Phys. Rev. Lett. **79**, 1130 (1997).
- [48] Kentaro Takano, R. H. Kodama, A. E. Berkowitz, W. Cao, G.Thomas, J. Appl. Phys., **83**, 6888 (1998).
- [49] M. Cartier, S. Auffret, Y. Samson, P. Bayle-Guillemaud, B. Dieny, J. Magn. Magn. Mater. **223**, 63 (2001).
- [50] W. L. Roth, J. Appl. Phys. **31**, 2000(1960).
- [51] S. Saito, M. Miura, K. Kurosawa, J. Phys. C: Solid State Phys. **13**, 1513 (1980).
- [52] Glen A. Slack, J. Appl. Phys. **31**, 1571 (1960).
- [53] W. Roth, Phys. Rev. **111**, 772 (1958).
- [54] W. L. Roth, G. A. Slack, J. Appl. Phys. Suppl. **31**, 352S(1960).
- [55] S. Greenwald and J. S. Smart, Nature, **166**, 523 (1950).
- [56] J. Kanamori, Progr. Theoret. Phys. (Japan) **17**, 197 (1957).
- [57] W. L. Roth, Phys. Rev. **111**, 772 (1958).
- [58] C. G. Shull, W. A. Strauser, and E. O. Wollan, Phys. Rev. **83**, 333 (1951).
- [59] C. Shull, W. Strausser, and E. Wollan, Phys. Rev. **83**, 333 (1951).
- [60] J. F. Bobo, S. Dubourg, E. Snoeck, B. Warot, P. Baules, J. C. Ousset J. Magn. Magn. Mater. **206**, 118-126 (1999).
- [61] T. H. DiStefano, IBM Tech. Disclosure Bull. **20**, 4212(1978).
- [62] R. Allenspach, IBM J. Res. Develop. **44**, 553(2000).
- [63] K. Koike, K. Hayakawa, Jpn. J. Appl. Phys. **23**, L187(1984).
- [64] J. Unguris, G. Hembree, R. J. Cellota, and D. T. Pierce, J. Microsc. **139**, RP1(1985).
- [65] K. Koike, H. Matsuyama, and K. Hayakawa, Scan. Microsc. **1**, 241(1987).
- [66] M. R. Scheinfein, J. Unguris, M. H. Kelley, D. T. Pierce, R. J. Celotta, Rev. Sci. Instrum. **61**, 2501(1990).

- [67] G. G. Hembree, J. Unguris, R. J. Celotta, and D. T. Pierce, *scan. Microsc* **1**, 229(1987).
 - [68] H. P. Oepen, J. Kirschner, *Scanning Microscopy* **5**, 1(1991).
 - [69] J. Unguris, D. T. Pierce, A. Galejs, R. J. Celotta, *Phys. Rev. Lett.* **49**, 72(1982).
 - [70] G. Chobrok, M. Hofmann, *Phys. Lett.* **57A**, 257(1976).
 - [71] J. Kirschner, K. Koike, H. P. Oepen, *Phys. Rev. Lett.* **59**, 2099(1988).
 - [72] E. Kisker, W. Gudat, K. Schröder, *Solid State Commun.* **44**, 591(1982).
 - [73] J. Kirschner, *Polarized Electrons at Surfaces*, Springer, Berlin, 1985.
 - [74] J. Kessler, *Polarized Electrons*, Springer, Berlin, 1985.
 - [75] M. R. Scheinfein, J. Unguris, M. H. Kelley, D. T. Pierce, and R. J. Cellota, *Rev. Sci. Instrum.* **61**, 2501(1990).
 - [76] A. Gavrin, J. Unguris, *J. Magn. Magn. Magn.* **213**, 95(2000).
 - [77] G. Steierl, G. Liu, D. Iogov and J. Kirschner, **73**, 4264 (2002) *Rev. Sci. Instrum.*.
 - [78] The magnetic foil is commercially available from Magntic Shield Corporation (Bensenville, IL, USA) under the trademark CO-NETIC AA.
 - [79] J. Kessler, *Polarized Electrons*, 2nd edition, Springer, Berlin, 1983.
 - [80] The program SIMIOM 3D 6.0 available from Princeton Electronic Systems, Inc. was used for field calculation and ray tracing simulation.
 - [81] R. Hertel and H. Kronmüller, *Physica B.* **275**, 1(2000).
 - [82] J. Baruchel, *Physica (Amsterdam)* **192B**, 79 (1993).
 - [83] T. Yamada, S. Saito, and Y. Shimomura, *J. Phys. Soc. Jpn.* **21**, 672 (1966).
 - [84] B. K. Tanner, M. Safa, D. Midgley, and J. Bordas, *J. Magn. Magn. Mater.* **1**, 337 (1976).
 - [85] H. Kondoh and T. Takeda, *J. Phys. Soc. Jpn* **19**, 2041 (1964).
 - [86] M. Fiebig, D. Frölich, S. Leute, and R. V. Pisarev, *Appl. Phys. B* **66**, 265 (1998).
 - [87] S. Anders, H. A. Padmore, R. M. Duarte, T. Renner, T. Stammner, A. Scholl, M. R. Scheinfein, J. Stöhr, L. Séve, and B. Sinkovic, *Rev. Sci. Instrum.* **70**, 3973 (1999).
 - [88] W. L. Roth, *Fourth International Congress, Internationa Union of Crystallography, Montreal, Canada, paper 15.6 (1957)*.
 - [89] Handbook of Auger Electron Spectroscopy, second edition, published by Physical Electrons Industries, Inc. 1976.
- Images of Antiferromagnetic Structure of a NiO(100) Surface by Means of X-Ray Magnetic Linear Dichroism Spectromicroscopy*

- [90] Soshin Chikazumi, *Physics of Ferromagnetism* second edition, P417, Clarendon Press, Oxford, 1997.
- [91] J. L. Robins, R. J. Celotta, J. Unguris, D. T. Pierce, B. T. Jonker, G. A. Prinz, Appl. Phys. Lett. **52**, 1918 (1988).
- [92] H. P. Oepen, J. Magn. Magn. Mater. **93**, 116 (1991).
- [93] H. Pinkvos, H. Poppa, E. Bauer, and J. Hurst, Ultramicroscopy **47**, 339 (1992).
- [94] R. Allenspach and A. Bischof, Phys. Rev. Lett. **69**, 3385 (1992).
- [95] N. D. Mermin and H. Wagner, Phys. Rev. Lett. **17**, 1133 (1966).
- [96] J. G. Gay and R. Richter, Phys. Rev. Lett. **56**, 2778 (1986).
- [97] D. P. Pappas, K.-P. Kämper, and H. Hopster, Phys. Rev. Lett. **64**, 3179 (1990); D. P. Pappas et al., J. Appl. Phys. **69**, 5209 (1991).
- [98] D. Pescia et al., Phys. Rev. Lett. **58**, 2126 (1987).
- [99] C. Liu, E. R. Moog, and S. D. Bader, J. Appl. Phys. **64**, 5325 (1988).
- [100] G. Lugert et al., Mater. Res. Soc. Symp. Proc. **232**, 97 (1992).
- [101] H. P. Oepen, and J. Kirschner, Phys. Rev. Lett. **62**, 819 (1989).
- [102] Soshin Chikazumi, *Physics of Ferromagnetism* second edition, P361, Clarendon Press, Oxford, 1997.
- [103] R. M. Bozorth and J. G. Walker, Phys. Rev. **89**, 624 (1951).
- [104] R. M. Bozorth, *Ferromagnetism* (Van Nostrand, 1951), chap. 13, p.664.
- [105] Y. K. Kim and T. J. Sila, Appl. Phys. Lett. **68(20)**, 2885 (1996).
- [106] O. Song, C. A. Ballentine and R. C. O'Handley, Appl. Phys. Lett. **64(19)**, 2593 (1994).
- [107] G. Blatter, M. V. Feigelman, V. B. Geshkenbein, A. I. Larkin, and V. M. Vinokur, Rev. Mod. Phys. **66**, 1125 (1994).
- [108] S. Lemerle, J. Ferré, C. Chappert, V. Mathet, T. Giamarchi, and P. Le Poussal, Phys. Rev. Lett. **80**, 849 (1998).
- [109] J. Ferré, J. P. Jamet, and P. Meyer, Phys. Stat. Sol.(a) **175**, 213 (1999).
- [110] H. Matsuyama, C. Haginoya, K. Koike, Phys. Rev. Lett. **85**, 646(2000).
- [111] S. H. A. Padmore, R. M. Duarte, T. Renner, T. Stammler, A. Scholl, M. R. Scheinfein, J. Stöhr, L. Séve, and B. Sinkovic, Rev. Sci. Instrum. **70**, 3973(1999).
- [112] M. T. Hutchings, Phys. Rev. B **6**, 3447 (1972).
- [113] K. Kurosawa, M. Miura, S. Saito, J. Phys. C **13**, 1521 (1980).
- [114] H. Zijlstra, IEEE Tans. Magn., **Mag.15**, 1246(1979).

- [115] H. Gengnagel and U. Hoffmann, *Phys. Stat. Sol.*, **29**, 91 (1968).
- [116] M. D. Stiles, R. D. McMichael, *Phys. Rev. B* **59**, 3722 (1999).
- [117] R. Skomski, J. P. Liu and D. j. Sellmyer, *Phys. Rev. B* **60**, 7359(1999).
- [118] Z. Li and S. Zhang, *Phys. Rev. B* **61**, R14897(2000).
- [119] D. V. Dimitrov, S. Zhang, J. Q. Xiao, G. C. Hadjipanayis, and C. Prados, *Phys. Rev. B* **58**, 12090(1998).
- [120] T. C. Schulthess, and W. H. Butler, *Phys. Rev. Lett.* **81**, 4516(1998).
- [121] T. C. Schulthess, and W. H. Butler, *J. Appl. Phys.* **85**, 5510(1999).
- [122] H. D. Chopra, D. X. Yang, P. J. Chen, H. J. Brown, L. J. Swartzendruber, and W. F. Egelhoff. Jr. *Phys. Rev. B* **61**, 15312(2000).
- [123] J. Ding and J. G. Zhu, *J. Appl. Phys.***79**, 5892(1996).
- [124] Z. Qian, M. T. Kief, P. K. George, J. M. Sivertsen and J. H. Judy, *J. Appl. Phys.* **85**, 5525(1999).
- [125] V. I. Nikitenko, V. S. Gornakov, L. M. Dedukh, Yu. P. Kabanov, A. F. Khapikov, A. J. Shapiro, R. D. Shull, A. Chaiken and R. P. Michel, *J. Appl. Phys.* **83**, 6828(1998).
- [126] V. S. Gornakov, V. I. Nikitenko, L. H. Bennett, H. J. Brown, M. J. Donahue, W. F. Egelhoff, R. D. McMichael, and A. J. Shapiro, *J. Appl. Phys.* **81**, 5215(1997).
- [127] U. Hartmann, and H. H. Mende, *J. Phys. D***18**, 2285(1985).
- [128] Y. Iwasaki, M. Takiguchi, and K. Bessho, *J. Appl. Phys.* **81**, 5021(1997).
- [129] V. I. Nikitenko, V. S. Gornakov, L. M. Dedukh, Yu. P. Kabanov, A. F. Khapitov, A. J. Shapiro, R. D. Shull, A. Chaiken, and R. P. Michel. *Phys. Rev. B* **57**, R8111(1998).
- [130] A. Khapikov, *Phys. Rev. Lett.* **80**, 2209 (1998).
- [131] T. J. Moran, J. M. Gallego, and Ivan K. Schuller, *J. Appl. Phys.* **78**, 1887(1995).
- [132] C. Leighton, J. Nogués, B. J. Jönsson-Åkerman, and Ivan K. Schuller, *Phys. Rev. Lett.***84**, 3466(2000).

Summary

When a ferromagnetic (FM) material contacts with an antiferromagnetic (AFM) material, its magnetic properties can be modified and some new phenomena could appear. Among them, the exchange anisotropy is of great interest due to its strong application in magnetic reading heads and magnetic sensors. Typically, the exchange anisotropy shows up as a shifted hysteresis in the magnetic field axis and large coercivity enhancement compared with a single ferromagnetic material. The exchange anisotropy has been extensively studied and many models have been proposed to understand its intrinsic physics. The effect, however, is not completely understood, partially due to the complexity of the spin and crystal structures. And most of characterizations were done with the macroscopic measurement, i.e., the hysteresis. Only until very recently, imaging techniques are implanted to reveal the microscopic features.

In this thesis, we present the study of the exchange interaction among a single crystalline system utilizing the combination of both macroscopic (MOKE) and microscopic (SEMPA) methods. In this system, ultrathin Fe films are epitaxially grown on NiO(001) single crystals. The NiO(001) single crystal has well known spin structure which simplifies the matter of interest. With the epitaxy of the Fe film and the high quality of the NiO(001) single crystal, the interface conditions can be well controlled. Further, the advance of the in-field SEMPA allows us to field by field compare the microscopic images with the macroscopic features characterized by the MOKE measurement. The experimental results and the model proposed to explain our findings are summarized as the following:

1) When a Fe film is epitaxially deposited on a single crystal substrate, its magnetic domain orientation should follow its easy axis assuming the surface anisotropy contribution is negligible. The magnetic domains of Fe film deposited on NiO(001), however, are different with the Fe film deposited on usual single crystal substrate. In this system, two types of domain walls were found on Fe film, shown in Fig. 1 or Fig. 2. Straight 90° type domain walls of Fe film locate at the same position with the T-walls of the NiO along $[100]$ (or $[010]$) direction of the NiO(001) while at the position of the T-walls along $[110]$ (or $[1-10]$), no domain wall is found. Within a single T-domain of the NiO, the Fe film domains are separated with 180° walls, which reveal strong uniaxial anisotropy. These findings suggest a strong correlation between the Fe film and the NiO(001) substrate.

2) To study this correlation in detail, we compare the magnetic images obtained on two types of NiO(001) surfaces. For the films grown on type I NiO(001) single crystal, the spin

orientation of the Fe films are aligned solely along $[110]$ (or $[1-10]$) direction (see Fig.1). Interestingly, for the films grown on type II NiO(001) surface, the spins of the Fe films inclined $6^\circ \pm 12^\circ$ from $[-110]$ direction or $11^\circ \pm 12^\circ$ from $[110]$ direction (see Fig.2). This kind of magnetic domain pattern of Fe films can be stabilized up to 30ML. Apart from a small motion of a fraction of T-walls, the Fe domains remain almost unchanged with increasing the thickness of Fe film.

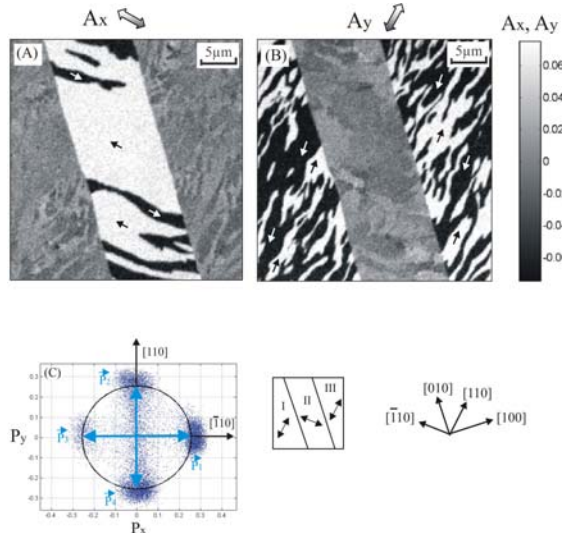


Fig. 1. A typical SEMPA measurement of 10ML Fe grown on type I NiO(001). (A) and (B) Fe domains in the asymmetry components of A_x and A_y . (C) spin histogram. The spins of Fe film on region II are oriented along $[-110]$ direction, on regions I and III along $[110]$ direction. See text for explanation.

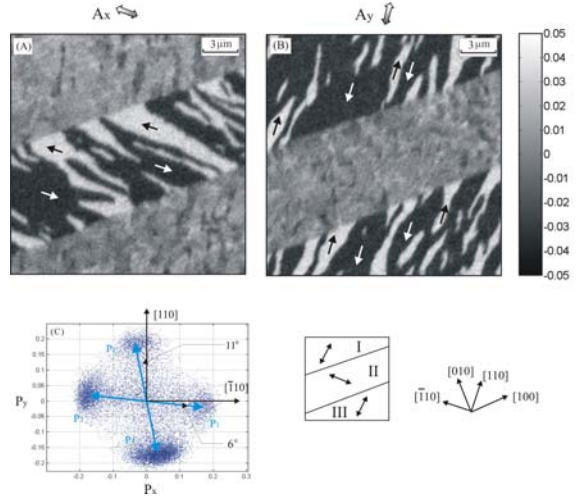


Fig. 2. A typical SEMPA measurement of 14ML Fe grown on type II NiO(001). (A) and (B) Fe domains in the asymmetry components of A_x and A_y . (C) spin histogram. The spins of Fe film on region II are inclined $6^\circ \pm 12^\circ$ from $[-110]$ direction, on regions I and III are inclined $11^\circ \pm 12^\circ$ from $[110]$ direction. See text for explanation.

3) As the structure distortion of the NiO at (001) plane is in the order of 10^{-3} which is 2 orders of magnitude of higher than the magnetostriction coefficient of bulk Fe (10^{-5}), we speculate the uniaxial anisotropy may come from two origins. It may come from either the exchange interaction between the spins of Fe film and the antiferromagnetic NiO or the magnetoelastic anisotropy induced by the structure distortion of the NiO. To further determine the origin of the effect, we repeat the same measurement, but with a material with vanishing magnetostriction, i.e., Permalloy ($\text{Fe}_{20}\text{Ni}_{80}$). Similar results are obtained on both Fe and Permalloy films grown on the same Ni(001) crystal. This suggests that the magnetoelastic anisotropy effect is not the dominant mechanism for the uniaxial anisotropy. Further, the structural distortion of the NiO is symmetric along crystal diagonal $[110]$ (or $[1-10]$) direction. The inclined angle of Fe film on type II NiO(001), however, shows that the Fe spins have no diagonal symmetry, which indicates that structural effect is not the major origin of the uniaxial anisotropy.

4) To explain our experimental observations, a phenomenological model is proposed. In the model, we assume that the T-domains (ferromagnetic planes) of the NiO(001) at the interface are the same as that in bulk crystal, but the individual AFM spins at the interface are energy favorably to rotate within its FM planes due to the relatively weak in-plane anisotropy K_2 of NiO. The inclined angle of Fe spins and the rotation of AFM spins at interface depend on the strength of exchange interaction. To describe the exchange coupling strength, a parameter λ (proportional to the exchange stiffness at interface) is introduced. When $\lambda \gg 1$, the strong exchange coupling forces the AFM spins to rotate at interface and collinear couple to Fe spins. The Fe spins and AFM spins are parallel and along $[110]$ (or $[1-10]$) direction at the interface, which explains the exchange interaction of Fe film grown on type I NiO(001) single crystal. When $\lambda \ll 1$, the Fe spins and AFM spins are independently along their own easy axes due to the negligible exchange interaction. In between, both of the spins of Fe film and AFM can rotate from their easy direction to minimize the total energy. For Fe film it performs an inclined angle from $[110]$ (or $[1-10]$) direction, where the magnitude of inclined angle indicates the strength of exchange interaction. It explains the exchange interaction of Fe (and Py) film grown on type II NiO(001) single crystal.

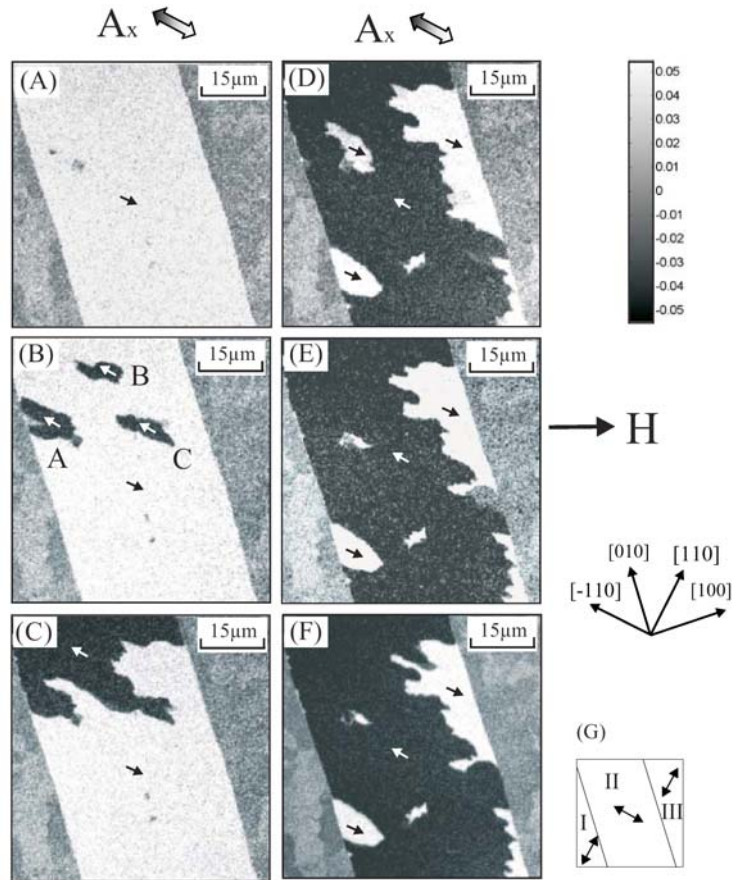


Fig. 3 Magnetic domain wall creeping of 20ML Fe film grown on NiO(001). The applied magnetic field $H = -23.2\text{mT}$. (A) shows the Fe domains image at beginning. (B) after one hour; (C) 2 minutes more; (D), (E) and (F) are sequences of Fe domains in 2 hours. (G) a sketch for T-walls and easy axes of Fe film. See text for explanation.

5) To understand the magnetization switching process of the epitaxial Fe film on NiO(001), both the macroscopic study and microscopic analysis are carried out. The macroscopic measurement by MOKE shows that the Fe film has a uniaxial symmetry instead of a four-fold symmetry expected from the structure. The hysteresis loop is symmetric in the field axis and has an enhanced coercivity. The missing of the exchange bias may be due to that the film was not treated with a field cooling procedure. The induced uniaxial anisotropy and the enhanced coercivity indicate that the exchange interaction existing between the Fe film and the underlying NiO. For the same film, in-field SEMPA shows that the magnetization reversal of the Fe film proceeds with domain nucleation and wall motion. The reversed domains are found to nucleate at the crystal defects or T-walls. The reversed domains expand by the thermally assisted wall creeping which only exists in a narrow field range near the coercivity (see Fig. 3). The comparison of the measurements with both the MOKE and in-field SEMPA suggests that the coercivity enhancement in Fe/NiO case comes from the generation of a twist wall at interface of the antiferromagnetic NiO.

Finally, it is worth to mention the aspects of the experimental setups. With the Fe/NiO(001) experiments, we demonstrate that the in-field SEMPA is a powerful technique to study the magnetic switching process from the microscopic point of view. In combination with the macroscopic method like MOKE, it can give us more complete picture of the magnetization reversal.

Zusammenfassung

Wird ein ferromagnetisches Material in direkten Kontakt mit einem Antiferromagneten gebracht, können neue ferromagnetischen Eigenschaften und auch neue Phänomene entstehen. Unter diesen, ist das Auftreten der Austauschisotropie besonders interessant, da dieser Effekt auch für verschiedene Anwendungen genutzt werden kann, wie zum Beispiel magnetische Leseköpfe und Sensoren. Typischerweise führt die Austauschisotropie zu einer Verschiebung der Hystereseschleife entlang der Feldachse und zu einer deutlichen Vergrößerung der Koerzitivfeldstärke im Vergleich zum isolierten ferromagnetischen Material. Die Austauschisotropie wurde bereits eingehend untersucht und viele Modelle wurden vorgeschlagen um deren intrinsische Physik zu verstehen. Trotzdem blieb das Verständnis nur unvollständig, zum Teil aufgrund der Komplexität der auftretenden Elektronenspin- und Kristallstrukturen. Zudem beschränkten sich die meisten Untersuchungen auf die Beobachtung von makroskopischen Größen wie zum Beispiel der Hystereseschleife. Erst seit kurzem werden verstärkt hochauflösende Abbildungsverfahren eingesetzt, um auch die mikroskopischen Eigenschaften zu erfassen.

In der vorliegenden Arbeit wird die Austauschwechselwirkung anhand eines ein kristallinen Systems untersucht, wobei eine Kombination von makroskopischen (MOKE) und mikroskopischen (SEMPA) Methoden genutzt wird. Als Materialsystem werden epitaktisch gewachsene, ultradünne Eisenfilme auf der (001) Oberfläche von Nickeloxidkristallen verwendet. Dieses Substrat wurde gewählt, da es eine wohlbekannt antiferromagnetische Spinordnung aufweist, wodurch die Fragestellung vereinfacht wird. Die Epitaxie des Eisenfilms und die hohe Qualität der Nickeloxidoberfläche ermöglichen eine genaue Kontrolle der Interfaceeigenschaften. Zudem wird es durch eine Weiterentwicklung von SEMPA (in-field SEMPA) möglich, mikroskopische Aufnahmen, die schrittweise bei bestimmten Feldstärken gemacht werden, mit den makroskopischen Eigenschaften, die durch MOKE Messungen bestimmt werden, zu vergleichen. Die experimentellen Resultate und ein Modell, das zur Erklärung der Ergebnisse vorgeschlagen wird, seien im folgenden zusammengefaßt:

- 1) Eisenfilme, die epitaktisch auf einer Einkristalloberfläche gewachsen sind, sollten bei vernachlässigbarer Oberflächenanisotropie innerhalb einer ferromagnetischen Domäne eine Magnetisierungsrichtung aufweisen, die mit einer der leichten Achsen [Richtungen] von Eisen zusammenfällt. Die magnetischen Domänen der Eisenfilme auf der (001) Oberfläche von Nickeloxid unterscheiden sich jedoch von Eisenfilmen auf gewöhnlichen einkristallinen Substraten. Bei diesem System werden zwei Arten von Domänenwänden im Eisenfilm beobachtet (Abb. 1 und 2). Gerade 90° Domänenwände werden im Eisenfilm bei der Position von antiferromagnetischen T-Domänenwänden des (001) Nickeloxidkristalls beobachtet, wenn die T-Domänenwand entlang der [100]- oder [010] Richtung orientiert ist, während bei T-Domänenwänden entlang der [110]- oder [1-10] Richtung direkt über der Wand im Eisenfilm keine ferromagnetischen Domänenwände beobachtet werden. Innerhalb einer einzelnen T-Domäne des Nickeloxidkristalls sind die Eisendomänen durch 180° Wände voneinander

getrennt, was auf eine starke uniaxiale Anisotropie schließen lässt. Diese Ergebnisse weisen auf eine eindeutige Korrelation zwischen Eisenfilm und (001) Oberfläche des Nickeloxidsubstrats hin.

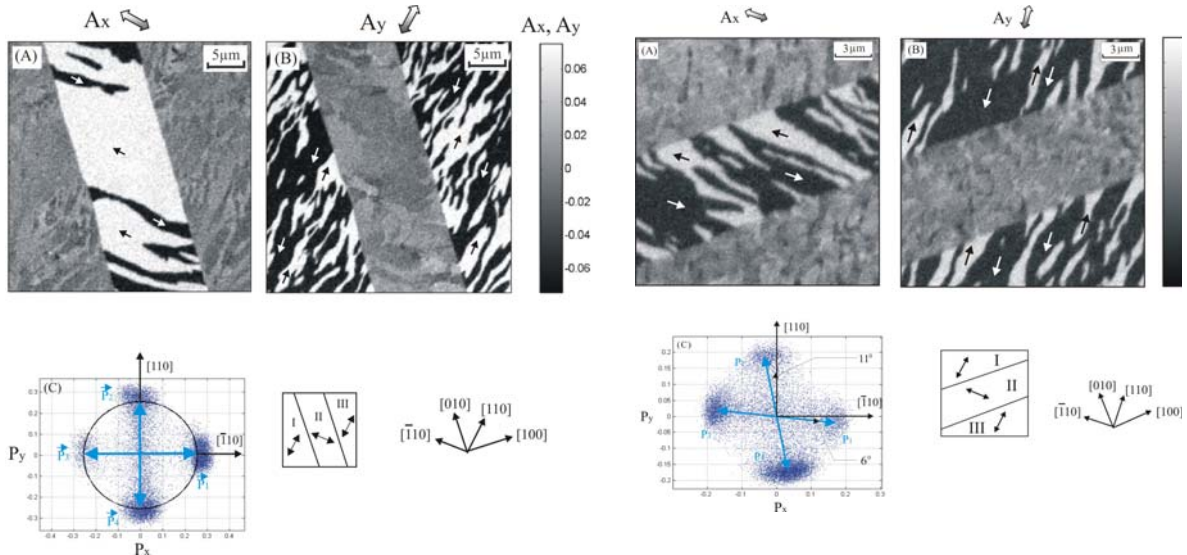


Abb. 1. Typische SEMPE Aufnahme eines 10 Monolagen dicken Eisenfilms, der auf der (001) Oberfläche von Nickeloxid gewachsen ist, das nach Verfahren I präpariert wurde. Die Asymmetriekomponenten A_x (A) und A_y (B) zeigen die Domänen im Eisenfilm. (C) Spinhistogramm. Im Bereich II ist der Spin des Eisenfilms entlang der $[-110]$ Richtung ausgerichtet und in den Bereichen I und III entlang der $[110]$ Richtung. Siehe Text zur Erklärung.

Abb. 2. Typische SEMPE Aufnahme eines 14 Monolagen dicken Eisenfilms, der auf der (001) Oberfläche von Nickeloxid gewachsen ist, das nach Verfahren II präpariert wurde. Die Asymmetriekomponenten A_x (A) und A_y (B) zeigen die Domänen im Eisenfilm. (C) Spinhistogramm. Im Bereich II weicht der Spin des Eisenfilms um $6^\circ \pm 12^\circ$ von der $[-110]$ Richtung ab, und in den Bereichen I und III um $11^\circ \pm 12^\circ$ von der $[110]$ Richtung. Siehe Text zur Erklärung.

2) Um diese Korrelation genauer zu untersuchen, wurde die Nickeloxid (001) Oberfläche auf zwei unterschiedliche Weisen präpariert (im folgenden Typ I und Typ II genannt) und die beobachteten Eisendomänenstrukturen verglichen. Die Eisenfilme, die auf der Typ I Oberfläche gewachsen sind, weisen eine Spinorientierung auf, die ausschließlich entlang der $[110]$ (oder der $[-110]$) Richtung liegt (siehe Abb.1). Interessanterweise weicht bei den Filmen, die auf der Typ II Nickeloxidoberfläche gewachsen sind, die Spinrichtung von $[110]$ bzw. der $[-110]$ Richtung ab. Die Abweichung beträgt $6^\circ \pm 12^\circ$ bei der $[-110]$ Richtung und $11^\circ \pm 12^\circ$ bei der $[110]$ Richtung (siehe Abb.2). Die Domänenstrukturen der Eisenfilme bleiben stabil bis zu einer Schichtdicke von 30 Monolagen. Abgesehen von kleinen Verschiebungen mancher T-Domänenwände bleiben die Eisendomänen bei einer Erhöhung der Eisenschichtdicke nahezu unverändert.

3) Die Gitterverzerrung von Nickeloxid an der (001) Oberfläche liegt in der Größenordnung von 10^{-3} und übersteigt damit den Magnetostruktionskoeffizienten von Eisen

(10^{-5}) um zwei Größenordnungen. Daher kommen zwei Ursachen für die uniaxiale Anisotropie in Frage. Zum einen könnte die Anisotropie durch die Austauschwechselwirkung zwischen den Spins im Eisenfilm und im antiferromagnetischen Nickeloxid entstehen, oder es könnte sich um eine magnetoelastische Anisotropie handeln, die durch die Gitterverzerrung des Nickeloxids induziert wird. Um die Ursache des Effektes genauer zu bestimmen, wurden die Messungen mit Permalloy-Filmen wiederholt, da dies ein Material ist, das eine verschwindende Magnetostriktion aufweist. Für beide, Eisen- und Permalloy-Filme, wurden sehr ähnliche Ergebnisse erzielt, wobei der gleiche Nickeloxidkristall verwendet wurde. Dies weist darauf hin, dass die magnetoelastische Anisotropie nicht die Hauptursache für die Ausbildung der uniaxialen Anisotropie ist. Zudem ist die Gitterverzerrung von Nickeloxid entlang der Kristalldiagonalen $[110]$ (oder $[1-10]$) symmetrisch. Die Spinrichtungen, die bei Eisenfilmen auf Typ II Nickeloxid (001) beobachtet werden, weisen jedoch keine diagonale Symmetrie auf. Dies läßt erkennen, dass ein struktureller Effekt nicht die Hauptursache für die uniaxiale Anisotropie ist.

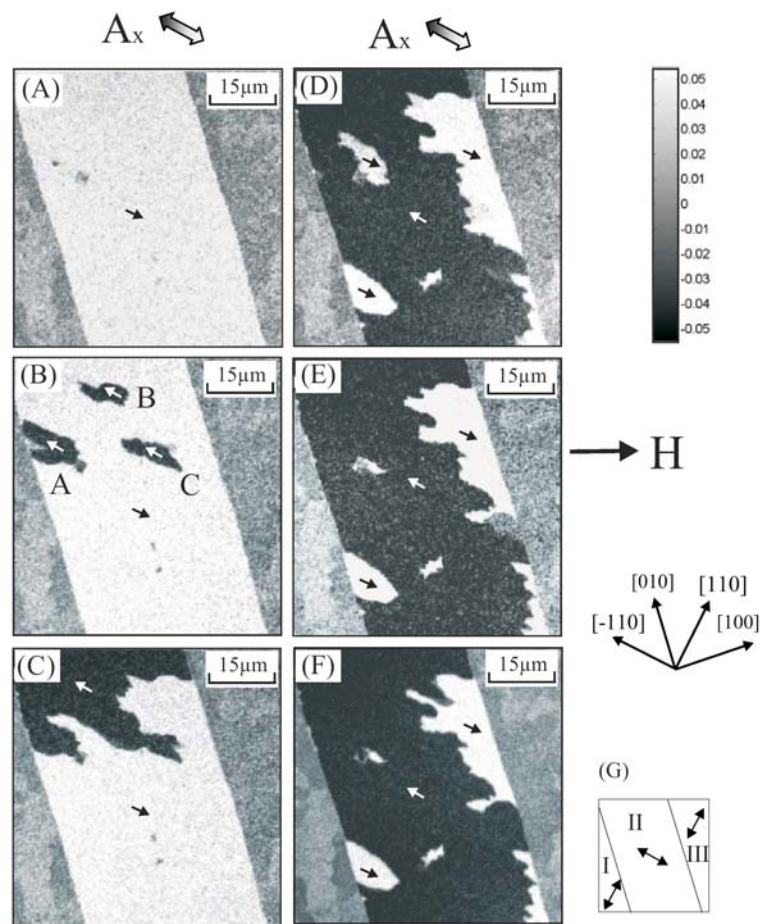


Abb. 3 Magnetisches Wandkriechen in einem 20 Monolagen dicken Eisenfilm, der auf (001) Nickeloxid gewachsen ist. Das angelegte magnetische Feld ist -23.2 mT. (A) zeigt den Anfangszustand der Domänenstruktur im Eisenfilm. (B) nach einer Stunde, (C) nach weiteren zwei Minuten; (D), (E) und (F) sind eine Folge von Aufnahmen der Eisendomänenstruktur im Abstand von 2 Stunden. In (G) sind die T-Wände und die leichten Richtungen von Eisen skizziert. Siehe Text zur Erklärung.

4) Um die experimentellen Beobachtungen zu erklären, wird ein phänomenologisches Modell vorgeschlagen. In diesem Modell wird angenommen, dass die T-Domänen (ferromagnetische Ebenen) des (001) Nickeloxidkristalls am Interface eine Abweichung von der Volumenstruktur darstellen, die dadurch entsteht, dass sich die individuellen antiferromagnetischen Spins innerhalb ihrer ferromagnetischen Ebenen aufgrund der niedrigen in-plane Anisotropie K_2 von Nickeloxid drehen können, um die Energie zu minimieren. Diese Drehung und die Abweichung der Fe Spins von den leichten Achsen hängen von der Stärke der Austauschwechselwirkung ab. Um diese zu beschreiben, wird der Parameter λ eingeführt, der proportional zur Austauschsteifigkeit ist. Für $\lambda \gg 1$ führt die starke Austauschkopplung dazu, dass die antiferromagnetischen Spins am Interface rotieren und kollinear zum Eisenspin werden. Die Spinrichtungen im Eisen und im Antiferromagneten sind am Interface parallel entlang der [110] (oder [1-10]) Richtung, wodurch die Austauschwechselwirkung der Eisenfilme auf Typ I (001) Nickeloxid erklärt wird. Für $\lambda \ll 1$ ist die Austauschwechselwirkung vernachlässigbar, und die Spinmomente des Eisenfilms und des Antiferromagneten orientieren sich unabhängig voneinander entlang ihrer jeweiligen leichten Achsen. Im Übergangsbereich können beide Spinrichtungen, die des Eisenfilms und des Antiferromagneten, von ihren leichten Richtungen abweichen um die Gesamtenergie zu minimieren. Beim Eisenfilm führt dies zu einer Abweichung von der [110] (oder [1-10]) Richtung, wobei die Größe der Abweichung ein Maß für die Stärke der Austauschwechselwirkung darstellt. Dies erklärt die Austauschwechselwirkung der Eisen- und Permalloy-Filme, die auf der Typ II (100) Nickeloxidoberfläche gewachsen wurden.

5) Um den magnetischen Schaltprozeß von epitaktischen Eisenfilmen auf der (001) Oberfläche von Nickeloxid zu verstehen, wurde dieser makroskopisch und mikroskopisch untersucht. Die makroskopischen MOKE-Messungen zeigen, dass der Eisenfilm eine uniaxiale Symmetrie aufweist, anstatt einer vierzähligen Symmetrie, wie man es aufgrund der Kristallstruktur erwarten würde. Die Hystereseschleife ist bezüglich der Magnetfeldrichtung symmetrisch und zeigt eine erhöhte Koerzitivfeldstärke. Die Abwesenheit einer Verschiebung der Hystereseschleife entlang der Feldachse kann dadurch verursacht sein, dass die Filme keine Abkühlungsprozedur im Magnetfeld durchlaufen haben. Die induzierte uniaxiale Anisotropie und die vergrößerte Koerzitivität weisen die Existenz der Austauschkopplung zwischen Eisenfilm und dem darunterliegenden Nickeloxidsubstrat nach. Für den gleichen Film zeigen die in-field SEMPA Messungen dass der magnetische Schaltprozeß des Eisenfilms durch Domänennukleation und Wandverschiebung abläuft. Die Nukleation von entgegengesetzten Domänen wird bei Kristalldefekten oder T-Domänenwänden beobachtet. Die entgegengesetzten Domänen expandieren durch thermisch unterstütztes Wandkriechen, das nur in einem schmalen Feldbereich um die Koerzitivfeldstärke existiert. Der Vergleich der MOKE und in-field SEMPA Messungen läßt es naheliegend erscheinen, dass die Vergrößerung der Koerzitivität des Eisenfilms durch die Ausbildung einer Wandstruktur bedingt ist, die zu einer Verdrehung der antiferromagnetischen Spinmomente des Nickeloxids am Interface führt.

Zum Abschluß sind einige Aspekte zum experimentellen Aufbau erwähnenswert. Durch die Experimente an Eisenfilmen auf Nickeloxid wurde gezeigt, dass in-field SEMPA eine leistungsfähige Methode ist, um magnetische Schaltprozesse mikroskopisch zu untersuchen. In Kombination mit einer makroskopischen Methode wie MOKE kann es uns ein vollständigeres Bild des magnetischen Schaltprozesses geben.

Appendix A

Curriculum Vitae

Personal data:

Name: Guolei Liu
Date of birth: August 01, 1972
Place of birth: Ningbo, Zhejiang province, China
Marital status: Single

Educations:

July. 1999 – Jun. 2002 Ph.D candidate at Max-Planck-Institute für Mikrostrukturphysik, Halle, Germany.
Supervisor: Prof. Dr. Jürgen Kirschner
Thesis: Exchange interaction of Fe films on NiO(001) single crystals

Sep. 1996 – June. 1999 M. Sc at Fudan University, Shanghai, China
Supervisor: Prof. Dr. Xiaofeng Jin
Major: Heterostructure of Ferromagnetic-semiconductor and devices

Sep. 1992 – July. 1996 B. Sc at Nankai University, Tianjin, China

Sep. 1989 – July. 1992 High school of Ninghai, Ningbo, Zhejiang province, China

Sep. 1986 – July. 1989 Secondary school of Xidian, Ningbo, Zhejiang province, China

Sep. 1981 – July. 1986 The Xiangshan primary school at Ningbo, Zhejiang province, China

Shanghai, China, 25 March, 2003-4-6

Guolei Liu

Appendix B

Erklärung

Ich versichere hiermit, die vorliegende Dissertation

Exchange interaction of Fe films grown on NiO(001) single crystals

selbständig verfasst und keine anderen als die von mir angegebenen Quellen und Hilfsmittel verwendet zu haben. Die in den benutzten Werken wörtlich oder inhaltlich entnommenen Stellen sind als solche kenntlich gemacht.

Shanghai, China, 25 March, 2003

Guolei Liu

Appendix C

Acknowledgment

First of all I would greatly thanks Prof. Jürgen Kirschner, my supervisor, for offering me a chance to work at Max-Planck-Institut für Mikrostrukturphysik at Halle (Saale), and for his many suggestions and constant supports during the research.

I am very grateful to Dr. Gerold Steierl for teaching me the technique of SEMPA. I thanks him for spending lots of time in explaining me all the experimental details, tricks and data analysis. I really appreciate many long time discussions. His patience and encouragement are very important for me.

I should mention the helps and encouragement from Prof. Hans Peter Oepen at MPI at first year. I thank very much to Prof. Xiaofeng Jin, my master degree supervisor, for his recommendation and long time encouragement.

I would be thankful to Dr. Dimitre Iorgov. I learned a lot from his experiences on Scanning Electron Microscopy and frequently discussions on technical details. I thanks very much to Dr. Miroslav Nyvlt and Dr. Francesco Bisio for their supports on optical measurements. I thanks Dr. Francesco Offi for long time discussions on the subject of exchange interaction. I am pleasure to meet Dr. Fabrizio Porrati, Dr. Jochen Barthel and Dr. Haifeng Ding and Dr. Yizheng Wu. They are wonderful friends and I appreciate their kindness and friendship.

I would like to thanks my colleagues and coworkers: Dr. Dimitre Iorgov, Dr. Fabrizio Porrati, Dr. Jochen Barthel, Dr. Miroslav Nyvlt, Dr. Francesco Offi, Dr. Francesco Bisio, Dr. Manfred Klaua, Dr. Ricarrdo Hertel, Dr. Kin Ha, Dr. Florin Zavaliche, Dr. Xianghong Qian, Dr. Dirk Ullman for their helps and friendship.

Of course I wish to thanks the following for their technical supports: Miss. Heike Menge, Mr. Herbert Engelhard, Dr. Jochen Barthel, Mr. Annelies Kroder, Mr. Perlich Peter, Dr. Hellmut Höche, Dr. Hartmut Schwabe, Mr. Eberhard Hunold, Mr. Hetlef Hartung and all the people at electric and mechanical workshops in MPI.

I am also thanks all the friends who I met in Halle for their kindly helps in my life: Dr. Yixing Zhang, Mrs. Yun Luo, Dr. Xiaohong Chen, Dr. Dong Shen, Dr. Lixing Yi, Dr. Xucun Ma, Mr. Keike Fukumoto, Dr. Chao Jin, Dr. Duochun Sun, Dr. Dong Qian, Dr. Wenhong Wang.

Finally, I am grateful to my parents for their patience and love. Without them this work would never have come into existence (literally).

Shanghai, 25 March, 2003

Guolei Liu